universität wien

DISSERTATION | DOCTORAL THESIS

Titel | Title

Towards High-Accuracy Auxiliary-Field Quantum Monte Carlo: Methodological Advancements and Applications

verfasst von | submitted by

Zoran Sukurma BSc MSc

angestrebter akademischer Grad | in partial fulfilment of the requirements for the degree of

Doktor der Naturwissenschaften (Dr.rer.nat.)

Wien | Vienna, 2025

Studienkennzahl lt. Studienblatt | Degree programme code as it appears on the student record sheet:	UA 796 605 411
Dissertationsgebiet lt. Studienblatt | Field of study as it appears on the student record sheet:	Physik
Betreut von | Supervisor:	Univ.-Prof. Dipl.-Ing. Dr. Georg Kresse


universität
wien

Abstract

Auxiliary-field quantum Monte Carlo (AFQMC) is emerging as a powerful method for computing electronic ground-state properties in molecules, solids, and lattice models. AFQMC employs imaginary-time propagation to extract the many-body ground state from a trial state. In its simplest formulation, using a Hartree-Fock trial wave function, AFQMC scales quartically with system size and achieves accuracy between the well-established coupled cluster singles and doubles (CCSD) method and the "gold standard" CCSD(T) method, which additionally includes perturbative triples.

In this work, we first present a scalable Fortran implementation of the AFQMC method and demonstrate its excellent performance on CPUs. We apply AFQMC to 26 molecules from the HEAT dataset, achieving near chemical accuracy with a mean absolute deviation of 1.15 kcal/mol. Additionally, we explore modifications to the phaseless approximation to address overcorrelation issues common to AFQMC. However, it remains unclear whether these modifications generally improve the method's accuracy.

Next, we examine the AFQMC propagation and analyze the associated time-step errors. We demonstrate that the second-order split technique and the Krylov method for approximating matrix exponentials minimize time-step errors. Furthermore, by modifying the reweighting procedure and rare event control, we eliminate size-consistency errors in large time-step AFQMC calculations. This enables robust time-step extrapolation using a second-order polynomial fit. With this protocol, we obtain accurate complete basis set binding energies for small water clusters, achieving a mean absolute error of 0.07 kcal/mol relative to CCSD(T).

Finally, we couple the AFQMC random walk with non-orthogonal configuration interaction (NOCI) to sample more accurate trial wave functions. We develop an efficient selection algorithm that identifies those random walkers most effective in lowering the NOCI energy. The resulting multideterminantal trial wave functions with typically 100 to 200 Slater determinants substantially reduce systematic and stochastic AFQMC errors, outperforming CCSD(T) for weakly correlated systems.

Zusammenfassung

Auxiliary-Field Quantum Monte Carlo (AFQMC) gewinnt zunehmend an Bedeutung als effiziente Methode zur Berechnung elektronischer Grundzustandseigenschaften in Molekülen, Festkörpern und Gittermodellen. AFQMC verwendet die Propagation in imaginärer Zeit, um den Grundzustand aus einem Trialzustand zu extrahieren. In seiner einfachsten Form—unter Verwendung einer Hartree-Fock-Trialwellenfunktion—skaliert AFQMC quartisch mit der Systemgröße und erreicht eine Genauigkeit, die zwischen der etablierten Coupled-Cluster-Methode mit singles und doubles (CCSD) und der "Goldstandard"-Methode CCSD(T) liegt, die zusätzlich perturbative triples berücksichtigt.

In dieser Arbeit präsentieren wir zunächst eine skalierbare Fortran-Implementierung der AFQMC-Methode und demonstrieren deren exzellente Leistung auf CPUs. Wir wenden AFQMC auf 26 Moleküle des HEAT-Datensatzes an und erzielen eine mittlere absolute Abweichung von 1.15 kcal/mol, die nahe an der chemischen Genauigkeit liegt. Darüber hinaus untersuchen wir Modifikationen der phaseless Approximation, um Überkorrelationsprobleme, die in AFQMC häufig auftreten, zu beheben. Allerdings bleibt unklar, ob diese Modifikationen die Genauigkeit der Methode generell verbessern.

Anschließend analysieren wir die AFQMC-Propagation und die damit verbundenen Zeitschrittfehler. Wir zeigen, dass die Split-Operator-Technik zweiter Ordnung sowie die Krylov-Methode zur Approximation von Matrixexponentialen die Zeitschrittfehler minimieren. Zudem beseitigen wir durch Modifikationen der Regewichtungsprozedur und der Kontrolle seltener Ereignisse Größeninkonsistenzen in AFQMC-Berechnungen mit großen Zeitschritten. Dies ermöglicht eine robuste Zeitschrittextrapolation mittels einer Polynomfit-Anpassung zweiter Ordnung. Mit dieser Methode erhalten wir genaue Bindungsenergien im vollständigen Basissatz und erreichen eine mittlere absolute Abweichung von nur 0.07 kcal/mol im Vergleich zu CCSD(T).

Abschließend kombinieren wir den AFQMC-Random-Walk mit nicht-orthogonaler Konfigurationsinteraktion (NOCI), um genauere Trialwellenfunktionen zu generieren. Wir entwickeln einen effizienten Auswahlalgorithmus, der die Random-Walker identifiziert, die am effektivsten zur Senkung der NOCI-Energie beitragen. Die auf diese Weise gesampelten multideterminantalen Trialwellenfunktionen, bestehend aus typischerweise 100 bis 200 Slater-Determinanten, reduzieren sowohl systematische als auch stochastische AFQMC-Fehler erheblich und übertreffen CCSD(T) für schwach korrelierte Systeme.

Acknowledgments

First and foremost, I would like to express my deepest gratitude to my supervisor, Prof. Georg Kresse, who guided me since my bachelor studies. From the very first lecture on Scientific Fortran that I attended, Georg has been a constant source of inspiration. His persistent commitment to staying at the forefront of scientific advancements continues to inspire me to this day. I am deeply grateful for his guidance, support, and countless discussions on electronic structure methods, all of which have played a crucial role in shaping both this work and my scientific career. Finally, I sincerely thank him for believing in me and for granting me the flexibility to pursue this research, even as it diverged from his central field of interest.

I extend my sincere appreciation to my colleagues Moritz Humer, Sajad Bazrafshan, Amir Taheridehkordi, and others for the stimulating discussions and the time we shared. The many hours spent during our Wednesday meetings, exchanging ideas and troubleshooting challenges, have been an integral part of this research. My deepest gratitude goes to Martin Schlipf for his unwavering support, for being the best first reviewer I could have wished for, and for providing invaluable advice on software design, which proved instrumental in achieving my research goals.

I would also like to thank Doris Hecht-Aichholzer and Christine Schrempf for fostering a harmonious working environment and for organizing wonderful group events. A special thanks goes to my colleague and fellow fountain pen enthusiast, Michael Pöltl, for his invaluable support in using the computer cluster. The hours we spent together in our fountain pen sessions were the most enjoyable breaks I could have imagined.

Beyond the academic environment, I am deeply grateful to my parents, without whose support, none of this would be possible. I extend my gratitude to my brother, my family and my friends for their support, patience, and encouragement throughout this journey. Their belief in me has been a source of strength during the most challenging moments of my educational journey. Special thanks to my cousin, Dragana, for her invaluable help in editing German texts during the early stages of my education, long before ChatGPT was available. No ChatGPT could ever replace you.

Last but not least, my heartfelt gratitude goes to my beloved wife, Jasmina **Sukurma**. No words can truly express my appreciation. Your love, patience, and support have been my greatest source of motivation throughout this journey. Thank you for every minute you spent listening to me share my Quantum Monte Carlo research ideas, and for every late night and weekend that work took away from our time together. Not to forget your creativity and invaluable help in designing graphics for the research—your contribution has left a unique mark.

Finally, I must also mention our dog, Chandler, for being an exceptional life coach, constantly reminding me of the importance of taking breaks, relaxing, and enjoying life together.

Contents

Chapter 1

Introduction

Auxiliary-field quantum Monte Carlo (AFQMC) was first invented in the 1980s as a path-integral Monte Carlo technique for obtaining the ground state of the coupled boson-fermion systems.[1–3] The path-integral formulation demonstrated excellent performance for lattice models, such as the Hubbard model.[4,5] However, its applicability to real materials was severely limited by the fermionic sign problem, which led to exponential scaling.

A major breakthrough came with the reformulation of AFQMC as an open-ended random walk. This significantly alleviated the sign problem, leading to constrained path (cp-)AFQMC[6,7] for lattice models and phaseless (ph-)AFQMC[8] for real materials. These advances extended the reach of AFQMC beyond model Hamiltonians, making it a powerful tool for electronic structure calculations.

To illustrate the broad applicability of the AFQMC method, we summarize its various applications across different materials. AFQMC can be directly applied in an atomic-like basis for isolated systems[9] and in a plane-wave basis for extended systems.[10] The generalized spin model enables the inclusion of the spin-orbit coupling[11,12], while the generalization to the BCS states allows AFQMC simulations of the superconducting phase.[13,14] Similarly, Lee *et al.*[15] introduced a generalization to correlated electrons coupled to phonons, while recent work has adapted AFQMC for cavity quantum-electrodynamical (QED) matter systems.[16]

Beyond ground-state calculations at zero temperature, AFQMC has also been successfully applied to excited-state calculations.[17,18] Given its original path-integral formulation, its extension to finite-temperature calculations is conceptually straightforward.[19,20] In addition, the computation of interatomic forces using AFQMC has been reported in the literature, further expanding its versatility.[21,22]

In this work, we focus on the phaseless auxiliary-field quantum Monte Carlo (ph-AFQMC) for calculating the ground state of isolated systems in an atomic-like basis. With the simplest trial wave function—single Slater determinant—the evaluation of a single AFQMC walker exhibits $\mathcal{O}(N^3) - \mathcal{O}(N^4)$ scaling with respect to the system size. The quartic scaling arises from the exchange energy evaluation, which becomes a computational bottleneck for large systems. This scaling can be further reduced using techniques, such as tensor hypercontractions,[23] density-fitting,[24,25] or stochastic resolution of identity.[26] These advances have enabled the wide applicability of AFQMC in recent years.[27–44]

In Chapter 4, we first demonstrate the excellent performance of our AFQMC code and its favorable scaling with system size. We then apply AFQMC to 26 molecules

from the HEAT dataset[45] to benchmark its accuracy against CCSD(T) and the more expensive CCSDTQP method, which provides reference values. Our results show that AFQMC with a Hartree-Fock trial wave function achieves accuracy comparable to CCSD(T), with a few outliers slightly increasing the mean absolute deviation. In addition, we explore modifications of the phaseless approximation[8] to prevent large overcorrelation errors typically observed in AFQMC.

In Chapter 5, we study AFQMC propagation in detail. We perform a detailed analysis of various propagators in AFQMC, identifying the second-order split technique (S2) as the optimal choice. We then investigate different methods for applying matrix exponentials to the walker determinant. Our results demonstrate that iterative Krylov methods outperform the Taylor expansion typically employed in AFQMC calculations. With these improvements, along with enhanced rare event control, we show that AFQMC errors exhibit dominant quadratic scaling with respect to the time step. This allows for the use of large time steps and a robust time-step extrapolation using a second-order polynomial fit. We test our large time-step AFQMC protocol on various systems and show that it yields accurate results even with significantly larger time steps, resulting in an order of magnitude speedup compared to traditional small time-step AFQMC calculations.

For improved accuracy, AFQMC requires more accurate trial wave functions. A natural extension involves using particle-hole multi-Slater determinants. Early implementations suffered from unsatisfactory linear scaling with respect to the number of determinants in the trial state. A lot of effort has been dedicated to developing algorithms with sublinear scaling, significantly improving the AFQMC efficiency.[46–52] On the other hand, non-orthogonal Slater determinants require fewer determinants to achieve the same accuracy, but their local energy evaluation inherently scales linearly with the number of determinants.[34,35] Another key issue is the generation of such trial wave functions using methods like resonating Hartree-Fock,[53] which remain largely underexplored.

We investigate this topic in more detail in Chapter 6. Specifically, we introduce a selection algorithm that generates non-orthogonal multi-Slater determinants directly from the AFQMC random walk. We show that these trial wave functions significantly reduce both systematic and stochastic AFQMC errors. With 100-200 Slater determinants, we observe a chemical accuracy for all tested weakly correlated systems. However, for strongly correlated systems, further refinement of the algorithm is required to attain similar accuracy.

Outline

In the next chapter, we provide a brief overview of the most widely used quantum chemistry methods and position AFQMC within this framework. We dedicate Chapter 3 and Appendices B-F to a detailed introduction to AFQMC theory. Chapters 4,5, and 6 are based on References [41, 54, 55], respectively. The theoretical sections of these papers related to AFQMC theory have been removed and consolidated into Chapter 3. Additional modifications were made to ensure consistency with the notation outlined in Appendix A. Apart from these modifications, Chapters 4,5, and 6 remain identical to the corresponding papers. Finally, we conclude the work with a brief summary in Chapter 7.

Throughout this work, all equations and derivations are presented using the restricted spin model ($\psi_{i\uparrow} = \psi_{i\downarrow} \equiv \psi_i$). The generalization to the unrestricted, or generalized spin models is straightforward.

Chapter 2

Theoretical Background

2.1 Schrödinger Equation for Many-Body Hamiltonian

Solving the time-independent many-body Schrödinger equation

$$\hat{H}\,|\Phi\rangle = E_0\,|\Phi\rangle \tag{2.1}$$

has occupied physicists and chemists for nearly a century. The many-body Hamiltonian $\hat{H}$ typically refers to the electronic Hamiltonian within the Born-Oppenheimer approximation[56], which in first quantization is defined as

$$\begin{aligned}\hat{H} &= \hat{T}_e + \hat{V}_{eN} + \hat{V}_{ee} + E_N \\ &= -\frac{1}{2}\sum_i \nabla_i^2 - \sum_{iA}\frac{Z_A}{|\hat{r}_i - R_A|} + \frac{1}{2}\sum_{i\neq j}\frac{1}{|\hat{r}_i - \hat{r}_j|} + \frac{1}{2}\sum_{A\neq B}\frac{1}{|R_A - R_B|},\end{aligned} \tag{2.2}$$

where each term represents the kinetic energy of electrons, the attractive electron-ion potential, the repulsive electron-electron interaction, and the classical nuclear-nuclear energy, respectively. Here, indices i, j refer to electronic coordinates, while indices A, B correspond to ionic coordinates (see Appendix A for the notation conventions used throughout this work).

An analytic solution of the Eq. (2.1) is known only for one-electron systems. For more complex systems, the equation can only be solved using computer simulations. Traditional grid-based approaches for solving differential equations[57] are feasible only for the smallest systems. To illustrate this, consider a numerical grid with G points per dimension. A system with N_e electrons would require G^{3N_e} grid points to represent a wave function. For a relatively small system with $G = 10$ and $N_e = 10$, we would need roughly 10^{30} bytes to store the wave function, which exceeds the storage capacity of the largest modern supercomputers.

Before exploring more efficient techniques to solve Eq. (2.1), we introduce second quantization[58–61], a powerful formalism that provides an elegant framework for describing many-body systems. In second quantization, both operators and wave functions are represented by linear operators. The central objects in this formalism are creation $\hat{c}_p^\dagger$ and annihilation $\hat{c}_p$ operators, which create or destroy an electron in the one-particle state $|\varphi_p\rangle$. They obey the following anticommutation relations

$$\begin{aligned}\{\hat{c}_p^\dagger, \hat{c}_q^\dagger\} = \{\hat{c}_p, \hat{c}_q\} = 0, \\ \{\hat{c}_p^\dagger, \hat{c}_q\} = \delta_{pq},\end{aligned} \tag{2.3}$$

which automatically ensure the antisymmetry property under the exchange of two electrons.

Given an orthonormal set of one-particle basis functions $|\varphi_p\rangle$, the many-body Hamiltonian in second quantization is expressed as

$$\hat{H} = \sum_{pq} t_{pq}\, \hat{c}_p^\dagger \hat{c}_q + \frac{1}{2} \sum_{pqrs} \langle pq|rs\rangle\ \hat{c}_p^\dagger \hat{c}_q^\dagger \hat{c}_s \hat{c}_r \tag{2.4}$$

with the one-body matrix elements

$$t_{pq} = \int \mathrm{d}^3 r\ \varphi_p^*(\mathbf{r}) \left(-\frac{1}{2} \sum_i \nabla_i^2 - \sum_{iA} \frac{Z_A}{|\hat{r}_i - R_A|} \right) \varphi_q(\mathbf{r}), \tag{2.5}$$

and the two-body matrix elements

$$\langle pq|rs\rangle = [pr|qs] = \int \mathrm{d}^3 r_1 \int \mathrm{d}^3 r_2\ \frac{\varphi_p^*(\mathbf{r}_1)\varphi_q^*(\mathbf{r}_2)\varphi_r(\mathbf{r}_1)\varphi_s(\mathbf{r}_2)}{|r_1 - r_2|}, \tag{2.6}$$

known as *electron repulsion integrals* (ERIs). For a one-particle basis of size N, the memory requirements scale as $\mathcal{O}(N^2)$ to store the one-body matrix elements and $\mathcal{O}(N^4)$ to store ERIs. Consequently, storing ERIs becomes impractical for basis sets with $N \geq 1\,000$, necessitating alternative approaches to manage and reduce memory usage in large systems.

2.2 Low-Rank Decomposition of Electron Repulsion Integrals: Modified Cholesky Decomposition

The low-rank decomposition factorizes ERIs as

$$\langle pq|rs\rangle = [pr|qs] \approx \sum_g^{N_g} L_{g,pr} L_{g,qs}, \tag{2.7}$$

where N_g scales linearly with the number of basis functions N. In this way, the four-index tensor $\langle pq|rs\rangle$ with N^4 elements is replaced by the three-index tensor $L_{g,pq}$ with $N_g N^2$ elements. Various techniques, including spectral decomposition[9], density fitting[62,63], and modified Cholesky decomposition[64–66] can be used to accomplish this task. Here, we focus on the modified Cholesky decomposition.

The *modified Cholesky decomposition*[64–66] (mCD) is an iterative procedure for decomposing positive-definite matrices. For simplicity, we first express ERIs in matrix notation, using composite indices $P = (p,r)$ and $Q = (q,s)$. In this representation, the ERIs form an $N^2 \times N^2$ positive-definite matrix $V_{PQ} = \langle pq|rs\rangle$.

In the g-th iteration of the mCD procedure, the g-th Cholesky vector L_{gP} is subtracted from the residual matrix as

$$V_{PQ}^{(g)} = V_{PQ}^{(g-1)} - L_{gP} L_{gQ} = V_{PQ} - \sum_\gamma^g L_{\gamma P} L_{\gamma Q}, \tag{2.8}$$

with an initial condition $V_{PQ}^{(0)} = V_{PQ}$. The Cholesky vector L_{gP} is selected by identifying the largest diagonal element $V_{GG}^{(g-1)}$ of the residual matrix $V_{PQ}^{(g-1)}$ and setting

$$L_{gP} = \frac{V_{GP}^{(g-1)}}{\sqrt{V_{GG}^{(g-1)}}}. \tag{2.9}$$

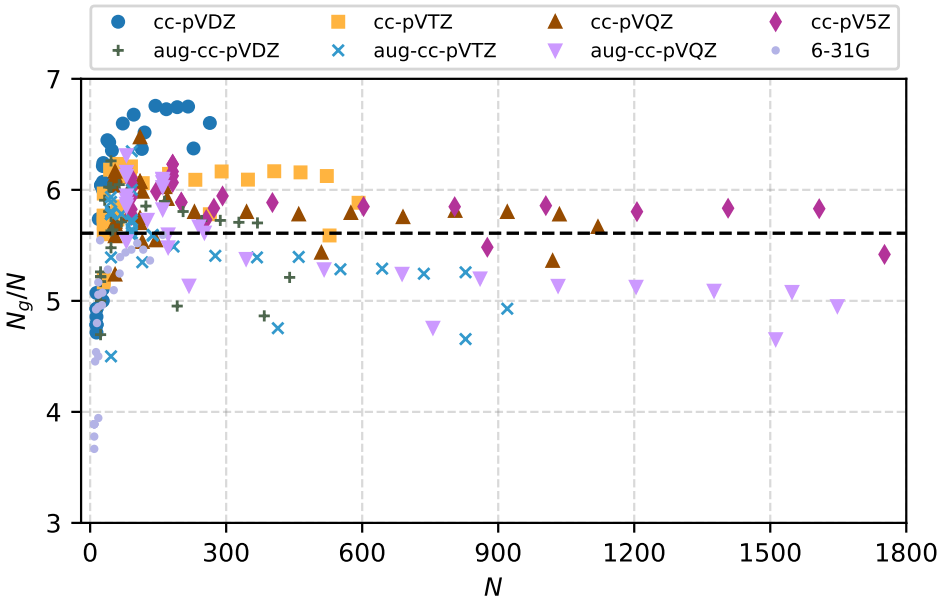

Figure 2.1: The number of Cholesky vectors N_g scales linearly with the basis set size N. We plot the N_g/N ratio as a function of N for thirty different systems, ranging from small diatomic molecules to larger organic complexes such as the benzene dimer. Each system is computed using eight different basis sets, as indicated in the legend. On average, the ratio N_g/N is approximately 6 for a typical Cholesky threshold $\delta = 10^{-5}$.

The procedure is stopped after N_g iterations when all diagonal elements of the residual matrix $V_{PP}^{(N_g)}$ drop below the specified Cholesky threshold δ.

For a typical Cholesky threshold $\delta = 10^{-5}$, the number of Cholesky vectors scales linearly with the basis set size as $N_g \approx 6N$, as illustrated in Fig. 2.1. We also show that the ratio N_g/N scales logarithmically with the threshold δ, enabling an efficient compression of the ERIs without loss of accuracy (see Fig. 2.2).

The efficient implementation of the mCD algorithm avoids storing the full residual matrix in memory, requiring only its diagonal elements. This reduces the memory requirement for storing Hamiltonian matrix elements from $\mathcal{O}(N^4)$ to $\mathcal{O}(N^3)$. Further reductions to $\mathcal{O}(N^2)$ matrix elements are possible using tensor hypercontraction techniques,[24,67] but these are not used in this work.

Using Cholesky vectors, we can rewrite Eq. (2.4) as

$$\begin{aligned}\hat{H} &= \sum_{pq}\Big(t_{pq} - \frac{1}{2}\sum_{r}\langle pr|rq\rangle\Big)\hat{c}_p^\dagger\hat{c}_q + \frac{1}{2}\sum_{g}\Big(\sum_{pq}L_{g,pq}\,\hat{c}_p^\dagger\hat{c}_q\Big)\Big(\sum_{rs}L_{g,rs}\,\hat{c}_r^\dagger\hat{c}_s\Big)\\ &= \sum_{pq}h_{pq}\,\hat{c}_p^\dagger\hat{c}_q + \frac{1}{2}\sum_{g}\hat{L}_g^2\\ &= \hat{H}_1 + \hat{H}_2\end{aligned} \tag{2.10}$$

by shifting the annihilation operator $\hat{c}_s$ two positions to the left. This form of the Hamiltonian, where the electron-electron interaction is expressed as a sum of quadratic terms, is particularly suitable for AFQMC, as we will see in the next chapter.

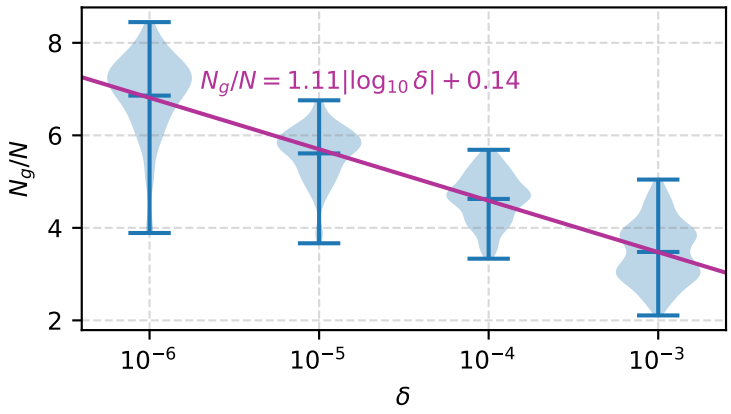

Figure 2.2: The number of Cholesky vectors N_g for a fixed basis set increases logarithmically as the Cholesky threshold δ decreases. The violin plots are depicted for several δ values. Each violin plot represents data from thirty systems and eight basis sets indicated in the legend of Fig. 2.1. The linear fit $N_g/N = 1.11|\log_{10}\delta| + 0.14$ closely matches the average N_g/N ratios illustrated in the violin plots.

2.3 Mean-Field Theory: Hartree-Fock Approximation

Hartree-Fock (HF) theory is a cornerstone of quantum chemistry and condensed matter physics. It approximates the complex electron-electron interaction with a simplified model, where each electron moves in the average field created by the other $N_e - 1$ electrons in the system. As a result, Hartree-Fock theory reduces the many-body problem to a set of one-electron equations, with each electron described by a single-particle wave function, also known as an orbital $|\psi_i\rangle$. The simplest N_e-electron wave function constructed from one-electron states that satisfies the Pauli exclusion principle is the antisymmetrized product of orbitals

$$\Psi(\mathbf{r}_1, \mathbf{r}_2, \ldots \mathbf{r}_{N_e}) = (N_e!)^{-1/2} \begin{vmatrix} \psi_1(\mathbf{r}_1) & \psi_2(\mathbf{r}_1) & \cdots & \psi_{N_e}(\mathbf{r}_1) \\ \psi_1(\mathbf{r}_2) & \psi_2(\mathbf{r}_2) & \cdots & \psi_{N_e}(\mathbf{r}_2) \\ \vdots & \vdots & \vdots & \vdots \\ \psi_1(\mathbf{r}_{N_e}) & \psi_2(\mathbf{r}_{N_e}) & \cdots & \psi_{N_e}(\mathbf{r}_{N_e}) \end{vmatrix} \tag{2.11}$$

known as a Slater determinant. From now on, we will use the shorthand notation

$$|\Psi\rangle = |\psi_1, \psi_2, \ldots \psi_{N_e}\rangle \tag{2.12}$$

to denote the Slater determinant. In a given orthonormal one-particle basis $\{|\varphi_i\rangle\}$, the Slater determinant is parametrized by the $N \times N_e$ coefficient matrix Ψ, where the i-th column represents the i-th orbital

$$|\psi_i\rangle = \sum_p \Psi_{pi} |\varphi_p\rangle \,. \tag{2.13}$$

In this basis, the Hartree-Fock energy is obtained by minimizing the determinantal energy

$$E[\Psi] = \frac{\langle\Psi|\hat{H}|\Psi\rangle}{\langle\Psi|\Psi\rangle} = 2\sum_{pq} t_{pq} D_{pq} + \sum_{pqrs} \langle pq|rs\rangle \left(2D_{pr}D_{qs} - D_{ps}D_{qr}\right) \tag{2.14}$$

with respect to the expansion coefficients Ψ

$$E_{\mathrm{HF}} = \min_{\Psi} E[\Psi]. \tag{2.15}$$

Here D is the *one-body reduced density matrix* (RDM)

$$D_{pq} = \langle \hat{c}_p^\dagger \hat{c}_q \rangle = \frac{\langle \Psi | \hat{c}_p^\dagger \hat{c}_q | \Psi \rangle}{\langle \Psi | \Psi \rangle} = (\Psi \Psi^\dagger)_{pq} = \sum_i \Psi_{pi} \Psi_{qi}. \tag{2.16}$$

In practice, the orthonormality constraint for the molecular orbital (MO) overlap matrix

$$S_{ij} = \langle \psi_i | \psi_j \rangle = (\Psi^\dagger \Psi)_{ij} = \sum_p \Psi_{ip} \Psi_{pj} = \delta_{ij}, \tag{2.17}$$

is enforced by minimizing the constrained energy functional

$$\mathcal{L}[\Psi] = E[\Psi] - \sum_{ij} \varepsilon_{ij} (S_{ij} - \delta_{ij}). \tag{2.18}$$

The stationary condition

$$\frac{\delta \mathcal{L}[\Psi]}{\delta \Psi_{pi}} = 0 \tag{2.19}$$

yields Hartree-Fock equations. A strict mathematical derivation of these equations is beyond the scope of this work; for further details, refer to standard textbooks on the subject.[58,59]

Instead, we present an illustrative derivation that emphasizes the mean-field nature of the method, as indicated by the section title. Specifically, we replace the full two-body interaction

$$\hat{H}_2 = \frac{1}{2} \sum_{pqrs} \langle pq|rs \rangle \; \hat{c}_p^\dagger \hat{c}_q^\dagger \hat{c}_s \hat{c}_r \tag{2.20}$$

with the mean-field interaction

$$\hat{H}_{\mathrm{MF}} = \frac{1}{2} \sum_{pqrs} \langle pq|rs \rangle \; \Big\{ \langle \hat{c}_q^\dagger \hat{c}_s \rangle \; \hat{c}_p^\dagger \hat{c}_r + \langle \hat{c}_p^\dagger \hat{c}_r \rangle \; \hat{c}_q^\dagger \hat{c}_s - \langle \hat{c}_p^\dagger \hat{c}_s \rangle \; \hat{c}_q^\dagger \hat{c}_r - \langle \hat{c}_q^\dagger \hat{c}_r \rangle \; \hat{c}_p^\dagger \hat{c}_s \Big\}, \tag{2.21}$$

which is further simplified by rearranging indices and using Eq. (2.16) to obtain

$$\begin{aligned} \hat{H}_{\mathrm{MF}} &= \sum_{pq} \underbrace{2 \sum_{rs} \langle pr|qs \rangle \, D_{rs}}_{J_{pq}} \; \hat{c}_p^\dagger \hat{c}_q - \sum_{pq} \underbrace{\sum_{rs} \langle pr|sq \rangle \, D_{rs}}_{K_{pq}} \; \hat{c}_p^\dagger \hat{c}_q. \\ &= 2\hat{J} - \hat{K} \end{aligned} \tag{2.22}$$

Here, $\hat{J}$ is the *Hartree potential* that corresponds to the classical electrostatic repulsion between electrons in a given one-electron basis. On the other hand, the *exchange potential* $\hat{K}$ arises directly from the antisymmetry principle and has no classical interpretation, unlike the Hartree potential.

Replacing $\hat{H}_2$ with $\hat{H}_{\mathrm{MF}}$ leads to a coupled set of one-electron Schrödinger equations, commonly known as the Roothan equations:

$$F\Psi = \Psi\varepsilon, \tag{2.23}$$

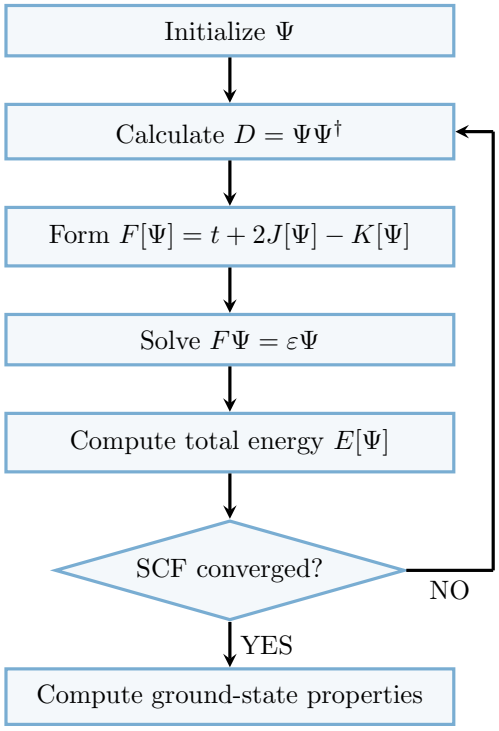

Figure 2.3: Self-consistent field (SCF) procedure for solving Hartree-Fock equations.

where F is the Fock matrix

$$F_{pq} = t_{pq} + 2J_{pq} - K_{pq}, \tag{2.24}$$

and ε is the set of eigenvalues, interpreted as orbital energies. Since F depends on Ψ through J and K, and thus on Ψ, written explicitly as $F[\Psi]$, Eq. (2.23) must be solved iteratively. This iterative procedure is known as the *self-consistent field* (SCF) approach. In the n-th iteration of the SCF procedure, we diagonalize the Fock matrix

$$F[\Psi^{(n)}]\,\Psi^{(n+1)} = \Psi^{(n+1)}\varepsilon^{(n+1)} \tag{2.25}$$

and choose the N_e lowest eigenvectors and eigenvalues as the updated coefficients $\Psi^{(n+1)}$ and orbital energies $\varepsilon^{(n+1)}$, respectively. The procedure is iterated until the changes in the expansion coefficients and total energy drop below predefined thresholds (see Fig. 2.3).

Due to the nonlinearity of Eq. (2.26), the simple SCF procedure illustrated in Fig. 2.3 does not always converge.[58,68,69] Depending on the underlying system and the chosen basis set, the procedure may oscillate or even diverge. Over the years, several techniques have been developed to improve the SCF convergence. These methods typically utilize information from multiple iterations to refine the coefficients for the next iteration, which can be mathematically expressed as

$$F[\Psi^{(1)}, \Psi^{(2)}, \ldots \Psi^{(n)}]\,\Psi^{(n+1)} = \Psi^{(n+1)}\varepsilon^{(n+1)}. \tag{2.26}$$

Examples include damping,[58] level shifting,[70] direct inversion of iterative subspace (DIIS),[71,72] quadratically convergent SCF,[73] and more. Furthermore, more accurate initial guesses significantly enhance convergence as well.[68,74,75]

2.4 Correlation-Consistent Methods

Hartree-Fock theory is remarkably successful in computing the ground-state properties of molecules and solids, despite completely neglecting electron correlation effects. Its success stems from the method's variational property, and its relatively low scaling $\mathcal{O}(N^3)$-$\mathcal{O}(N^4)$ with system size. The Hartree-Fock energy E_{HF} typically accounts for approximately 99% of the total energy E_0. However, most experimentally measurable quantities depend on energy differences rather than absolute energies. The missing energy, known as the *correlation energy*, is defined as

$$E_{\text{corr}} = E_0 - E_{\text{HF}} \tag{2.27}$$

and plays a crucial role in accurately predicting these energy differences. In the following, we briefly summarize the widely used correlation-consistent methods in quantum chemistry, as outlined in Table 2.1.

The first attempt to incorporate correlation effects on top of the Hartree-Fock theory is to use the perturbation theory. *Møller-Plesset perturbation theory*[76] (MPPT) treats $\hat{H}_2 - \hat{H}_{\text{MF}}$ as a perturbation term. The first energy correction is obtained using the second-order perturbation (MP2) as

$$E_{\text{MP2}} = -\sum_{ij}\sum_{ab} \frac{\langle ij|ab\rangle \left(2\langle ij|ab\rangle - \langle ij|ba\rangle\right)}{\varepsilon_i + \varepsilon_j - \varepsilon_a - \varepsilon_b}. \tag{2.28}$$

MP2 scales as $\mathcal{O}(N^5)$ due to the required transformation of ERIs into the canonical MO basis. It typically captures 80-90% of the correlation energy and provides reliable relative energies. Consequently, MP2 is often combined with more accurate correlation-consistent methods to estimate the correlation energy in the complete basis set (CBS) limit, especially when these methods become prohibitively expensive for large basis sets.

Configuration interaction (CI) is conceptually the simplest method to incorporate correlation effects. The basic idea is to use Hartree-Fock orbitals to build the basis of Slater determinants and diagonalize the N_e-electron Hamiltonian within that basis. In a one-particle basis of N Hartree-Fock orbitals, we can construct $\binom{N}{N_e}$ Slater determinants by promoting electrons from occupied orbitals to unoccupied (virtual) orbitals. Determinants that differ from $|\Psi_0\rangle$ by n orbitals are called n-tupled excitations. The Hamiltonian matrix elements between these determinants are calculated using Slater-Condon rules,[58,59] and the lowest eigenvalue of the resulting Hamiltonian matrix is the total energy of the system. When all possible $\binom{N}{N_e}$ Slater determinants are included, the method is known as a full configuration interaction (FCI), which yields the exact energy E_0 within the basis set. However, the number of excitations scales exponentially with the system size, making FCI computationally feasible only for the smallest systems (up to 10^{10} Slater determinants).[77]

To address this limitation, numerous approximations have been developed to include only the most significant determinants in the CI expansion. *Configuration interaction singles and doubles* (CISD) restricts the expansion to single and double excitations, as they have non-zero Hamiltonian matrix elements with the reference Hartree-Fock determinant. This truncation reduces the computational cost, resulting in a polynomial scaling $\mathcal{O}(N^6)$ for the CISD method. The CISD wave function is

conveniently expressed in terms of the single and double excitation operators

$$\begin{aligned} \hat{T}_1 &= \sum_{ia} t_i^a \, \hat{a}_a^\dagger \, \hat{a}_i, \\ \hat{T}_2 &= \sum_{ijab} t_{ij}^{ab} \, \hat{a}_a^\dagger \hat{a}_b^\dagger \, \hat{a}_i \hat{a}_j, \end{aligned} \tag{2.29}$$

as

$$|\Phi_{\text{CISD}}\rangle = (1 + \hat{T}_1 + \hat{T}_2) \, |\Psi_0\rangle \, . \tag{2.30}$$

The variational solution of $\hat{H} \, |\Phi_{\text{CISD}}\rangle = E_{\text{CISD}} \, |\Phi_{\text{CISD}}\rangle$ captures approximately 80-90% of the correlation energy, but it lacks size-extensivity, which limits its applicability in practice.

Coupled-cluster (CC) methods employ the exponential ansatz

$$|\Phi_{\text{CC}}\rangle = e^{\hat{T}} \, |\Psi_0\rangle \tag{2.31}$$

to enforce the size-extensivity for any truncation of the cluster operator $\hat{T}$. The most commonly used truncation

$$|\Phi_{\text{CCSD}}\rangle = e^{\hat{T}_1 + \hat{T}_2} \, |\Psi_0\rangle \tag{2.32}$$

is known as *coupled-cluster singles and doubles* (CCSD). The Schrödinger equation $\hat{H} \, |\Phi_{\text{CCSD}}\rangle = E_{\text{CCSD}} \, |\Phi_{\text{CCSD}}\rangle$ is difficult to solve variationally due to the non-linear nature of the exponential ansatz. Instead, it is typically solved using a "projection technique" that generates equations for the single and double amplitudes t_i^a and t_{ij}^{ab}. CCSD generally outperforms CISD since higher excitations are implicitly included through the exponential ansatz. Remarkably, despite its improved accuracy, CCSD scales as $\mathcal{O}(N^6)$, similar to CISD. However, it often fails to achieve chemical accuracy (1 kcal/mol) even for small molecules, highlighting the need for additional corrections.

Coupled-cluster singles, doubles, and triples (CCSDT) is more accurate, but it scales as $\mathcal{O}(N^8)$ with the system size and requires the storage of triple amplitudes t_{ijk}^{abc}. These requirements limit its applicability to the smallest systems. An alternative approach, *coupled-cluster singles, doubles, and perturbative triples* (CCSD(T))[78] includes triples through the perturbation theory, reducing the computational cost to $\mathcal{O}(N^7)$. Moreover, it requires the storage of only double amplitudes t_{ij}^{ab}, making it significantly more practical. CCSD(T) delivers highly accurate energies and, in some cases, even outperforms CCSDT. For this reason, it is widely regarded as the "gold standard" of quantum chemistry. However, CCSD(T) has its limitations as well. It fails for strongly correlated systems, including bond dissociation, transition-metal complexes, or systems with nearly degenerate electronic states. More importantly, its high computational cost restricts its applicability to medium-sized systems with up to 100 electrons in 1000 orbitals.

An alternative approach is offered by *projector quantum Monte Carlo* (PQMC) methods, which are stochastic techniques with favorable computational scaling ranging from $\mathcal{O}(N^4)$ to $\mathcal{O}(N^5)$. These methods are particularly well-suited for large-scale, high-performance computations on modern computer architectures. One of the most widely used PQMC techniques, *fixed-node diffusion Monte Carlo* (FN-DMC)[79,80] has been originally used to compute the correlation energy of the homogeneous electron gas[81], which was crucial for the development of accurate correlation-exchange

Table 2.1: Overview of the most widely used correlation-consistent methods in quantum chemistry. MP2, with $\mathcal{O}(N^5)$ scaling, offers a good balance between accuracy and efficiency. CCSD(T), known as the "gold standard" of quantum chemistry, achieves chemical accuracy for small systems and scales as $\mathcal{O}(N^7)$.

Method	scaling	memory requirements	characteristics
MP2	$\mathcal{O}(N^5)$	$\mathcal{O}(N^3)$	non-variational, size-consistent
CISD	$\mathcal{O}(N^6)$	$\mathcal{O}(N^4)$	variational, size-inconsistent
CCSD	$\mathcal{O}(N^6)$	$\mathcal{O}(N^4)$	non-variational, size-consistent
CCSD(T)	$\mathcal{O}(N^7)$	$\mathcal{O}(N^4)$	non-variational, size-consistent [a]
CCSDT	$\mathcal{O}(N^8)$	$\mathcal{O}(N^7)$	non-variational, size-consistent

[a] The (T) correction is not strictly size-consistent in theory, but in practice, CCSD(T) is size-consistent for most applications.

functionals in density functional theory (DFT). Today, DMC is considered the method of choice for achieving beyond-DFT accuracy in large systems containing a few hundred electrons.[82,83] Another promising PQMC method, *auxiliary-field quantum Monte Carlo* (AFQMC),[6,8] offers favorable scaling and leverages many advantages of traditional quantum chemistry methods. Since AFQMC is the primary focus of this work, the next section is dedicated to a general overview of projector QMC methods.

2.5 Projector Quantum Monte Carlo Methods

Projector quantum Monte Carlo (PQMC) methods, also referred to as Monte Carlo power methods, solve the time-independent many-body Schrödinger equation (Eq. 2.1) using the time-dependent Schrödinger equation in imaginary time

$$-\frac{\partial}{\partial \mathcal{T}} |\Phi(\mathcal{T})\rangle = \hat{H} |\Phi(\mathcal{T})\rangle \tag{2.33}$$

with the formal solution

$$|\Phi(\mathcal{T})\rangle = \hat{P}(\mathcal{T}) |\Phi(0)\rangle = e^{-\mathcal{T}\left(\hat{H}-E_0\right)} |\Phi(0)\rangle\,, \tag{2.34}$$

where $\hat{P}(\mathcal{T})$ is known as the propagator or projector. In the limit of large imaginary time

$$|\Phi\rangle = \lim_{\mathcal{T}\to\infty} \hat{P}(\mathcal{T}) |\Phi_0\rangle\,, \tag{2.35}$$

the exact ground state wave function $|\Phi\rangle$ is filtered out from the initial state $|\Phi_0\rangle = |\Phi(0)\rangle$, provided that the initial state has a nonzero overlap with the ground state, i.e. $\langle\Phi_0|\Phi\rangle \neq 0$.

Since the projector can be accurately computed only in the limit of small time steps τ, the total imaginary time $\mathcal{T}$ is divided into n steps, where $n\tau = \mathcal{T}$. This allows us to express the ground-state wave function as

$$|\Phi\rangle = \lim_{n\to\infty} \hat{P}^n(\tau) |\Phi_0\rangle \tag{2.36}$$

which can be solved iteratively using

$$|\Phi_{k+1}\rangle = \hat{P}(\tau) |\Phi_k\rangle\,. \tag{2.37}$$

It is instructive to expand the last equation in an appropriate complete basis set $\{|q\rangle\}$ to obtain an integral equation

$$\Phi_{k+1}(q') = \int \mathrm{d}q\, G(q'|q)\Phi_k(q). \tag{2.38}$$

Here we define the so-called Green's function[1]

$$G(q'|q) = \langle q'|\hat{P}(\tau)|q\rangle \tag{2.39}$$

and interpret it as a transition kernel that defines the probability of the transition $|q\rangle \to |q'\rangle$. Eq. (2.38) describes the evolution of the probability density $\Phi_k(q)$ over successive iterations and can be solved using Monte Carlo sampling techniques.[84–86] Convergence to the equilibrium density $\Phi(q)$, corresponding to the ground-state wave function, is guaranteed if the transition kernel satisfies the following conditions:

$$G(q'|q) \geq 0 \quad \forall q, q' \qquad\qquad \int \mathrm{d}q'\, G(q'|q) = 1. \tag{2.40}$$

The practical realization of the projector $\hat{P}(\tau)$ and the choice of the state space $\{|q\rangle\}$ lead to different PQMC methods[2](see Table 2.2):

Full configuration interaction quantum Monte Carlo[87,88] (FCIQMC) is formulated in second quantization and employs a complete set of particle-hole excitations $|\Psi_i\rangle$ as the state space. The ground-state wave function is expressed as $|\Phi\rangle = \sum_i W_i |\Psi_i\rangle$, where W_i is an integer weight that represents the number of walkers associated with a specific determinant $|\Psi_i\rangle$. To approximate the short-time propagator, FCIQMC uses a simple forward Euler algorithm $\hat{P}(\tau) \approx (1 - \tau(\hat{H} - E_0))$. The action of $\hat{H}$ on each random walker is implemented stochastically, leading to the birth or death of walkers based on the sign and magnitude of the Hamiltonian matrix elements.

Diffusion Monte Carlo[79,80,89–91] (DMC) operates directly in real-space with a random walker being just a set of $3N_e$ electron coordinates R_{id} that can be interpreted as the eigenstates of the quantum-mechanical position operator

$$|\mathbf{R}\rangle = \prod_{i=1}^{N_e} \prod_{d=1}^{3} \delta(r_{id} - R_{id}). \tag{2.41}$$

The ground-state wave function is represented as a weighted average of walkers $|\Phi\rangle = \sum_w W_w |\mathbf{R}_w\rangle$. DMC uses the exponential projector, with the short-time Green's function

$$G(\mathbf{R}'|\mathbf{R}) = \frac{1}{(2\pi)^{3N_e/2}} e^{-(\mathbf{R}'-\mathbf{R}-V(\mathbf{R})\tau)^2/2\tau} e^{-\tau(E_\mathrm{L}(\mathbf{R})+E_\mathrm{L}(\mathbf{R}')-2E_0)/2}, \tag{2.42}$$

where the first exponential defines the diffusion-like process responsible for the movement of electrons, while the second exponential is interpreted as a

[1] Mathematically, it is not a Green's function.

[2] This is not an exhaustive list, but rather the list of PQMC methods that are routinely used in quantum chemistry.

Table 2.2: The projector quantum Monte Carlo method (PQMC) is characterized by the projector, the state space used to sample the ground state wave function, and the quantization in which it is defined.

Method	projector	state space	quantization
FCIQMC	$(1-\tau(\hat{H}-E_0))$	$\|\Psi_i\rangle$	2nd
DMC	$\exp(-\tau(\hat{H}-E_0))$	$\|\mathbf{R}\rangle$	1st
GFMC	$(1+\tau(\hat{H}-E_0))^{-1}$	$\|\mathbf{R}\rangle$	1st
AFQMC	$\exp(-\tau(\hat{H}-E_0))$	$e^{\hat{T}_1}\|\Psi_0\rangle$	2nd

multiplicative branching factor influencing the walker weights. Here, $V(\mathbf{R})$ is the quantum velocity defined as

$$V(\mathbf{R}) = \frac{\langle \mathbf{R}|\nabla|\Phi_\mathrm{T}\rangle}{\langle \mathbf{R}|\Phi_\mathrm{T}\rangle}, \tag{2.43}$$

and $E_\mathrm{L}(\mathbf{R})$ is the local energy

$$E_\mathrm{L}(\mathbf{R}) = \frac{\langle \mathbf{R}|\hat{H}|\Phi_\mathrm{T}\rangle}{\langle \mathbf{R}|\Phi_\mathrm{T}\rangle} = \frac{\hat{H}\Phi_\mathrm{T}(\mathbf{R})}{\Phi_\mathrm{T}(\mathbf{R})}. \tag{2.44}$$

By sampling the configuration space in imaginary time, DMC dynamically adjusts the walker weights, assigning larger weights to regions of higher importance and smaller or zero weights to less important or forbidden regions.

Green's function Monte Carlo[92,93] (GFMC) is similar to diffusion Monte Carlo, but uses $(1+\tau(\hat{H}-E_0))^{-1}\delta(\mathbf{R}-\mathbf{R}')$ as a projector.

Auxiliary-Field quantum Monte Carlo[1,3,6,8] (AFQMC) is the main focus of this work. For this reason, we dedicate the next chapter to a detailed analysis of the AFQMC algorithm.

Chapter 3

Auxiliary-Field Quantum Monte Carlo

Auxiliary-field quantum Monte Carlo (AFQMC) is a projector technique that extracts the ground-state wave function $|\Phi\rangle$ from any initial state $|\Phi_0\rangle$ through imaginary time propagation

$$|\Phi\rangle = \lim_{n\to\infty} \left[e^{-\tau(\hat{H}-E_0)}\right]^n |\Phi_0\rangle \tag{3.1}$$

provided that $\langle\Phi_0|\Phi\rangle \neq 0$. The initial state $|\Phi_0\rangle$ is typically chosen as the Hartree-Fock Slater determinant. As shown in Eq. (2.37), the above expression can be rewritten in the iterative form as

$$|\Phi_{k+1}\rangle = e^{-\tau(\hat{H}-E_0)} |\Phi_k\rangle , \tag{3.2}$$

which represents the basic building block of the AFQMC method. To develop an efficient AFQMC algorithm, two key components must be defined: (i) the representation of the ground-state wave function $|\Phi_k\rangle$, and (ii) an efficient technique for propagating the many-body wave function $e^{-\tau(\hat{H}-E_0)} |\Phi_k\rangle$.

The first component, the representation of the wave function, is realized using the over-complete space of non-orthogonal Slater determinants. Specifically, we approximate the ground-state wave function $|\Phi_k\rangle$ at time step k as a weighted sum of N_w random walkers

$$|\Phi_k\rangle = \sum_{kw} W_{kw} |\Psi_{kw}\rangle , \tag{3.3}$$

where each walker is represented by a single Slater determinant $|\Psi_{kw}\rangle$, and a complex-valued weight W_{kw}.

With this representation of the wave function, we simplify the imaginary-time propagation of the general many-body wave function to the propagation of N_w single Slater determinants

$$W_{k+1,w} |\Psi_{k+1,w}\rangle = W_{kw}\, e^{-\tau(\hat{H}-E_0)} |\Psi_{kw}\rangle . \tag{3.4}$$

To propagate the random walkers, we employ the second-order split technique (S2)

$$e^{-\tau(\hat{H}-E_0)} \approx e^{-\tau\hat{H}_1/2} e^{-\tau\hat{H}_2} e^{-\tau\hat{H}_1/2} e^{\tau E_0} + \mathcal{O}(\tau^3) \tag{3.5}$$

to separate the one-body propagation from the two-body propagation. In Chapter 5, we will discuss various propagators in detail and explicitly show that the S2 method is optimal for the AFQMC method.

Propagating a single determinant $|\Psi_{kw}\rangle$ with $e^{-\tau\hat{H}_1/2}$ remains a single Slater determinant due to Thouless's theorem,[94,95]

$$\Psi' = e^{-\tau H_1/2}\, \Psi, \tag{3.6}$$

which holds for the exponential of any one-body operator. Here, we use the notation introduced in Section 2.3. Given the fundamental role of Thouless's theorem in the development of AFQMC theory, we provide a detailed derivation in Appendix B.

However, propagating with $e^{-\tau\hat{H}_2}$ is much more challenging. Its application to a single determinant generally produces a linear combination of many Slater determinants, leading to exponential scaling similar to FCI or FCIQMC. In the next section, we demonstrate how the *Hubbard-Stratonovich transformation* addresses this issue and reformulates the problem into an integral equation equivalent to Eq. (2.38), making it suitable for Monte Carlo sampling.

3.1 Hubbard-Stratonovich Transformation

The Hubbard-Stratonovich (HS) transformation[96,97] replaces the two-body propagator with a one-body propagator. This is feasible only for quadratic Hamiltonians and comes at the cost of introducing the integral over auxiliary fields. Effectively, the HS transformation reformulates a many-body problem into a series of mean-field-like calculations, significantly reducing computational complexity.

As we argue that a deep understanding of the Hubbard-Stratonovich transformation is essential to fully grasp the AFQMC method, we provide an explicit proof for the HS transformation of the simplest quadratic Hamiltonian $\hat{H} = \hat{L}^2$:

$$e^{-\tau\hat{L}^2/2} = \int \mathrm{d}x \, \frac{e^{-x^2/2}}{\sqrt{2\pi}} \, e^{i\sqrt{\tau}x\hat{L}}, \tag{3.7}$$

where $\hat{L}$ is any one-body operator.
Proof:
To prove this identity, we first multiply the right-hand side by $e^{-\tau\hat{L}^2/2}e^{\tau\hat{L}^2/2}$ to complete the square

$$e^{-\tau\hat{L}^2/2} = \int \mathrm{d}x \, \frac{e^{-x^2/2}\, e^{i\sqrt{\tau}x\hat{L}}\, e^{\tau\hat{L}^2/2}}{\sqrt{2\pi}} \, e^{-\tau\hat{L}^2/2} = e^{-\tau\hat{L}^2/2} \int \mathrm{d}x \, \frac{e^{-(x-i\sqrt{\tau}\hat{L})^2/2}}{\sqrt{2\pi}}. \tag{3.8}$$

By substituting $u = x - i\sqrt{\tau}\hat{L}$, and integrating over u, we obtain:

$$e^{-\tau\hat{L}^2/2} = e^{-\tau\hat{L}^2/2} \int \mathrm{d}u \, \frac{e^{-u^2/2}}{\sqrt{2\pi}} = e^{-\tau\hat{L}^2/2}, \tag{3.9}$$

which completes the proof.

For a general many-body Hamiltonian (Eq. 2.4), we rewrite the two-body part as a sum of quadratic terms

$$\hat{H}_2 = \frac{1}{2}\sum_g^{N_g} \hat{L}_g^2 \tag{3.10}$$

by introducing Cholesky vectors as explicitly shown in Eq. (2.10). In this case, the Hubbard-Stratonovich transformation is exact only in the limit of small time steps

$$\begin{aligned} e^{-\tau\hat{H}_2} = e^{-\tau\sum_g \hat{L}_g^2/2} &= \int \mathrm{d}^{N_g}x \, \frac{e^{-\sum_g x_g^2/2}}{(2\pi)^{N_g/2}} \, e^{i\sqrt{\tau}\sum_g x_g \hat{L}_g} + \mathcal{O}(\tau^2) \\ &= \int \mathrm{d}\mathbf{x} \, p(\mathbf{x}) \, e^{-\tau\mathcal{H}(\mathbf{x})} + \mathcal{O}(\tau^2), \end{aligned} \tag{3.11}$$

or in the case of commuting $\hat{L}_g$ operators. For brevity, we define the N_g-dimensional standard normal distribution $p(\mathbf{x})$, and an effective one-body interaction

$$\hat{\mathcal{H}}(\mathbf{x}) = \frac{i}{\sqrt{\tau}} \sum_g x_g \hat{L}_g. \tag{3.12}$$

By inserting Eq. (3.11) into Eq. (3.4), we obtain an update equation for the walkers

$$W_{k+1,w} \left|\Psi_{k+1,w}\right\rangle = \int \mathrm{d}\mathbf{x}\; p(\mathbf{x}) \hat{B}(\mathbf{x})\; W_{kw} \left|\Psi_{kw}\right\rangle, \tag{3.13}$$

where $\hat{B}(\mathbf{x})$ is the HS-transformed one-body propagator

$$\hat{B}(\mathbf{x}) = e^{-\tau \hat{H}_1/2} e^{-\tau \hat{\mathcal{H}}(\mathbf{x})} e^{-\tau \hat{H}_1/2} e^{\tau E_0}. \tag{3.14}$$

The integral over auxiliary fields is evaluated using Monte Carlo integration, as described in Appendix C. However, naive Monte Carlo sampling is typically too noisy for all non-trivial cases. To mitigate the noise, various variance-reduction techniques can be applied. In the following section, we introduce three such techniques: importance sampling using the trial wave function, mean-field subtraction, and importance sampling with force bias.

3.2 Importance Sampling in Auxiliary-Field Quantum Monte Carlo

Importance sampling is among the most commonly used variance-reduction techniques in Monte Carlo methods. The core idea is to concentrate Monte Carlo samples in the most important regions of the configuration space. For a detailed explanation of the fundamental principles, see Appendix D.

In this section, we examine three importance sampling techniques used in AFQMC: (i) trial wave function, (ii) mean-field subtraction, and (iii) force bias.

3.2.1 Trial Wave Function

The trial wave function guides AFQMC walkers toward the most relevant regions of the configuration space, enhancing sampling efficiency and reducing variance. Following the notation established in Appendix A, we use $|\Psi_\mathrm{T}\rangle$ to denote special expressions for the single-determinantal trial wave function and $|\Phi_\mathrm{T}\rangle$ for a general case whenever applicable. Any approximation of the exact ground-state wave function $|\Phi\rangle$ can be used as a trial wave function. The most straightforward choices include the Hartree-Fock determinant $|\Psi_0\rangle$ or a determinant constructed from Kohn-Sham orbitals.

Let us consider a single time-step propagation of an AFQMC walker:

$$W' \left|\Psi'\right\rangle = \int \mathrm{d}\mathbf{x}\; p(\mathbf{x}) \hat{B}(\mathbf{x})\; W \left|\Psi\right\rangle. \tag{3.15}$$

After multiplying the left-hand side by $\langle\Phi_\mathrm{T}|\Psi'\rangle \,/\, \langle\Phi_\mathrm{T}|\Psi'\rangle$ and the right-hand side by $\langle\Phi_\mathrm{T}|\Psi\rangle \,/\, \langle\Phi_\mathrm{T}|\Psi\rangle$, we obtain

$$W' \left\langle\Phi_\mathrm{T}|\Psi'\right\rangle \left|\Psi'\right\rangle = \int \mathrm{d}\mathbf{x}\; p(\mathbf{x}) \hat{B}(\mathbf{x}) \frac{\langle\Phi_\mathrm{T}|\Psi'\rangle}{\langle\Phi_\mathrm{T}|\Psi\rangle}\; W \left\langle\Phi_\mathrm{T}|\Psi\right\rangle \left|\Psi\right\rangle \tag{3.16}$$

If we now redefine weights as $W \to \langle \Phi_T | \Psi \rangle W$, the walker update equation changes to

$$W' |\Psi'\rangle = \int \mathrm{d}\mathbf{x}\; p(\mathbf{x})\, \hat{B}(\mathbf{x}) \frac{\langle \Phi_T | \Psi' \rangle}{\langle \Phi_T | \Psi \rangle} W |\Psi\rangle . \tag{3.17}$$

In the practical implementation of importance sampling, the update of the walker determinant $|\Psi\rangle$ remains unchanged, while the walker weight is additionally updated as

$$W' = W \frac{\langle \Phi_T | \Psi' \rangle}{\langle \Phi_T | \Psi \rangle}. \tag{3.18}$$

In this way, walkers with a larger overlap with the trial wave function acquire larger weights, leading to their accumulation in the most important regions of the configuration space—provided the trial wave function is sufficiently close to the exact ground state. In most cases, even the simplest choice, such as the Hartree-Fock determinant, significantly improves the AFQMC sampling variance.

3.2.2 Mean-Field Subtraction

Another approach to improve AFQMC sampling is to minimize $\hat{H}_2$, which in turn reduces the effective interaction $\mathcal{H}(\mathbf{x})$, and decreases fluctuations in the random walk. While the total Hamiltonian cannot be modified, its terms can be rearranged to make $\hat{H}_2$ "smaller". To achieve this, we introduce a mean-field shift

$$\bar{l}_g = \frac{\langle \Phi_T | \hat{L}_g | \Phi_T \rangle}{\langle \Phi_T | \Phi_T \rangle} \tag{3.19}$$

to rewrite the two-body Hamiltonian as

$$\hat{H}_2 = \frac{1}{2}\sum_g \hat{L}_g^2 = \frac{1}{2}\sum_g \left(\hat{L}_g - \bar{l}_g\right)^2 + \sum_g \bar{l}_g \hat{L}_g - \frac{1}{2}\sum_g \bar{l}_g^2. \tag{3.20}$$

This identity holds for any real shift $\bar{l}_g$. The second term represents a one-body operator, while the third term is an energy shift. In the special case of a Hartree-Fock trial wave function, these terms correspond to the Hartree potential (Eq. 2.22) and the Hartree energy, respectively.

With this rearrangement, the new Hamiltonian terms $\hat{H} = H_0 + \hat{H}_1 + \hat{H}_2$ are defined as

$$\begin{aligned} H_0 &\to H_0 - \frac{1}{2}\sum_g \bar{l}_g^2 \\ \hat{H}_1 &\to \hat{H}_1 + \sum_g \bar{l}_g \hat{L}_g \\ \hat{H}_2 &\to \frac{1}{2}\sum_g \left(\hat{L}_g - \bar{l}_g\right)^2 \end{aligned} \tag{3.21}$$

compared to the previous defintion in Eq. (2.10). Here we introduce the energy shift H_0 to account for the shift introduced by the mean-field subtraction.

Applying the Hubbard-Stratonovich transformation to the modified two-body Hamiltonian changes the HS-transformed propagator to

$$\hat{B}(\mathbf{x}) = e^{-\tau \hat{H}_1/2} e^{-\tau \hat{\mathcal{H}}(\mathbf{x})} e^{-\tau \hat{H}_1/2} e^{-\tau (H_0 - E_0)} \tag{3.22}$$

with the modified effective interaction

$$\hat{\mathcal{H}}(\mathbf{x}) = \frac{i}{\sqrt{\tau}} \sum_g x_g \left(\hat{L}_g - \bar{l}_g\right). \tag{3.23}$$

The implementation of mean-field subtraction requires only the precomputation of the shift $\bar{l}_g$ at the beginning of the AFQMC simulation. This incurs no additional computational cost while substantially reducing AFQMC sampling variance. Consequently, we apply mean-field subtraction in all AFQMC simulations reported in this work. Furthermore, whenever referring to the propagator $\hat{B}(\mathbf{x})$ or the interaction $\hat{\mathcal{H}}(\mathbf{x})$, we implicitly assume their forms after mean-field subtraction.

3.2.3 Force Bias

Similar to mean-field subtraction, where the mean-field Hartree potential is subtracted from the $\hat{H}_2$ term, we can take a step further and subtract the instantaneous Hartree potential generated by the walker determinant $|\Psi\rangle$:

$$\hat{J} = \sum_g l_g \hat{L}_g, \tag{3.24}$$

where l_g is the mixed estimator

$$l_g = \langle \hat{L}_g \rangle = \frac{\langle \Phi_T | \hat{L}_g - \bar{l}_g | \Psi \rangle}{\langle \Phi_T | \Psi \rangle}. \tag{3.25}$$

The calculation of l_g will be discussed in more detail in the following section and Section 4.3.

To incorporate instantaneous mean-field subtraction into the AFQMC random walk, we follow the importance sampling transformation introduced in Appendix D. Consider the mixed expectation value[1] of the Hubbard-Stratonovich transformed propagator defined in Eq. (3.11):

$$\begin{aligned} \int \mathrm{d}\mathbf{x}\; p(\mathbf{x})\; \langle e^{-\tau \hat{\mathcal{H}}(\mathbf{x})} \rangle &= \int \mathrm{d}\mathbf{x}\; p(\mathbf{x}-\mathbf{f})\; \langle e^{-\tau \hat{\mathcal{H}}(\mathbf{x})} \rangle\; \frac{p(\mathbf{x})}{p(\mathbf{x}-\mathbf{f})} \\ &= \int \mathrm{d}\mathbf{x}\; p(\mathbf{x}-\mathbf{f})\; \langle e^{-\tau \hat{\mathcal{H}}(\mathbf{x})} \rangle\; R(\mathbf{x},\mathbf{f}), \end{aligned} \tag{3.26}$$

where $p(\mathbf{x}-\mathbf{f})$ is the proposal distribution

$$p(\mathbf{x}-\mathbf{f}) = \frac{e^{-(\mathbf{x}-\mathbf{f})^2/2}}{(2\pi)^{N_g/2}} = \frac{e^{-\sum_g (x_g - f_g)^2/2}}{(2\pi)^{N_g/2}}, \tag{3.27}$$

and $R(\mathbf{x},\mathbf{f})$ is the ratio of the target and proposal distributions

$$R(\mathbf{x},\mathbf{f}) = \frac{p(\mathbf{x})}{p(\mathbf{x}-\mathbf{f})} = e^{-\mathbf{x}\mathbf{f}} e^{\mathbf{f}^2/2} = e^{-\sum_g x_g f_g}\; e^{\sum_g f_g^2/2} \tag{3.28}$$

known as the importance sampling reweighting factor (see Appendix D).

[1] Expectation values of the form $\frac{\langle \Phi_T | \hat{O} | \Psi \rangle}{\langle \Phi_T | \Psi \rangle}$ where bra and ket states differ, are known as mixed expectation values.

This transformation is valid for any choice of the *force bias* $\mathbf{f}$, but Zhang *et. al.*[8] demonstrated that

$$f_g = i\sqrt{\tau}\,\langle \hat{L}_g - \bar{l}_g \rangle = i\sqrt{\tau}\,\frac{\langle \Phi_T | \hat{L}_g - \bar{l}_g | \Psi \rangle}{\langle \Phi_T | \Psi \rangle} = i\sqrt{\tau}\,(l_g - \bar{l}_g) \tag{3.29}$$

minimizes the fluctuations of $\langle e^{-\tau \hat{\mathcal{H}}(\mathbf{x})} \rangle$ and leads to a more stable random walk. Specifically, the dominant imaginary part of the propagator proportional to $\sqrt{\tau}$, is explicitly canceled. This is conveniently showed by expanding $\langle e^{-\tau \hat{\mathcal{H}}(\mathbf{x})} \rangle$ and $R(\mathbf{x},\mathbf{f})$ to first order in $\sqrt{\tau}$:

$$1 - \sum_g i\sqrt{\tau} x_g \,\langle \hat{L}_g - \bar{l}_g \rangle = 1 - \sum_g x_g f_g, \tag{3.30}$$

where we used Eq. (3.23) to expand $\hat{\mathcal{H}}(\mathbf{x})$ This directly leads to the definition of the force bias given in Eq. (3.29).

Substituting back Eq. (3.26) into the walker update equation (Eq. 3.17) yields

$$W' \,|\Psi'\rangle = \int \mathrm{d}\mathbf{x}\; p(\mathbf{x}-\mathbf{f})\, \hat{B}(\mathbf{x})\, \frac{\langle \Phi_T | \Psi' \rangle}{\langle \Phi_T | \Psi \rangle} R(\mathbf{x},\mathbf{f})\; W\,|\Psi\rangle\,. \tag{3.31}$$

This equation can be interpreted as follows: random numbers $\mathbf{x}$ are sampled from the distribution $p(\mathbf{x}-\mathbf{f})$ and used to propagate the walker determinant as $|\Psi'\rangle = \hat{B}(\mathbf{x})\,|\Psi\rangle$. Finally, the walker weight is updated as $W' = W\,\frac{\langle \Phi_T | \Psi' \rangle}{\langle \Phi_T | \Psi \rangle} R(\mathbf{x},\mathbf{f})$.

For practical implementation, $\mathbf{f}$ must be accessible for each walker. Unlike mean-field subtraction, the walker-dependent force bias introduces an additional computational overhead to the AFQMC procedure. However, the cost of evaluating the force bias is identical to that of computing the Hartree energy and is significantly lower than that of computing the exchange energy or performing AFQMC propagation (see Sect. 4.3).

3.3 Energy Estimators in Auxiliary-Field Quantum Monte Carlo

The total AFQMC energy of the system is computed as a weighted average of local energies over all time steps and walkers

$$\bar{E}_0 = \frac{\sum_{kw} W_{kw}\, E_L(\Psi_{kw})}{\sum W_{kw}} = \frac{\sum_k W_k E_k}{\sum_k W_k}, \tag{3.32}$$

where W_k and E_k are the average weight and the average energy at time step k, respectively:

$$W_k = \frac{1}{N_w}\sum_w W_{kw}, \qquad\qquad E_k = \frac{\sum_w W_{kw} E_L(\Psi_{kw})}{\sum_w W_{kw}}. \tag{3.33}$$

For a detailed explanation of the computation of these averages and their corresponding statistical errors in AFQMC, see Appendix E.

The *local energy* estimator for a single-determinant trial wave function is evaluated using the non-orthogonal Wick theorem[98] as

$$E_{\mathrm{L}}(\Psi_{kw}) = \frac{\langle \Psi_{\mathrm{T}}|\hat{H}|\Psi_{kw}\rangle}{\langle \Psi_{\mathrm{T}}|\Psi_{kw}\rangle} = 2\sum_{pq} t_{pq}G_{pq} + \sum_{pqrs}\langle pq|rs\rangle\left(2G_{pr}G_{pq} - G_{ps}G_{qr}\right), \quad (3.34)$$

where the terms correspond to the one-body energy, Hartree energy, and exchange energy, respectively. The interstate density matrix G, a generalization of the reduced one-body density matrix D defined in Section 2.3, is given by

$$G_{pq}(\Psi) = \frac{\langle \Psi_{\mathrm{T}}|\hat{a}_p^\dagger \hat{a}_q|\Psi\rangle}{\langle \Psi_{\mathrm{T}}|\Psi\rangle} = \left(\Psi\left(\Psi_{\mathrm{T}}^\dagger\Psi\right)^{-1}\Psi_{\mathrm{T}}^\dagger\right)_{qp}. \quad (3.35)$$

The evaluation of local energies is computationally the most expensive part of the AFQMC procedure, scaling quartically with the system size. This will be discussed in more detail in Chapter 4.

The naive generalization of the local energy expression to the multideterminantal trial wave functions $|\Phi_{\mathrm{T}}\rangle = \sum_\alpha^{N_d} c_\alpha |\Psi_\alpha\rangle$ is given by

$$E_{\mathrm{L}}(\Psi_{kw}) = \frac{\langle \Phi_{\mathrm{T}}|\hat{H}|\Psi_{kw}\rangle}{\langle \Phi_{\mathrm{T}}|\Psi_{kw}\rangle} = \frac{\sum_\alpha^{N_d} c_\alpha^* \langle \Psi_\alpha|\Psi_{kw}\rangle \frac{\langle \Psi_\alpha|\hat{H}|\Psi_{kw}\rangle}{\langle \Psi_\alpha|\Psi_{kw}\rangle}}{\sum_\alpha^{N_d} c_\alpha^* \langle \Psi_\alpha|\Psi_{kw}\rangle}, \quad (3.36)$$

which scales linearly with the number of determinants in the trial state. This equation is used to evaluate local energies for non-orthogonal multideterminantal trial wave functions (NOMSD). In contrast, for particle-hole multi-Slater determinants (PHMSD), there are efficient local energy evaluation techniques[46–49] that achieve sublinear scaling with the number of determinants. Further details about multideterminantal trial wave functions will be discussed in Chapter 6.

The *hybrid energy*, an alternative energy estimator as proven explicitly in Appendix F, is cheaper to compute

$$E_{\mathrm{H}}(\Psi_{kw}) = -\frac{1}{\tau}\log\frac{\langle \Phi_{\mathrm{T}}|\Psi_{k+1,w}\rangle}{\langle \Phi_{\mathrm{T}}|\Psi_{kw}\rangle} R(\mathbf{x}_{kw}, \mathbf{f}_{kw}), \quad (3.37)$$

but it is also less accurate than the local energy estimator. This is illustrated in Fig. 3.1, which compares the distributions of local and hybrid energies in a typical AFQMC simulation. In general, the variance of the hybrid energy estimator is an order of magnitude larger than that of the local energy estimator, as evidenced by the heavier tails in the hybrid energy.

However, the computation of the hybrid energy requires only the evaluation of overlaps between Slater determinants, resulting in cubic scaling for a single-determinant trial wave function. The hybrid energy has a strong dependence on the time step and provides a reliable energy estimator only in the limit of small time steps, as proven in Appendix F. Despite this limitation, the hybrid energy plays a crucial role in AFQMC weight updates, as demonstrated in the following two sections. Additionally, since the hybrid energy is estimated from the propagated walker determinant, it serves as a useful tool for verifying AFQMC propagation.

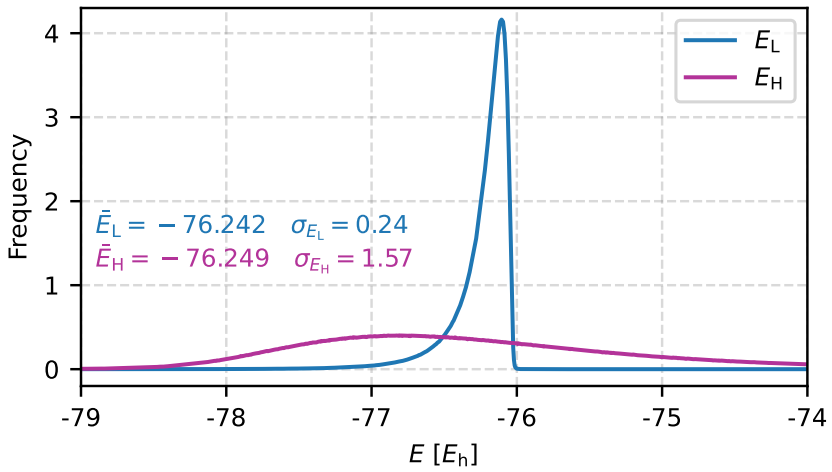

Figure 3.1: The hybrid energy estimator E_H exhibits a larger variance than the local energy estimator E_L. In a typical AFQMC simulation with force bias, the variance of E_H is an order of magnitude larger than that of E_L. The error in the average hybrid energy E_H arises from the relatively large time step $\tau = 0.01\, E_h^{-1}$ used for AFQMC propagation.

3.4 Free-Projection Auxiliary-Field Quantum Monte Carlo

After introducing the trial wave function and mean-field subtraction, we can define the first equations of motion for the walkers:

$$|\Psi_{k+1,w}\rangle = \hat{B}(\mathbf{x}_{kw})\,|\Psi_{kw}\rangle\,, \tag{3.38}$$

$$W_{k+1,w} = W_{kw}\, e^{-\tau E_H(\Psi_{kw})}, \tag{3.39}$$

which form the basis of the *free-projection auxiliary-field quantum Monte Carlo* (fp-AFQMC) method. Note that fp-AFQMC is typically implemented without force bias ($f_g = 0$), and the weights are updated using the hybrid energy estimator (Eq. 3.37).

Fig. 3.2 (top) illustrates the typical flow of an fp-AFQMC simulation using the example of an H_2O molecule in the cc-pVDZ basis set. Every AFQMC simulation begins with an equilibration phase, during which the energy estimator rapidly converges from the trial energy E_T to the true ground-state energy E_0. The simulation then transitions to the sampling phase, where the AFQMC energy E_k at time step k fluctuates around a fixed value. In principle, the estimated energy average $\bar{E}_0$ should approach the exact ground-state energy E_0. However, as the number of time steps increases, $\bar{E}_0$ begins to fluctuate again, which is a manifestation of the fermionic sign problem—commonly referred to as the phase problem within the AFQMC framework. For more details on the AFQMC simulation flow and statistical data analysis, see Appendix E.

The phase problem in AFQMC is less severe compared to real-space projector Monte Carlo methods, where the projector converges to the bosonic ground state rather than the fermionic one. In AFQMC, the antisymmetric nature of the sampled ground state is ensured by construction. However, the phase problem is not entirely eliminated. During the AFQMC walk, the walker weights populate the entire complex

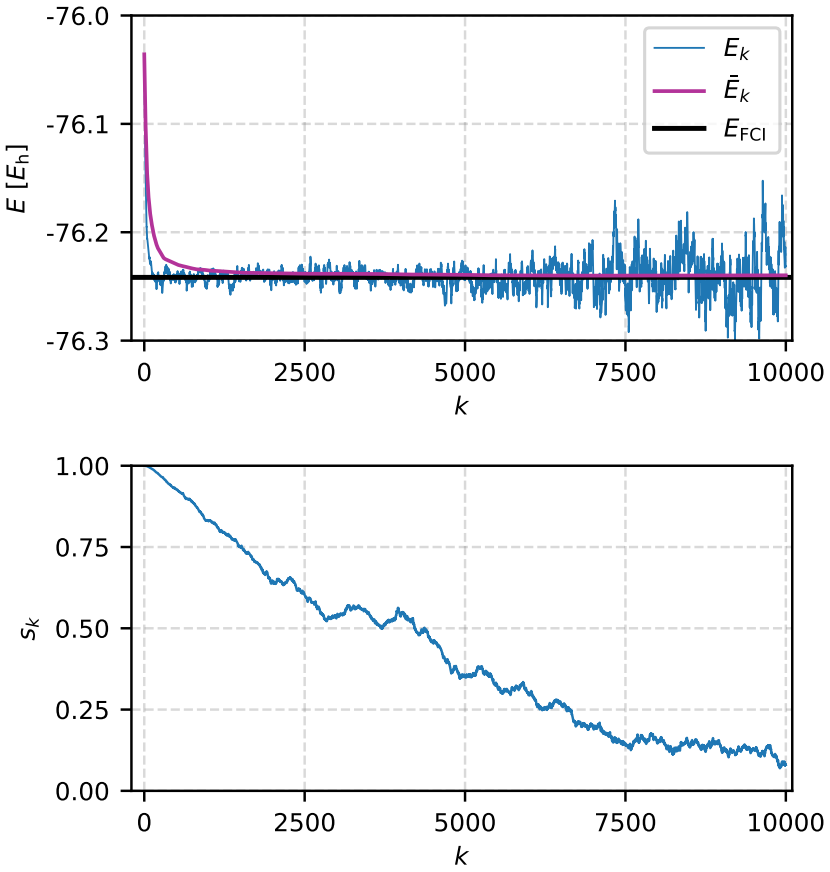

Figure 3.2: (Top) Typical behavior of the local energy E_k at time step k (blue line) and the running local energy average (magenta line) in an fp-AFQMC simulation. The variance of E_k increases with increasing k. (Bottom) The average sign s_k decreases throughout the fp-AFQMC simulation. As $N_w s_k$ approaches zero, the fp-AFQMC simulation becomes unstable, and the denominator in Eq. (3.32) averages to zero.

plane uniformly, causing the denominator in Eq. (3.32) to average to zero. This is illustrated in Fig. 3.3, which shows the distribution of walker phases θ_{kw}[2] at different time steps k. As k increases, θ_{kw} becomes uniformly distributed, effectively reducing the number of samples from N_w to $N_w s_k$, where s_k is the average sign at time step k, defined as

$$s_k = \frac{\sum_w |W_{kw}| e^{i\theta_{kw}}}{\sum_w |W_{kw}|}. \tag{3.40}$$

As s_k approaches zero, fp-AFQMC becomes unstable, as illustrated in Fig. 3.2. Therefore, fp-AFQMC simulations are usually performed with as many walkers as possible and as few time steps as possible, ensuring that $N_w s_k$ does not approach zero during the run. Other strategies to slow the decay of s_k include using more accurate trial wave functions or improving importance sampling. The inclusion of force bias is an excellent candidate, although it requires additional algorithmic improvements to be stable in practice,[47,49] since the force bias (Eq. 3.29) diverges as walkers become orthogonal to the trial wave function.

[2]The phase θ_{kw} is defined as $W_{kw} = |W_{kw}| e^{i\theta_{kw}}$

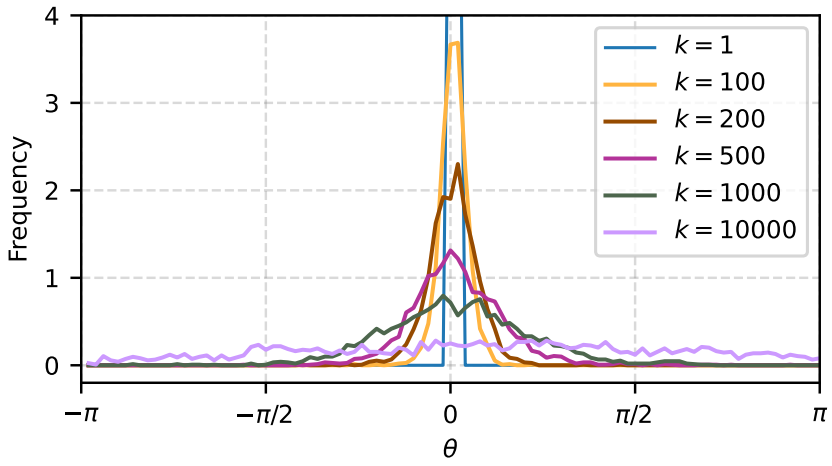

Figure 3.3: The distribution of walker phases θ_{kw} evolves from an initial delta distribution at timestep $k = 1$ to a uniform distribution at timestep $k = 10000$, illustrating the emergence of the phase problem in fp-AFQMC simulations. The phase distributions are depicted for several k values.

3.5 Phaseless Approximation: Phaseless Auxiliary-Field Quantum Monte Carlo

To suppress the phase problem in AFQMC, it is sufficient to ensure that the reweighting factor in Eq. (3.39) remains real-valued and positive. While the addition of force bias significantly reduces the imaginary part of walker weights, it does not eliminate it completely. To further address this, Zhang *et. al.*[8] proposed additional constraints:

$$|\Psi_{k+1,w}\rangle = \hat{B}(\mathbf{x}_{kw})\,|\Psi_{kw}\rangle \tag{3.41}$$

$$W_{k+1,w} = W_{kw}\, e^{-\tau \mathrm{Re}E_{\mathrm{H}}(\Psi_{kw})}\, \max(0, \cos(\Delta\theta)), \tag{3.42}$$

where the phase change $\Delta\theta$ is defined as

$$\Delta\theta = \mathrm{Im}\log \frac{\langle \Phi_{\mathrm{T}}|\Psi_{k+1,w}\rangle}{\langle \Phi_{\mathrm{T}}|\Psi_{kw}\rangle}. \tag{3.43}$$

These equations define phaseless AFQMC (ph-AFQMC), which effectively mitigates the phase problem but introduces a systematic bias known as the *phaseless error*. Unlike fp-AFQMC, ph-AFQMC yields consistent results only if the force bias is employed. Therefore, throughout this work, whenever we refer to ph-AFQMC calculations, we implicitly assume that the force bias is included.

Fig. 3.4 illustrates a typical ph-AFQMC simulation (magenta line) for an H_2O molecule using the cc-pVDZ basis set. Compared to fp-AFQMC (blue line), ph-AFQMC remains stable in the limit of long imaginary times; however, ph-AFQMC energy does not necessarily converge to the exact ground-state energy E_0 as it includes an uncontrolled bias. In the case of the H_2O molecule, the phaseless error is negligible, but it will be systematically studied in Chapter 4 for the Hartree-Fock trial wave function and in Chapter 6 for multideterminantal trial wave functions.

Several alternative constraints have been proposed in the literature[41,99,100] One of them will be discussed in more detail in Chapter 4. However, it remains unclear

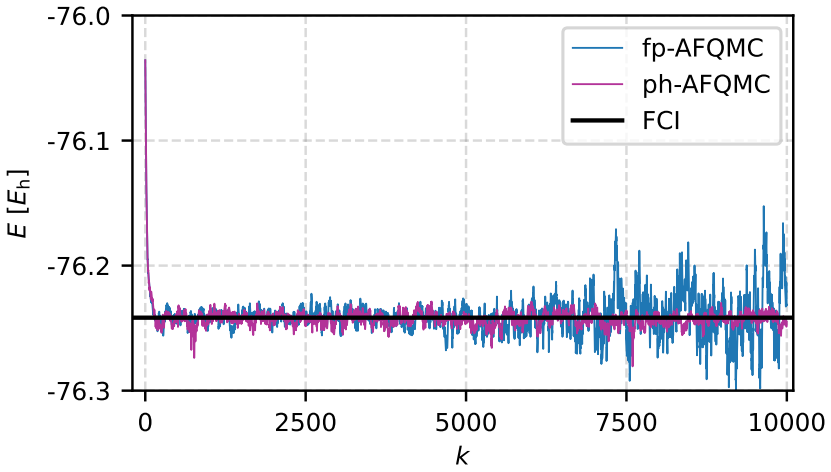

Figure 3.4: The phaseless approximation stabilizes AFQMC energies at large imaginary times ($k \geq 5\,000$), but introduces a systematic error known as the *phaseless bias*.

whether these alternative constraints yield better results than the original phaseless approximation.

3.6 Further Stabilization of the AFQMC Method

The AFQMC algorithm described so far remains unstable in the limit of long imaginary times, even within the phaseless regime. In this section, we introduce additional stabilization techniques that are routinely applied in AFQMC: walker reconfiguration and walker reorthogonalization. Furthermore, the control of rare events will be discussed in Chapter 5.

3.6.1 Walker Reconfiguration

Despite importance sampling techniques, some AFQMC walkers acquire large weights, while others remain very small. Simulating a large number of walkers with small weights leads to inefficient sampling, as indicated by Eq. (3.32). To address this, a periodic reconfiguration of walkers is required, where walkers with large weights are replicated, while those with small weights are removed from the simulation.

We employ a comb method[101] that preserves the total number of walkers. To perform the comb reconfiguration of N_w AFQMC walkers $\{W_w, \Psi_w\}$, we first compute the normalized weights

$$w_w = \frac{N_w}{\sum_v W_v} W_w \tag{3.44}$$

ensuring the normalization $\sum_w w_w = N_w$. The goal is to determine an integer function $\sigma(w)$ that defines the reconfiguration of walkers

$$\Psi_w \to \Psi'_w = \Psi_{\sigma(w)}, \tag{3.45}$$

where $\sigma(w) = v$ occurs approximately w_v times.

To illustrate the process, we map the walkers onto a one-dimensional grid of length N_w, where the length of each segment (i.e., walker) corresponds to its weight w_w as illustrated in Fig. 3.5 with a blue line. This grid is then compared with an equidistant grid of the same length, shifted to the left by a uniformly distributed random number $\zeta \in [0,1)$ (in gray). The nodes $w \in [1,2,\ldots,N_w]$ of the equidistant grid intersect the walker grid, and the intersections determine the indices of the replicated walkers, i.e., the desired function $\sigma(w)$. After reconfiguration, all walker weights are reset to one, as illustrated with the magenta grid. The Python implementation of the comb reconfiguration is presented in the listing below.

The inclusion of the random number ζ ensures that $\sigma(N_w)$ is not necessarily equal to N_w, regardless of the walker weights. Without this randomization, the last walker could never be reconfigured (except in the extreme case $w_{N_w} = 0$), introducing bias into the process.

Regardless of this issue, the reconfiguration process inherently introduces a bias that decreases as N_w^{-1} and vanishes in the limit of infinitely many walkers.[84] Fig. 3.6 illustrates the reconfiguration bias in a typical ph-AFQMC simulation. The bias is relatively small and becomes essentially negligible with as few as 24 walkers.

For fp-AFQMC, we expect a larger reconfiguration bias since weights are complex-valued. To address this, we use the weight magnitude $|W_w|$ in the reconfiguration process. However, since fp-AFQMC calculations are typically performed with a very large number of walkers—allowing for fewer time steps to mitigate the sign problem—the reconfiguration bias is expected to be negligible in these calculations as well.

Several alternative reconfiguration methods have been proposed in the literature.[84,85]. Among these, we find that the comb method is the best choice for AFQMC because: (I) the number of walkers N_w is kept constant; (ii) it introduces a relatively small bias with respect to N_w (see Fig. 3.6); (iii) statistical errors are well-controlled and decrease as $(N_w N_k)^{-1/2}$ with the total number of samples; and (iv) it minimizes the randomness, as the entire reconfiguration process depends on a single random number.

```python
import numpy as np

def reconfigure_walkers(walkers):
    sigma = comb_reconfiguration(walkers.weights)
    walkers = walkers[sigma]
    walkers.weights = 1.0
    return walkers

def comb_reconfiguration(weights):
    """
    Comb reconfiguration method:
    input:
        weights - real array of walker weights
    output:
        sigma - integer array needed for the reconfiguration:
            walkers[w] = walkers[sigma[w]]
    """

    nwalkers = np.size(weights)

    #normalize weights
    weights = weights / np.sum(weights) * nwalkers

    weight_sum = -np.random.rand()
    previous = 0

    for w in range(nwalkers):
        weight_sum += weights[w]
        current = int(np.ceil(weight_sum))
        sigma[w] = current - previous
        previous = current

    return np.cumsum(sigma)
```

3.6.2 Walker Reorthogonalization

The AFQMC propagator is non-unitary because AFQMC operates in imaginary time. As a result, the propagated walker orbitals are not inherently orthonormal, and repeated application of the Hubbard-Stratonovich transformed propagator can lead to the accumulation of truncation errors.

To prevent numerical instabilities, periodic reorthogonalization of walkers is required. This is achieved by transforming the walker orbitals as

$$\Psi \to \Psi' = \Psi T \tag{3.46}$$

where T is an arbitrary $N_e \times N_e$ matrix. Such transformations alter the Slater de-

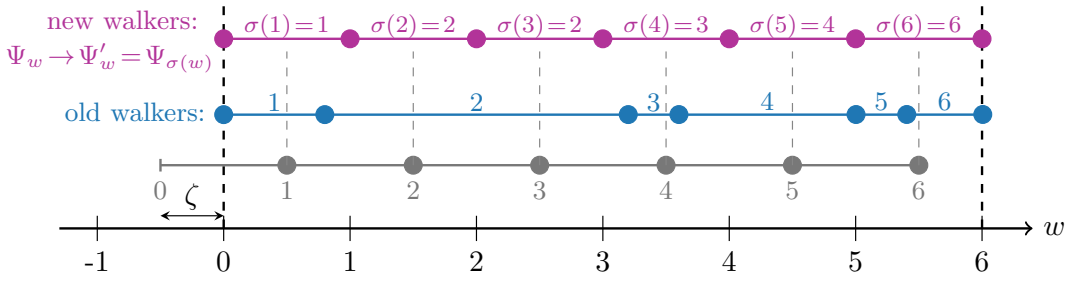

Figure 3.5: Illustration of the comb reconfiguration method.[101] The blue line represents walkers, where the segment length corresponds to the walker's weight. The gray line is an equidistant grid, shifted to the left by a uniformly distributed random number ζ. The gray nodes $[1,2,\ldots,N_w]$ intesect blue segments, determining the indices $[\sigma(1),\sigma(2),\ldots,,\sigma(N_w)]$ of the reconfigured walkers illustrated with the magenta grid. The walker weights of the reconfigured walkers are reset to 1. In this example, the original walkers $[1,2,3,4,5,6]$ are replaced with walkers $[1,2,2,3,4,6]$, meaning walker 2 is replicated, while the walker 5 is removed from the simulation. Note that without the random shift ζ, the last walker would always survive reconfiguration as long as $w_{N_w} > 0$.

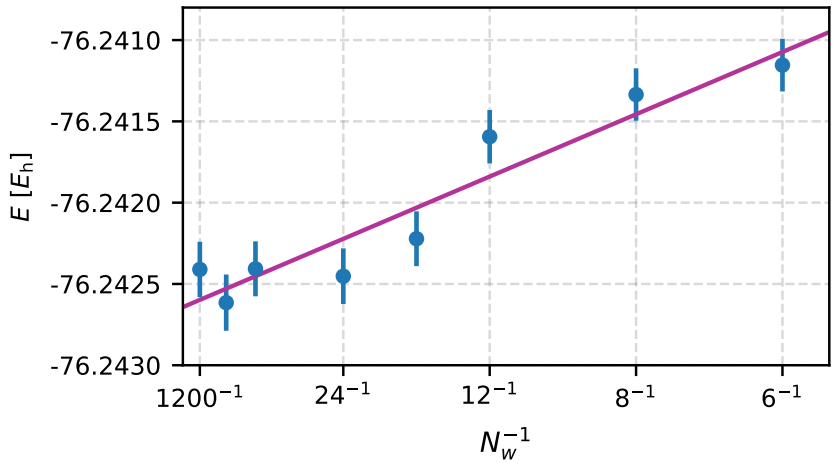

Figure 3.6: The reconfiguration bias is inversely proportional to the number of walkers N_w. For the comb reconfiguration method, the bias becomes negligible with as few as 24 walkers in a typical ph-AFQMC simulation. (The simulations were performed for the H_2O molecule using the cc-pVDZ basis set.)

terminant only by an overall constant factor $\det(T)$[3] and do not affect expectation values.

QR Orthogonalization

Gram-Schmidt orthogonalization is the simplest method for orthogonalizing orbitals, but it is neither the most efficient nor the most numerically stable choice. A more robust approach employs the QR decomposition[102] of the walker determinant

$$\Psi = \Psi' R, \tag{3.47}$$

where Ψ' is the $N \times N_e$ part of the unitary matrix, and R is a $N_e \times N_e$ upper triangular matrix. The walker orbitals Ψ are then replaced by the orthonormal orbitals Ψ', while the walker weight is divided by the factor $\det(R)$, which is straightforward to compute. If reorthogonalization is performed after local energy evaluation and weight update, this factor is irrelevant and can be disregarded.

Cholesky Decomposition

Another robust reorthogonalization method is achieved using the Cholesky decomposition.[102] Given a walker determinant Ψ, we construct the positive-definite overlap matrix and decompose it as

$$S = \Psi^\dagger \Psi = L L^\dagger \tag{3.48}$$

using the Cholesky decomposition. Here, L is a lower-triangular matrix of dimensions $N_e \times N_e$. The new set of orbitals

$$\Psi' = \Psi (L^\dagger)^{-1} \tag{3.49}$$

is orthonormal, as easily verified:

$$(\Psi')^\dagger \Psi' = \left(\Psi (L^\dagger)^{-1}\right)^\dagger \Psi (L^\dagger)^{-1} = L^{-1} \Psi^\dagger \Psi (L^\dagger)^{-1} = \left(L^{-1} L\right)\left(L^{-1} L\right)^\dagger = 1. \tag{3.50}$$

Regardless of the reorthogonalization method, the number of operations needed for the reorthogonalization of a single walker is approximately $N N_e^2$, which is typically much cheaper than the AFQMC propagation or local energy evaluation (see Chapter 4). Therefore, it is expedient to reorthogonalize walkers as often as possible.

[3] $\langle \Psi_T | \Psi' \rangle = \det(\Psi_T^\dagger \Psi') = \det(\Psi_T^\dagger \Psi T) = \det(\Psi_T^\dagger \Psi) \det(T) = \langle \Psi_T | \Psi \rangle \det(T)$

Chapter 4

Benchmark Phaseless Auxiliary-Field Quantum Monte Carlo Method for Small Molecules

This chapter is based on:

Benchmark Phaseless Auxiliary-Field Quantum Monte Carlo Method for Small Molecules
Zoran Sukurma, Martin Schlipf, Moritz Humer, Amir Taheridehkordi, Georg Kresse

published in: Journal of Chemical Theory and Computation **19** (15), 4921-4934 (2023)
doi: https://doi.org/10.1021/acs.jctc.3c00322
arXiv: https://arxiv.org/abs/2303.04256

The Section 4.2, where the general AFQMC formalism is described, is modified and partially moved to the Chapter 3.

Author Contribution: conceptualization of the project (together with coauthors), software development, numerical calculations, data acquisition, data analysis, drafting of the initial manuscript, manuscript editing and proofreading (together with coauthors).

We report a scalable Fortran implementation of the phaseless auxiliary-field quantum Monte Carlo (ph-AFQMC) and demonstrate its excellent performance and beneficial scaling with respect to system size. Furthermore, we investigate modifications of the phaseless approximation that can help to reduce the overcorrelation problems common to the ph-AFQMC. We apply the method to the 26 molecules in the HEAT set, the benzene molecule, and water clusters. We observe a mean absolute deviation of the total energy of 1.15 kcal/mol for the molecules in the HEAT set; close to chemical accuracy. For the benzene molecule, the modified algorithm despite using a single-Slater-determinant trial wavefunction yields the same accuracy as the original phaseless scheme with 400 Slater determinants. Despite these improvements, we find systematic errors for the CN, CO_2, and O_2 molecules that need to be addressed with more accurate trial wavefunctions. For water clusters, we find that the ph-AFQMC yields excellent binding energies that differ from CCSD(T) by typically less than 0.5 kcal/mol.

4.1 Introduction

Density functional theory (DFT) approximately solves the many-body Schrödinger equation by mapping it to a single-particle problem and has become routine in quantum chemistry and condensed matter physics.[103–105] Despite its simplicity and the fact that it can describe systems with hundreds of atoms, DFT is not always accurate enough to serve as a general-purpose solution. The stretched H_2 molecule is a well-known example of the limitations of DFT, as its results are qualitatively wrong.[106] The key problem is the treatment of the electron-electron correlation effects via approximate exchange-correlation (xc) energy functionals.[107] Perdew established the analogy of *climbing Jacob's ladder* for the effort of developing more advanced xc functionals to reach chemical accuracy.[108] Higher rungs offer higher accuracy at the price of higher computational costs and lower transferability. Novel xc potentials based on machine learning[109,110] attempt to address the accuracy issue but still struggle with lower transferability. It remains to be seen whether machine learning functionals will replace traditional ones in the coming years. Machine-learned xc potentials as well as machine-learned force fields[111,112] require highly accurate reference data. In addition, more accurate methods are also important to calibrate new methods or to access strongly correlated materials where DFT generally performs poorly.

For this reason, a whole spectrum of correlation-consistent methods has been developed over the last 50 years.[58,59] Full configuration interaction (FCI) provides an exact solution within a given basis set[77] but suffers from exponential scaling. Therefore, it is only usable for modest system sizes (up to 10^{10} Slater determinants). A clever partitioning of the Fock space led to a class of methods called selected CI[113–115] and its stochastic counterpart full configuration interaction quantum Monte Carlo (FCIQMC).[87,88,116] These methods enabled the treatment of the Fock space with up to 10^{30} Slater determinants while maintaining the accuracy of the traditional FCI. A variant of the selected CI methods, semistochastic heat-bath configuration interaction (SHCI)[114] was able to achieve nearly exact atomization energies for 55 molecules in the G2 set with a mean absolute deviation of 0.5kcal/mol compared to the experimental values.[117] However, these methods still scale weakly exponentially making them difficult to apply to more realistic systems.

Besides CI methods, the most prominent methods are based on the coupled-cluster expansion. The most popular among them, the "gold-standard" coupled-cluster singles, doubles, and perturbative triples (CCSD(T)),[118,119] is extensively used to treat molecules and is known to give excellent results for systems with small static correlation effects. High-accuracy benchmark data for small molecules are usually calculated using the CC expansion. For instance, a series of papers focused on high-accuracy extrapolated ab-initio thermochemistry (HEAT) include electron-electron correlation up to full quintuples in the coupled cluster expansion.[45,120,121] For the molecules in the HEAT set, these results are considered to be as good as the FCI results. More importantly, the HEAT studies also show that CCSD(T) alone is not accurate enough to achieve chemical accuracy ($<$ 1kcal/mol) but approaches it in many relevant cases. Furthermore, CCSD(T) scales adversely with the 7th power of the system size and performs poorly in the presence of strong static correlation effects, e.g. bond dissociation. These drawbacks emphasize the need for alternative methods.

The density-matrix renormalization group (DMRG) is a variational method widely used to treat systems with strong correlation effects.[122–124] It uses matrix-product states

to encode the locality in one of the spatial dimensions and to reduce the exponential scaling of the CI expansion. For low-dimensional quantum systems (quantum dots, molecules extended in one dimension), DMRG is the method of choice due to its efficiency and accuracy. Although DMRG is applicable to arbitrary systems, its limitation of about 30 active orbitals prevents it from being a general-purpose tool for more generic and compact molecules or solids.

Quantum Monte Carlo methods, such as variational Monte Carlo[125] (VMC) and diffusion Monte Carlo[80,89,91] (DMC), exhibit low polynomial scaling with system size and are nowadays routinely applied to systems with hundreds of electrons. However, Nemec and co-workers[126] showed that achieving chemical accuracy is difficult with DMC. They reported a mean absolute deviation of atomization energies of 3.2kcal/mol for 55 molecules in the G2 set.[127] Additionally, VMC and DMC require accurate models for multi-electron wavefunctions including linear combinations of Slater determinants, Jastrow factors, backflow wavefunctions, and many others. Petruzielo *et. al.*[128] performed DMC calculations on a G2 set using a small complete active space Slater-Jastrow trial wavefunction and obtained a mean absolute deviation of 1.2kcal/mol compared to experimental atomization energies. Finally, recent work that combines Deep Learning and VMC has emerged as a promising way to tackle the quantum many-body problem.[129,130]

In this work, we use the auxiliary-field quantum Monte Carlo (AFQMC) method. AFQMC is a well-established projector Monte Carlo method successfully used in various applications.[17,27–31,37,38,131] The original AFQMC was formulated as a path-integral method using the Metropolis algorithm.[3–5,132] It behaved well for systems without severe fermionic sign problem. Since almost all general fermionic systems suffer from the sign problem, the reformulation into an open-ended random walk led to the constrained path (cp)-AFQMC, which was remarkably successful for model Hamiltonians.[6,7] In order to handle general many-body Hamiltonians, the phaseless (ph)-AFQMC was proposed by Zhang and co-workers.[8] The ph-AFQMC was successfully applied to isolated molecules using Gaussian-type orbitals (GTOs) and to solids using a plane-wave basis (PWs).[10] With the increasing popularity of the method, a wide range of ph-AFQMC applications emerged in recent years.[17,27–31,37,38,131] One reason for its popularity is that the ph-AFQMC scales quartic with the system size. This scaling stems from the local energy evaluation and can be further reduced using tensor contraction,[23,26] density-fitting techniques[24,25] or plane-wave basis.[10] In contrast to DMC, AFQMC yields energies fully consistent with other traditional quantum chemistry approaches, allowing correlation energies to be directly compared.

Controlling the fermionic phase problem is crucial for the accuracy of the AFQMC method. In the ph-AFQMC, the *phaseless approximation* imposes a constraint on the walker weights,[8,99,133] analogous to the fixed-node approximation in DMC.[80] The phaseless approximation can introduce somewhat uncontrolled errors that often lead to overestimated correlation energies. In the ph-AFQMC, improving the trial wavefunctions systematically reduces the phaseless approximation error. As the trial wavefunction approaches the exact ground-state wavefunction, the ph-AFQMC energy approaches the exact ground-state energy and the phaseless error disappears. Usually, the trial wavefunction consists of the single Slater determinant formed from Hartree-Fock (HF) or Kohn-Sham (KS) orbitals. They are particularly popular because they are easily accessible from all quantum chemistry / solid-state physics codes and avoid additional computational costs introduced by more complex trial wavefunctions.

Recent research focused on multi-determinant trial wavefunctions[49,50,134–136]. For example, Mahajan *et. al.* used 10^4 Slater determinants while increasing the total cost of the ph-AFQMC computation by only a factor of 3 in comparison to the single Slater determinant case.

In this study, we adopt a simpler approach. We will carefully scrutinize whether modifications to the weight update reduce the need to go beyond single-determinant trial wavefunctions. With these modifications, the ph-AFQMC can provide close to chemical accuracy for the HEAT set. Bomble *et. al.*[120] provided highly accurate CCSDTQP molecular energies at the double-zeta basis set (cc-pVDZ). In this work, we benchmark the accuracy of the ph-AFQMC energies against this reference data set of small molecules. Borda *et. al.* recently performed a similar study on the G1 test set.[35] Their study focused on non-orthogonal multi Slater determinant expansion as a tool to generate high-quality compact trial wavefunctions for AFQMC. They found that using 1, 5, and 20 non-orthogonal Slater determinants as the trial wavefunction for ph-AFQMC resulted in mean absolute deviations of 1.42 kcal/mol, 0.41 kcal/mol, and 0.19 kcal/mol, respectively.

The rest of the paper is structured as follows: In Sec. 4.2, the ph-AFQMC method is briefly reviewed along with the proposed modifications, followed by details on the implementation in Sec. 4.3. In Sec. 4.4, we present and discuss different applications of ph-AFQMC. Finally, Sec. 4.5 concludes our findings and possibilities for future developments.

4.2 AFQMC Formalism

This section is partially moved to the Chapter 3.

4.2.1 Phaseless Approximation

The fp-AFQMC is formally exact but suffers from the fermionic phase problem. The problem is observed in the expression for the energy evaluation (Eq. (3.32)). After the equilibration time, during which excited states contained in $|\Psi_\mathrm{I}\rangle$ decay exponentially, walkers will populate the entire complex plane uniformly. Therefore, the denominator in Eq. (3.32) vanishes and the whole expression becomes ill-defined. To circumvent the fermionic phase problem, the phaseless approximation is introduced.

Since the effective Hamiltonian given in Eq. (3.22) is complex-valued, the orbitals become complex-valued as well. In DMC, $|\Phi\rangle$ and $-|\Phi\rangle$ are both valid solutions of the Schrödinger equation. Similarly in AFQMC, if $|\Phi\rangle$ is the valid solution, then $e^{i\theta}|\Phi\rangle$ is a valid solution for any $\theta \in [0, 2\pi)$. To prevent the exponential growth of the noise in AFQMC simulation, Zhang *et. al.*[8] introduced a phaseless approximation

$$W_{k+1,w} = W_{k,w} \left| \frac{\langle \Psi_\mathrm{T} | \Psi_{k+1,w} \rangle}{\langle \Psi_\mathrm{T} | \Psi_{k,w} \rangle} R(\mathbf{x}_{kw}, \mathbf{f}_{kw}) \right| \max\left(0, \cos(\Delta\theta)\right), \tag{4.1}$$

$$\theta_{kw} = 0, \tag{4.2}$$

where the importance sampling factor R and the phase change $\Delta\theta$ are defined as

$$R(\mathbf{x},\mathbf{f}) = e^{-\mathbf{x}\mathbf{f}} e^{\mathbf{f}^2/2} = e^{-\sum_g x_g f_g}\ e^{\sum_g f_g^2/2} \tag{4.3}$$

$$\Delta\theta = \mathfrak{Im}\ \ln \frac{\langle \Psi_\mathrm{T}|\Psi_{k+1,w}\rangle}{\langle \Psi_\mathrm{T}|\Psi_{kw}\rangle} \approx \mathfrak{Im} \sum_g x_g f_g. \tag{4.4}$$

The update equation (4.1) can be also rewritten as

$$W_{k+1,w} = W_{kw} \max\left(0,\ \mathfrak{Re}\frac{\langle \Psi_\mathrm{T}|\Psi_{k+1,w}\rangle}{\langle \Psi_\mathrm{T}|\Psi_{kw}\rangle}\right) |R(\mathbf{x}_{kw},\mathbf{f}_{kw})|. \tag{4.5}$$

Zhang *et. al.*[8,99] state that different approximations yield the same expectation values and slightly different standard deviations.

In this work, we investigate this statement more quantitatively. To this end, we modify the expression for the total energy evaluation (Eq. (3.32))

$$E_0 = \frac{\sum_{kw} W_{kw} \cos(\theta_{kw}) E_\mathrm{loc}(\Psi_{kw})}{\sum_{kw} W_{kw} \cos(\theta_{kw})} \tag{4.6}$$

and the update procedure for the walker weights

$$W_{k+1,w} e^{i\theta_{k+1,w}} = W_{kw} e^{i\theta_{kw}} \frac{\langle \Psi_\mathrm{T}|\Psi_{k+1,w}\rangle}{\langle \Psi_\mathrm{T}|\Psi_{kw}\rangle} \mathfrak{Re} R(\mathbf{x}_{kw},\mathbf{f}_{kw})\ . \tag{4.7}$$

We refer to this new approach as ph*-AFQMC throughout this paper. In contrast to the original approach, there are two key differences: First, we retain the complex nature of the walker weights and use the real part for the population control and evaluation of physical observables, such as the energy. Walkers are killed explicitly if $|\theta_{kw}| \geq \frac{\pi}{2}$. Secondly, we include the real part of the importance weight instead of the absolute value. We suggest that only the real part is meaningful and using the absolute value increases the weights with the imaginary part. This may contribute to the systematic over-correlation of ph-AFQMC. We will show in Sec. 4.4 that ph*-AFQMC systematically yields correlation energies smaller in absolute value.

4.3 Implementation Details

In this section, we present our implementation of AFQMC in QMCFort.[1] QMCFort is written in Fortran and utilizes (threaded) BLAS/LAPACK for fast linear algebra and MPI and OpenMP for parallelization. In addition to AFQMC, QMCFort offers implementations of restricted, restricted open-shell, and unrestricted Hartree-Fock (RHF, ROHF and UHF) and MP2. The electron repulsion integrals (ERIs) are calculated using the McMuchie-Davidson scheme[59] and decomposed into Cholesky vectors. Therefore, QMCFort can act as a standalone tool to setup and run AFQMC simulations. However, only the AFQMC part is highly optimized for large-scale calculations. For this reason, we also interface QMCFort with PySCF[137] for isolated systems and with VASP[104] for extended systems. The implementation of the computationally intensive parts of the AFQMC procedure and the interface between QMCFort and VASP are detailed in the remainder of this section.

[1] QMCFort is available from the authors upon a reasonable request.

4.3.1 Effective Hamiltonian

At each time step and for each walker, we build the effective Hamiltonian according to Eq. (3.22). The computationally demanding part is the convolution of the shifted random fields with Cholesky vectors $\sum_g (x_g - f_g) \cdot L_{g,pq}$. Treating the orbital indices p and q as a combined index, we map this contraction to matrix-matrix multiplication with a cubic scaling ($\sim N^2 N_g N_w$) in system size. Typically, we treat in the range of 10 to 100 walkers per MPI rank and compute this contraction for all of them simultaneously. Although the exchange energy evaluation (Sec.4.3.4) scales worse, the creation of the effective Hamiltonian is often the most expensive operation in AFQMC because it is required at each time step.

4.3.2 AFQMC Propagation

The effective Hamiltonian propagates the orbitals according to Eq. (3.38). The matrix exponentials in the Trotter-Suzuki propagator[138,139] are approximated by the sixth-order Taylor expansion. This requires several applications of the effective Hamiltonian to the orbitals, i.e. matrix-matrix multiplications of the form

$$\Psi_{pi,w} \to \bar{\Psi}_{pi,w} = \sum_q \mathcal{H}_{pq,w} \Psi_{qi,w} \; . \tag{4.8}$$

These scale as $N^2 N_e$.

4.3.3 Force Bias

The force bias evaluation (see Eq. (3.29)) is equivalent to the evaluation of the Hartree potential and energy. It scales cubically with respect to the system size, i.e. $N N_g N_e N_w$. Similar to the effective Hamiltonian (Sec. 4.3.1), the force bias is computed for all walkers simultaneously. To make it more transparent, we will first define the contracted Cholesky vectors

$$\mathcal{L}_{g,pi} = \sum_q L_{g,pq} \Psi_{\mathrm{T},qi}, \tag{4.9}$$

and the force bias is then

$$f_{g,w} = \sum_{pi} \mathcal{L}_{g,pi} \Psi_{pi,w} \; . \tag{4.10}$$

Here, we can treat $\{p,i\}$ as a single index and evaluate the contraction with a matrix-matrix multiplication. We use the force bias to compute the Hartree energy for the walker Ψ_w

$$E_{\mathrm{H}}(\Psi_w) = \frac{1}{2} \sum_g f_{g,w} f_{g,w}. \tag{4.11}$$

4.3.4 Exchange Energy

Of all individual contributions to AFQMC, the computation of the exchange energy incurs the largest computational cost. Although the naive implementation of Eq. (3.34) scales as $N^3 N_g N_w$, we simplify it by computing intermediate arrays $\alpha^w_{g,ij}$

$$\alpha^w_{g,ij} = \sum_p \mathcal{L}_{g,pi} \Psi^w_{pj} \; . \tag{4.12}$$

Table 4.1: Number of operations per walker and time step and asymptotic scaling of the computationally intensive parts of the AFQMC procedure. N represents the number of basis functions, N_g is the number of Cholesky vectors, and N_e is the number of occupied states in the system.

Task	# of operations	asymptotic scaling
effective Hamiltonian	$N^2 N_g$	$\mathcal{O}(N^3)$
AFQMC propagation	$N^2 N_e$	$\mathcal{O}(N^3)$
force bias	$N N_g N_e$	$\mathcal{O}(N^3)$
exchange energy	$N N_g N_e^2 + N_g N_e^2$	$\mathcal{O}(N^4)$

The exchange energy of the walker Ψ_w is then given by

$$E_{\mathrm{x}}(\Psi_w) = -\frac{1}{2}\sum_g \sum_{ij} \alpha^w_{g,ij}\alpha^w_{g,ji} \,. \tag{4.13}$$

The quartic-scaling ($N N_g N_e^2 N_w$) construction of the intermediate arrays $\alpha^w_{g,ij}$ is also mapped to a matrix-matrix multiplication. Multiple walkers are treated simultaneously in a block of approximately 5-10 walkers for optimal performance. One can evaluate the exchange energy only say every 10th time step. This has no significant impact on the statistics because one needs to sample independent local energies so the alternative is block averaging. Computing the exchange energy from the α tensors scales as $N_g N_e^2$ but the computational effort is negligible in comparison to other tasks discussed in this section.

4.3.5 Other tasks

Besides the operations mentioned above, there are a few additional parts of the AFQMC procedure that should be mentioned. Since the AFQMC propagator is non-unitary, we periodically reorthogonalize the walkers by a QR decomposition of the walker matrices Ψ_w. The walker population is controlled to avoid too small or too large weights. We opted for the comb method[140], because it keeps the total number of walkers constant.

4.3.6 Performance

In Table 4.1, we summarize the number of operations corresponding to the computationally demanding tasks. Assuming that the number of walkers is independent of the system size, we list the resulting asymptotic large system-size scaling for these tasks. We gauge the asymptotic behavior for water clusters of various sizes containing up to 5 water molecules. The calculations were performed on a dual-socket Intel Skylake Platinum 8174 with 24 cores each and a nominal base frequency of 3.1 GHz. We average the timings over 200 AFQMC steps, with each step processing 4 800 walkers on 48 MPI processes.

Fig. 4.1 shows the elapsed times per AFQMC step of the computationally demanding tasks. To estimate the effective scaling exponent for each task, we fit the power function $f(x) = Cx^{\beta}$ through the data points. As predicted, the construction of the

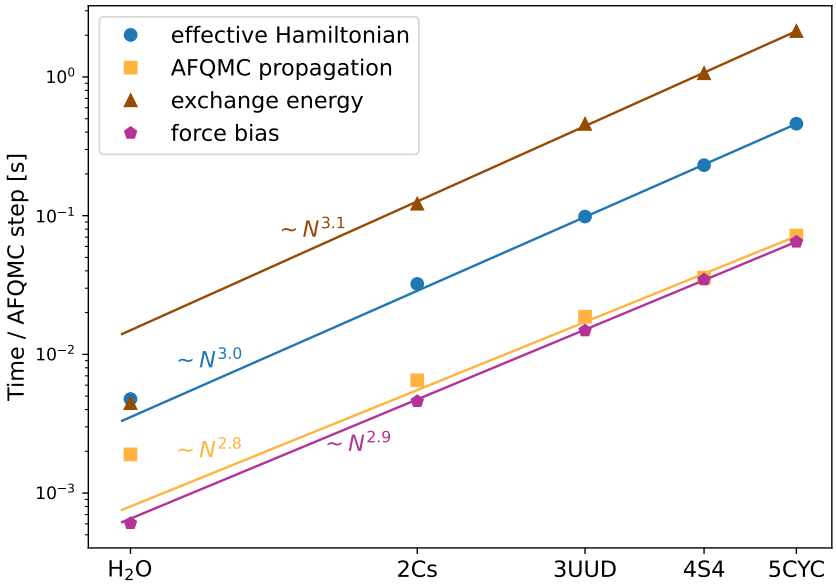

Figure 4.1: Elapsed time per AFQMC step of the computationally intensive operations measured on water clusters of different sizes. AFQMC calculations were performed on a dual-socket Intel Skylake Platinum 8174 with 4 800 walkers, and 48 MPI processes. Timings are averaged over 200 AFQMC steps.

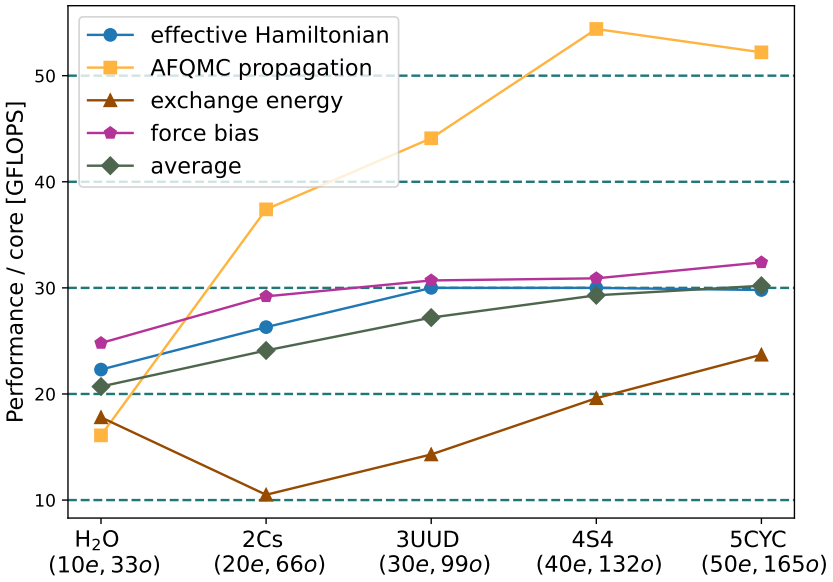

Figure 4.2: Performance per CPU core of the computationally intensive operations in the AFQMC procedure measured on water clusters of different sizes. Tuples on the x-axis denote the number of electrons and orbitals. Executing the AFQMC code on one CPU node (dual-socket Intel Skylake Platinum 8174) delivers 1–1.5 TFLOPS (30 GFLOPS per core, green line) on average.

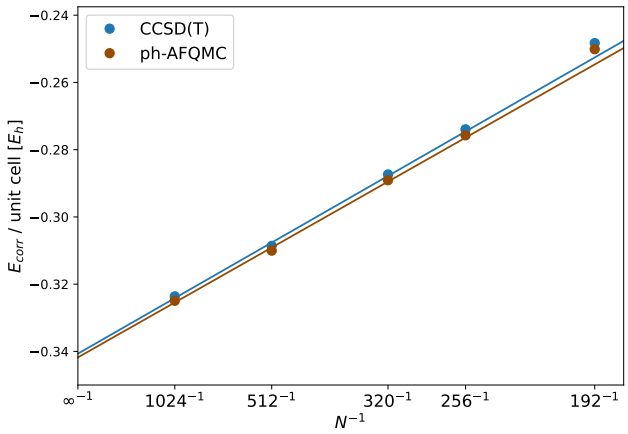

Figure 4.3: Convergence behavior of the CCSD(T) and ph-AFQMC correlation energies as a function of the number of canonical orbitals for diamond. Linear extrapolation to the complete basis set is performed using the first three points (1024^{-1}, 512^{-1}, and 320^{-1}). The calculations were performed using a 2x2x2 diamond supercell with an energy cutoff of 700eV.

effective Hamiltonian, AFQMC propagation, and force bias calculation scale cubically. The measured exponent $\beta = 3.1$ for the exchange energy does not exactly match the expected exponent $\beta = 4$. With increasing system size, we observe an increasing per-core performance of the exchange evaluation (Fig. 4.2). This increase effectively reduces the scaling exponent. Still, the exchange evaluation is the least performant of the relevant computational tasks. As depicted in Fig. 4.2, most other tasks run efficiently with the performance of 20–35 GFLOPS/core. A notable exception is the AFQMC propagation that reaches a performance above 50 GFLOPS/core for large systems, very close to peak performance.

4.3.7 Interface with VASP

VASP provides a set of one-electron mean-field orbitals $\{\phi_p(\mathbf{r})\}$. From these, we compute the single-particle Hamiltonian matrix elements h_{pq} and Cholesky vectors $L_{g,pq}$ (see Appendix for more details). We export the matrix elements and Cholesky vectors to a file and read them with QMCFort. Then, the AFQMC calculation for extended systems is equivalent to calculations on isolated molecules using the Gaussian basis set.

As an example, we compute the 2x2x2 supercell of diamond. The convergence of the AFQMC and CCSD(T) correlation energies with respect to the number of canonical orbitals is studied. CCSD(T) energies are computed using Cc4s code.[67] A lattice constant of $a = 3.567$ Å is used with an energy cutoff of $E_{\text{cut}} = 700$ eV. In addition, we use an energy cutoff $E^{\chi}_{\text{cut}} = 500$ eV for the truncation of the Coulomb kernel. VASP relies on PAW potentials[105,141] and the potential referred to as C_GW with valence $2s2p$ was used. The core radius of this potential is $r_{\text{core}} = 1.5$ a.u.; the local potential is equivalent to the d-pseudopotential and 4 projectors are used (two s-projectors with $r_{\text{cut}} = 1.2$ a.u., and two p-projectors with $r_{\text{cut}} = 1.5$ a.u.).

Figure 4.3 shows the convergence of the correlation energy as a function of the number of canonical orbitals for ph-AFQMC and CCSD(T). The number of orbitals

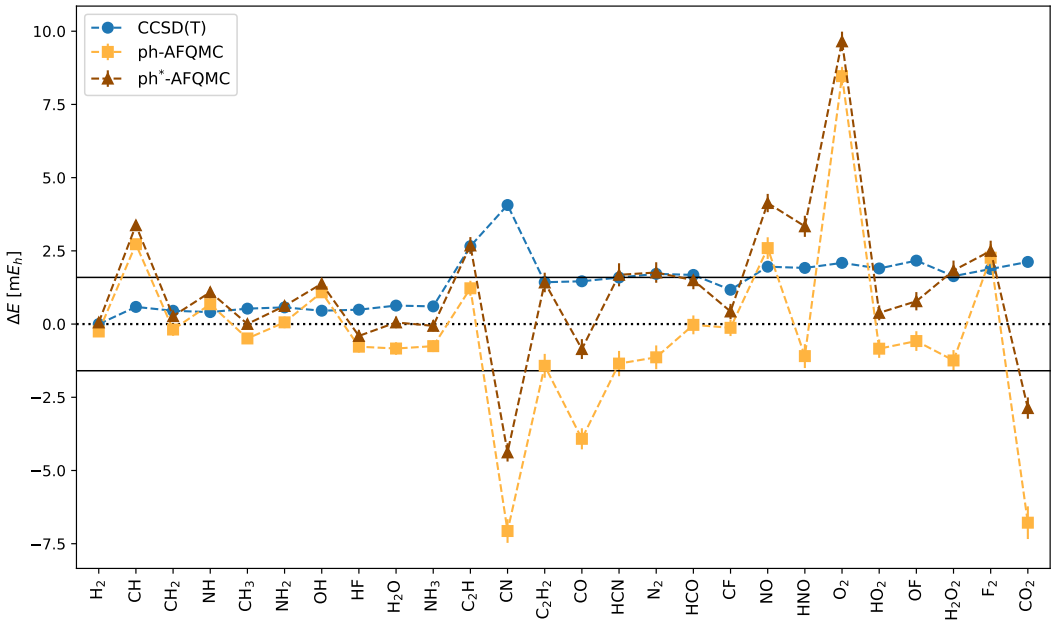

Figure 4.4: CCSD(T), ph-AFQMC and ph*-AFQMC total-energy differences ΔE relative to the reference CCSDTQP energies for the HEAT set. Calculations use the cc-pVDZ basis set and a frozen-core approximation including only the last occupied shell. Trial wavefunctions are single RHF/UHF Slater determinants. The solid black line represents the chemical accuracy range ($\Delta E < 1\,\mathrm{kcal/mol}$)

is varied from the small basis set with 64 electrons in 192 orbitals (64e, 192o) to a relatively large basis of 64 electrons in 1024 orbitals (64e, 1024o). A $1/N$ behavior is fitted through the data points. The ph-AFQMC and CCSD(T) lines are almost indistinguishable suggesting that the methods yield consistent energies for periodic systems. Further details on AFQMC calculations for extended systems will be reported in a forthcoming publication.[42]

To compare the computational cost of the CCSD(T) and ph-AFQMC, we conducted calculations using 256 and 1024 bands. For the 256-band calculation, the CCSD(T) calculation took 20 minutes on a single node (2x AMD Epyc (Milan)), while the ph-AFQMC calculation took 11 hours. However, for the 1024-band calculation, CCSD(T) required 24 hours on 4 nodes (2x AMD Epyc (Milan)), while ph-AFQMC calculation took 48 hours to complete. The timings we obtained for the CCSD(T) and ph-AFQMC calculations demonstrate the favorable scaling of the AFQMC method, which becomes increasingly advantageous as the number of orbitals and the complexity of the system increase.

4.4 Results and Discussion

In the following four subsections, we report (i) the total molecular energies for 26 molecules from the HEAT set, (ii) the AFQMC energy of the benzene molecule using the cc-pVDZ basis set, and (iii) the AFQMC binding energies of the water clusters.

Table 4.2: Total molecular energies (in Hartree units) for the HEAT set[45] molecules at different levels of theory: ph-AFQMC[8], ph*-AFQMC, CCSD(T), CCSDTQP[120] and HCI[113, 114]. All energies are calculated using the cc-pVDZ basis set. The last three rows of the table depict the root-mean-square deviation (RMSD), mean signed deviation (MSD), and mean absolute deviation (MAD).

Molecule	ph-AFQMC	ph*-AFQMC	CCSD(T)	CCSDTQP	HCI
H_2	-1.16363(2)	-1.16338(3)	-1.163426	-1.163426	-1.163426
CH	-38.37764(6)	-38.37705(7)	-38.379655	-38.380241	
CH_2	-39.04181(5)	-39.04150(6)	-39.041196	-39.04165	
NH	-55.09087(5)	-55.09077(7)	-55.097448	-55.0917	
CH_3	-39.71651(6)	-39.71592(7)	-39.715543	-39.71607	
NH_2	-55.73265(6)	-55.73222(8)	-55.732506	-55.733076	
OH	-75.55854(6)	-75.55837(8)	-75.559233	-75.559689	
HF	-100.22933(7)	-100.2290(1)	-100.228131	-100.228622	
H_2O	-76.24249(8)	-76.24167(9)	-76.241018	-76.241649	-76.241637
NH_3	-56.40334(7)	-56.4024(1)	-56.401913	-56.402517	
C_2H	-76.3999(2)	-76.3986(2)	-76.398558	-76.401217	
CN	-92.4997(2)	-92.4973(2)	-92.488695	-92.49276	-92.492788
C_2H_2	-77.1118(2)	-77.1092(2)	-77.109249	-77.110678	
CO	-113.0594(2)	-113.0567(2)	-113.054431	-113.055892	
HCN	-93.1912(2)	-93.1881(2)	-93.188321	-93.18991	
N_2	-109.2781(2)	-109.2750(2)	-109.275298	-109.277012	-109.277005
HCO	-113.5778(2)	-113.5757(2)	-113.575706	-113.577384	
CF	-137.4764(1)	-137.4754(2)	-137.474848	-137.476019	
NO	-129.5970(2)	-129.5945(2)	-129.597778	-129.599737	
HNO	-130.1736(2)	-130.1697(2)	-130.170989	-130.172906	
O_2	-149.9792(2)	-149.9787(2)	-149.985684	-149.987773	
HO_2	-150.5606(2)	-150.5603(2)	-150.558481	-150.56038	
OF	-174.5004(2)	-174.4998(2)	-174.497924	-174.50009	
H_2O_2	-151.1963(2)	-151.1940(2)	-151.19363	-151.195266	
F_2	-199.0968(2)	-199.0965(2)	-199.097448	-199.099328	
CO_2	-188.1561(2)	-188.1525(2)	-188.147429		-188.149551
RMSD (in mE_h)	2.89	2.73	1.65		
MSD (in mE_h)	-0.38	1.17	1.39		
MAD (in mE_h)	1.85	1.84	1.39		

4.4.1 Heat Molecules

We calculated total energies for 26 molecules from the HEAT set using the frozen-core approximation and geometries from Ref.[120] (HEAT). All calculations employed the double-zeta basis set (cc-pVDZ). We used the QMCFort code to calculate Cholesky vectors, the reference Hartree-Fock (RHF/UHF) wavefunctions, and all AFQMC energies. We used the PySCF package[137] to calculate the CCSD(T) energies. The Dice code[113,114] was used to calculate the heat-bath CI energies. To eliminate possible sources of systematic errors in the AFQMC, we (i) truncated Cholesky vectors at a conservative threshold of 10^{-8} to ensure a reasonably accurate representation of the molecular ERIs, (ii) chose a relatively small time step of $0.002\,E_\mathrm{h}^{-1}$ to exclude significant time-step errors, and (iii) equilibrated the system for 40 000 time steps. To ensure good statistics, we propagated 6 000 walkers until the standard error of the mean of the predicted molecular energies dropped below $0.2\,\mathrm{m}E_\mathrm{h}$.

Table 4.2 compares the ph-AFQMC and ph*-AFQMC molecular energies to the "gold-standard" CCSD(T) and the more accurate coupled-cluster expansion including variational triple, quadruple and pentuple excitations (CCSDTQP). We use the latter as reference values since they are practically converged against the FCI limit. The CCSDTQP value for the CO_2 molecule is missing in Ref.[120], so we use the result of the heat-bath configuration interaction (HCI).[113] cTo verify the accuracy of the HCI method, we selected a few other molecules (H_2, H_2O, CN, N_2) and found a maximal difference to the CCSDTQP values of $0.01\,\mathrm{m}E_\mathrm{h}$, well below the statistical AFQMC errors. Comparing to these reference values, we find a similar precision for the ph-AFQMC and ph*-AFQMC method with a root-mean-square deviation (RMSD) of $2.89\,\mathrm{m}E_\mathrm{h}$ and $2.73\,\mathrm{m}E_\mathrm{h}$, respectively. For context, the CCSD(T) exhibits a RMSD of $1.65\,\mathrm{m}E_\mathrm{h}$ for these molecules. The mean absolute deviations (MAD) of $1.39\,\mathrm{m}E_\mathrm{h}$ (CCSD(T)), $1.85\,\mathrm{m}E_\mathrm{h}$ (ph-AFQMC) and $1.84\,\mathrm{m}E_\mathrm{h}$ (ph*-AFQMC) show a smaller difference between the methods indicating that some outliers taint the overall performance of AFQMC. The mean signed deviation (MSD) of $1.39\,\mathrm{m}E_\mathrm{h}$ (CCSD(T)) and $1.17\,\mathrm{m}E_\mathrm{h}$ (ph*-AFQMC) indicate under-correlation in contrast to ph-AFQMC with an average over-correlation of $-0.38\,\mathrm{m}E_\mathrm{h}$. The modified approach (ph*-AFMQC) is also closer to CCSD(T) with an RMSD of $2.66\,\mathrm{m}E_\mathrm{h}$ compared to ph-AFQMC with an RMSD of $3.67\,\mathrm{m}E_\mathrm{h}$.

Next, we present a more detailed analysis based on the graphical representation of the results in Fig. 6.7. Let us focus on the more-widely-used CCSD(T) method first. Fig. 6.7 illustrates that CCSD(T) systematically under-correlates compared to the reference values. The most frequent deviation lies around $1\,\mathrm{kcal/mol}$ (i.e. $1.59\,\mathrm{m}E_\mathrm{h}$). The worst case is the CN molecule with a deviation of $4.1\,\mathrm{m}E_\mathrm{h}$. The reason for the larger deviation is probably the large spin contamination in the UHF wavefunction.[120]

The ph-AFQMC and ph*-AFQMC results show similar trends. The O_2 molecule is the worst case for AFQMC with an undercorrelation of $8.6\,\mathrm{m}E_\mathrm{h}$. Solving this problem requires a multi-determinant trial wavefunction, for example from a complete active space self-consistent field (CASSCF) calculation in the open-shell subspace. A similar problem in open-shell atoms is solved by using multi-determinant CASSCF trial wavefunctions or by using symmetry restoration techniques.[133] Excluding O_2 from the statistics reduces the RMSD to 2.41 and $2.11\,\mathrm{m}E_\mathrm{h}$ for the ph-AFQMC and ph*-AFQMC method, respectively.

In contrast to the O_2 molecule, the ph-AFQMC values for CN, CO, and CO_2 molecules show considerable over-correlation (up to $7\,\mathrm{m}E_\mathrm{h}$ for the CN molecule).

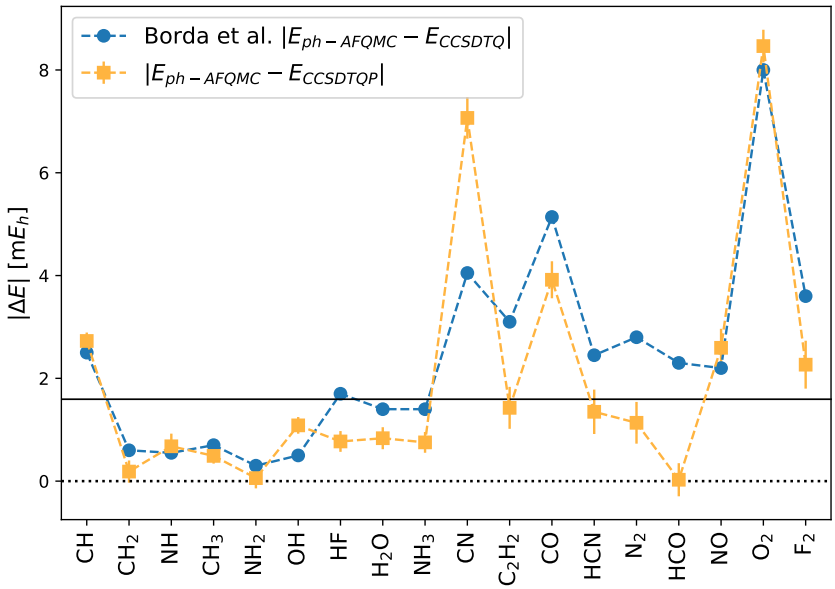

Figure 4.5: Absolute total energy difference $|\Delta E|$ between ph-AFMQC (QMCPACK) and CCSDTQ (see Ref.[35]) as well as ph-AFQMC (QMCFort) and CCSDTQP for the overlapping molecules in the G1 and HEAT set.

The origin of these deviations is the fixed-node error. Our modified approach (ph*-AFQMC) systematically increases the energies compared to ph-AFQMC. It is noteworthy that the differences are larger in the cases where the ph-AFQMC shows larger over-correlation. The fixed-node errors are therefore significantly reduced for the CN, CO, and CO_2 molecules but the residual errors are still sizable. Better trial wavefunctions could further reduce the fixed-node errors.

Borda *et. al.*[35] performed similar benchmarks using the G1 test set that partially overlaps with the HEAT set. They also used cc-pVDZ basis sets with the frozen-core approximation and compared AFQMC total energies calculated with the QMCPACK package to the CCSDTQ energies. Although they also employed more accurate trial wavefunctions, this study focuses on comparing our results to theirs using a single Slater determinant. While we used UHF trial wavefunctions, they used ROHF ones for the AFQMC calculations. Fig. 4.5 shows the deviation of ph-AFQMC from the reference energies. Overall, most energies agree within 1 mE_h between the two ph-AFQMC calculations. For the remaining cases, our results appear to be closer to the reference result except for the CN molecule. Possible reasons for these differences include: (i) smaller statistical and systematic errors in the present work, (ii) different molecular geometries, and (iii) different trial wavefunctions. The latter matters particularly for the CN molecule because the large spin contamination in the UHF wavefunction makes the ROHF wavefunction a better choice for the trial wavefunction.

Next, we study the basis-set impact by comparing the total energy differences between ph*-AFQMC and CCSD(T) for the cc-pVDZ basis set and the roughly six-times larger aug-cc-pVQZ one. The latter includes core electrons overcoming the frozen-core approximation of the smaller basis. Fig. 4.6 shows remarkably similar energy differences for both basis sets. Three notable exceptions are F_2, O_2, and OH where the deviation is slightly larger than 1 kcal/mol. This result is important for two

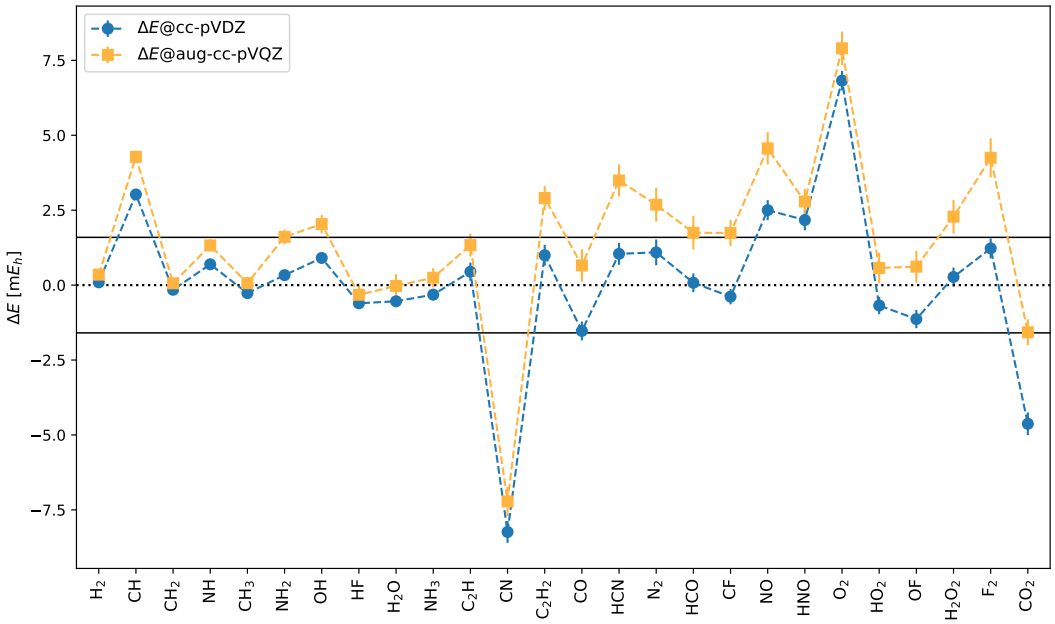

Figure 4.6: Total-energy difference ΔE between ph*-AFQMC and CCSD(T) for the HEAT set. The cc-pVDZ calculations employ the frozen-core approximation; the aug-cc-pVQZ ones include all electrons. Trial wavefunctions are single RHF and UHF Slater determinants for closed- and open- shell molecules, respectively. The solid black line represents chemical accuracy ($\Delta E < 1\,\mathrm{kcal/mol}$).

reasons: First, the comparison between ph*-AFQMC and CCSD(T) is sufficiently accurate using a cc-pVDZ basis set. Hardly any new conclusion could be drawn from the complete basis-set limit. Secondly, the ph*-AFQMC precisely describes core-electron effects at the accuracy of the CCSD(T) method.

4.4.2 Benzene Molecule

The ground state of the benzene molecule with double-zeta basis set (cc-pVDZ) is an interesting system to benchmark state-of-the-art correlation-consistent methods because it is among the largest systems that can be treated directly using FCI diagonalization. The benzene molecule in the cc-pVDZ basis set contains 108 orbitals and 30 electrons (in the frozen-core approximation).

Eriksen *et. al.*[142] performed a blind test on the benzene molecule comparing ten different methods. They include the coupled-cluster expansion methods, different selected CI methods, and quantum Monte Carlo methods. The authors agreed that the full coupled-cluster reduction (FCCR) and many-body FCI expansion (MBE-FCI) essentially yield the exact correlation energy of $-863.0\,\mathrm{m}E_\mathrm{h}$. Lee *et. al.*[37] supplemented the study with ph-AFQMC results using two different trial wavefunctions: RHF wavefunction and CASSCF(6,6) multiconfigurational wavefunction. The ph-AFQMC+RHF overestimates the correlation energy by $3.1\,\mathrm{m}E_\mathrm{h}$, while the ph-AFQMC+CAS(6,6) over-correlates by $1.2\,\mathrm{m}E_\mathrm{h}$. For the sake of completeness, we augmented the study with CCSD(T) results which are under-correlated by $3.5\,\mathrm{m}E_\mathrm{h}$. Our ph-AFQMC+RHF result is equivalent to the ph-AFQMC+RHF result calculated using the QMCPACK code.[143,144] This serves as an additional validation of our AFQMC implementation

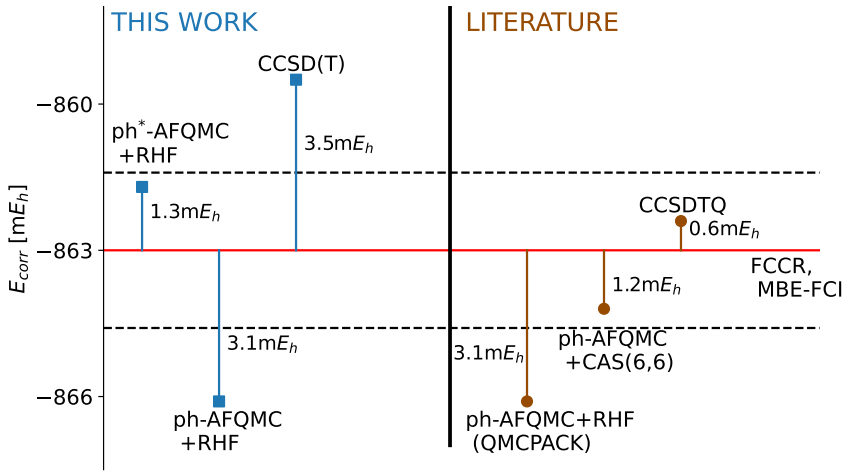

Figure 4.7: Correlation energies for the benzene molecule using the cc-pVDZ basis set and the frozen-core approximation. ph-AFQMC(RHF), ph*-AFQMC(RHF) correlation energies are obtained using QMCFort code, while the CCSD(T) energy is calculated using PySCF code.[137] Other values are taken from the Refs.[37,142]. The red line represents the reference correlation energy of $-863.0\,\mathrm{m}E_\mathrm{h}$, while the dashed black lines represent the range of the chemical accuracy ($1\,\mathrm{kcal/mol}$). All energy values are given in $\mathrm{m}E_\mathrm{h}$.

in QMCFort. Similar to CN, CO, and CO_2, ph*-AFQMC+RHF reduces the absolute value of the correlation energy considerably and leads to an energy under-correlated by $1.3\,\mathrm{m}E_\mathrm{h}$. In this case the quality of the ph*-AFQMC+RHF is seemingly similar to the quality of ph-AFQMC+CAS(6,6). However, better trial wavefunctions promise improved accuracy and, most importantly, more controlled results. All methods and respective correlation energies are visualized in Fig. 6.11.

4.4.3 Water Clusters

Great effort has been put into developing empirical models that faithfully represent the properties of bulk water. It turns out that a good model must also adequately describe the small water clusters present in the Earth's atmosphere. Temeslo *et. al.* collected representative structures for water clusters of various sizes.[145] They investigated which contributions are important to obtain accurate formation energies. Motta *et al.* reported deviations of AFQMC and CCSD(T) larger than the statistical fluctuations.[23] Here, we revisit these clusters to scrutinize the accuracy of AFQMC for water.

We estimate the binding energy of the most stable water cluster with $n \leq 5$ H_2O molecules

$$E_b(n\mathrm{H_2O}) = E(n\mathrm{H_2O}) - nE(\mathrm{H_2O})\ . \tag{4.14}$$

Here, $E(n\mathrm{H_2O})$ is the total energy of the cluster, and $E(\mathrm{H_2O})$ is the ground-state energy of the water molecule. The cluster geometries are taken from Ref.[145]. We relaxed the single water molecule using MP2 at aug-cc-pVDZ basis set and obtain a bond length of 0.96593 Å and a bond angle of 103.866°. We used the heavy-augmented basis set (aug-cc-pVDZ for O atom and cc-pVDZ for H atom) and all-electron wavefunctions to compare our results with Ref.[23]. The PySCF package[137] produced the CCSD(T)

Table 4.3: Binding energies of the four most stable water clusters containing up to 5 H_2O molecules calculated using heavy-augmented cc-pVDZ basis set and all-electron wavefunctions. RHF, MP2, CCSD(T), and different ph-AFQMC values in kcal/mol are reported.

Cluster	RHF	MP2	CCSD(T)	ph-AFQMC	ph*-AFQMC	ph-AFQMC[23]
2Cs	-3.82	-5.22	-5.18	-5.17(05)	-5.06(07)	-5.11(31)
3UUD	-10.52	-15.83	-15.62	-15.67(09)	-15.68(09)	-14.78(64)
4S4	-19.00	-28.36	-27.87	-28.12(10)	-28.11(10)	-26.49(46)
5CYC	-25.30	-37.48	-36.78	-37.14(28)	-37.31(28)	-36.27(59)

Table 4.4: The AFQMC energies of the stretched 3UUD cluster and its fragments, and the binding energies demonstrate that ph-AFQMC and ph*-AFQMC are both size-consistent (all values are given in E_h).

Cluster	ph-AFQMC	ph*-AFQMC
3UUD	-228.82750(12)	-228.82448(12)
1-H_2O	-76.27576(04)	-76.27475(04)
2-H_2O	-76.27580(04)	-76.27477(04)
3-H_2O	-76.27585(04)	-76.27481(04)
E_b	0.00009(14)	0.00015(14)

correlation energies and QMCFort the RHF, MP2, and AFQMC ones. We truncated the Cholesky decomposition of the ERIs with a threshold of $10^{-6}E_h$. We propagated 4 800 walkers for 140 000 steps with a time-step of $0.01\,E_h^{-1}$. The exchange energy was evaluated after every 100 steps. For the largest cluster, we used half as many walkers. This setup keeps the systematic errors in the binding energy within 0.05 kcal/mol.

Table 4.3 lists RHF, MP2, CCSD(T), ph-AFQMC, ph*-AFQMC and AFQMC binding energies from Ref.[23]. While the RHF binding energies differ significantly from the correlation-consistent methods, all other methods agree within chemical accuracy. Our AFQMC values are in better agreement with MP2 and CCSD(T) values than the previous AFQMC values. The large statistical errors in the reference data might partially explain the discrepancy in AFQMC binding energies. However, the systematic under-correlation of the reference AFQMC binding energies indicates the existence of systematic errors, too. One possible source of the systematic errors could be the looser threshold in the Cholesky decomposition of the ERIs ($10^{-4}E_h$) in Ref.[23].

To test ph-AFQMC and ph*-AFQMC for size consistency we dissociated the cluster into individual molecules by shifting the second and third molecule in the 3UUD cluster by 8 Å in x and y direction, respectively. We computed the total energy of the stretched cluster and of the individual water molecules individually. We summarize our findings in Table 4.4. Within statistical fluctuations, all fragments exhibit the same total energy which is equal to a third of the stretched cluster. This demonstrates that ph-AFQMC and ph*-AFQMC are size-consistent.

4.5 Conclusion

The phaseless auxiliary-field quantum Monte Carlo is increasingly popular due to its high accuracy, the low polynomial scaling ($N^3 - N^4$), and its applicability to quantum chemistry and condensed matter physics. Using the DFT or HF solutions as starting point, it can be considered as a natural extension of these methods with similar scaling but higher accuracy.

We have presented a Fortran implementation of the AFQMC, QMCFort, that enables efficient large-scale calculations on CPUs. The code is parallelized using MPI, OpenMP, and parallel BLAS, and runs near peak performance for typical systems (see Fig. 4.2). QMCFort can run AFQMC simulations independently or obtain Cholesky vectors of the two-electron intermediates via interfaces to VASP and PySCF.

Using QMCFort, we compared the accuracy of the ph-AFQMC method to the "gold-standard" CCSD(T) and the more accurate CCSDTQP method. For this purpose, we calculated the ph-AFQMC energies of the 26 molecules in the HEAT set, the benzene molecule, and water clusters. For the HEAT set, the ph-AFQMC yields a mean absolute deviation (MAD) of 1.85 mE_h (1.15 kcal/mol) compared to CCSDTQP values. The poor performance for four molecules (CN, CO, CO_2, O_2) is responsible for a large part of this deviation. Such outliers are clearly troublesome as they are difficult to recognize in the absence of reference calculations. Furthermore, CCSD(T) is certainly more robust for the HEAT set and is highly accurate even if the groundstate wavefunction involves significant double excitations. One possible explanation for the presence of outliers and the failure of the AFQMC is that the method fails to account accurately for strong double excitations. This suggests that the AFQMC with a single determinantal trial wavefunction is only capable to treat weakly correlated materials that lack strong static correlation effects even in the space of double excitations.

For the remaining molecules in the HEAT set, ph-AFQMC performs similarly to or better than the CCSD(T). We modified the phaseless approximation—ph*-AFQMC—to overcome at least partly the over-correlation problems often encountered with ph-AFQMC. For the CN, CO, and CO_2 molecules, where the over-correlation effects are particularly pronounced, the modified approach indeed improves the energies significantly. In the case of the benzene molecule, ph*-AFQMC yields a correlation energy 1.3 mE_h higher than the FCI reference value. This is noticeably better than ph-AFQMC and comparable to the accuracy of ph-AFQMC with a multi-determinant CAS(6,6) trial wavefunction. Finally, the AFQMC binding energies of water clusters agree with the CCSD(T) and MP2 binding energies to within 0.5 kcal/mol. For the four water clusters, our present results are generally closer to CCSD(T) results than previous AFQMC results, substantiating our claim that the AFQMC method with a single Slater determinant is particularly suitable for weakly correlated molecules and materials.

Both the ph*-AFQMC, as well as the ph-AFQMC, are rather ad hoc approaches to deal with the fermionic sign problem and the exponential increase of the noise. We feel that the present work does not conclusively show that the ph* approximation is superior to the ph approximation. However, the present work clearly shows that even minor changes to the phaseless approximation can affect the final results. Although we could not find an approximation that more generally improves the results, we believe that further research in this direction is well warranted.

In summary, the ph-AFQMC is a promising and reliable method with high accuracy

and reasonable computational cost. It provides nearly chemical accuracy for the small molecules studied in this work if the molecules are weakly correlated. We plan to further improve the accuracy of QMCFort through algorithmic improvements and the use of more accurate trial wavefunctions.

Chapter 5

Toward Large-Scale AFQMC Calculations: Large Time Step Auxiliary-Field Quantum Monte Carlo

This chapter is based on:

Toward Large-Scale AFQMC Calculations: Large Time Step Auxiliary-Field Quantum Monte Carlo
Zoran Sukurma, Martin Schlipf, Moritz Humer, Amir Taheridehkordi, Georg Kresse

published in: Journal of Chemical Theory and Computation **20** (10), 4205–4217 (2024)
doi: https://doi.org/10.1021/acs.jctc.4c00304
arXiv: https://arxiv.org/abs/2403.02542

The Section 5.2 is partially moved to the Chapter 3 and Appendix E.

Author Contribution: conceptualization of the project (together with coauthors), analytic derivations, software development, numerical calculations, data acquisition, data analysis, drafting of the initial manuscript, manuscript editing and proofreading (together with coauthors).

We report modifications of the ph-AFQMC algorithm that allow the use of large time steps and reliable time step extrapolation. Our modified algorithm eliminates size-consistency errors present in the standard algorithm when large time steps are employed. We investigate various methods to approximate the exponential of the one-body operator within the AFQMC framework, distinctly demonstrating the superiority of Krylov methods over the conventional Taylor expansion. We assess various propagators within AFQMC and demonstrate that the Split-2 propagator is the optimal method, exhibiting the smallest time-step errors. For the HEAT set molecules, the time-step extrapolated energies deviate on average by only 0.19 kcal/mol from the accurate small time-step energies. For small water clusters, we obtain accurate complete basis-set binding energies using time-step extrapolation with a mean absolute error of 0.07 kcal/mol compared to CCSD(T). Using large time-step ph-AFQMC for the N_2 dimer, we show that accurate bond lengths can be obtained while reducing CPU time by an order of magnitude.

5.1 Introduction

The accurate description of electron-electron correlation in large systems remains a fundamental challenge in solid-state physics and quantum chemistry. When beyond DFT accuracy is needed, one commonly resorts to coupled-cluster singles, doubles, and perturbative triples (CCSD(T))[146,147] or fixed-node diffusion Monte Carlo (FN-DMC).[80,89] Over the past two decades, several accurate correlation-consistent methods have emerged as promising tools for achieving nearly chemical accuracy: density-matrix renormalization group,[122–124] full configuration-interaction quantum Monte Carlo,[87,88,116,148,149] heat-bath configuration interaction,[113,114,150,151] adaptive sampling configuration interaction,[152–154] iterative CI,[155,156] and many-body expansion of full configuration interaction (MBE-FCI).[157–160] Extensive tests on small systems show that these methods yield nearly exact FCI solutions. As a result, they serve as valuable benchmark tools or high-level solvers. However, their application is currently limited to modest system sizes due to high computational costs and other inherent limitations. Besides the mentioned methods, phaseless auxiliary-field quantum Monte Carlo (ph-AFQMC)[8] is one of the most promising alternatives to both CCSD(T) and FN-DMC because of its favorable scaling with system size and because it is readily applicable to molecular and extended systems.

Čížek and Paldus[146,147] introduced the coupled-cluster theory 50 years ago, and since then, it has found extensive use in correlation-consistent calculations. The *gold standard* of quantum chemistry—coupled-cluster singles, doubles, and perturbative triples (CCSD(T))[59,78,119]— has been carefully benchmarked on a wide range of small molecules, achieving nearly chemical accuracy.[119,161] The Grüneis and Chan groups have successfully applied CCSD(T) to solids routinely treating a few hundred electrons.[162–166] However, CCSD(T) is often not accurate enough, especially in the presence of strong static correlation and spin contamination.[119] For instance, the total energy of the CN radical in a double-zeta basis set converges to within 0.3 kcal/mol only at the CCSDTQP level of theory.[120] More importantly, the CCSD(T) theory already exhibits adverse computational scaling ($\mathcal{O}(N^7)$) and higher coupled-cluster expansions, such as CCSDTQP, are accessible only for the smallest systems (20 electrons in 100 orbitals). Similar to stochastic and selected versions of CI, analogous coupled-cluster variants have been proposed. These aim to alleviate the computational scaling of higher coupled-cluster expansions and enhance accuracy beyond CCSD(T).[167–172] More extensive benchmark data for these methods is necessary to judge the performance and accuracy relative to CCSD(T).

Fixed-node diffusion Monte Carlo[80,89,91] (FN-DMC) is a commonly used method for studying solids and molecules containing up to 1000 electrons. It uses a random walk in real space to sample the Hamiltonian expectation values and scales as $\mathcal{O}(N^3)-\mathcal{O}(N^4)$ with system size. DMC requires accurate trial wavefunctions to guide the walker density to the important positions in real space. Typically, Jastrow factors[173–175] on top of the Slater determinant impose cusp conditions. While Jastrow factors yield faster convergence to the complete basis set (CBS) limit, FN-DMC becomes comparable to other quantum chemistry methods only in the CBS limit. Several groups showed that the mean absolute error of the FN-DMC with a single Slater-Jastrow wavefunction is approximately 3 kcal/mol.[126,128,176] Petruzielo *et al.*[128] demonstrated that a variational optimization of orbitals within the Slater-Jastrow wavefunction reduces the error to 2.1 kcal/mol. Furthermore, adding multiple Slater determinants

from small complete active spaces reduces the mean absolute error to 1.2 kcal/mol for the G2 set. To mitigate the fermionic sign problem, DMC relies on the fixed-node approximation. This constrains the nodal structure of the exact many-body ground-state wavefunction to match the nodes of the trial wavefunction. However, the trial wavefunction is the primary source of errors in DMC.[80,177] More accurate trial wavefunctions such as backflow wavefunctions,[178] geminal wavefunctions,[179] pfaffians,[180] or recently introduced deep learning models,[129,130] provide a route for further improvements of the method.

In this work, we will focus on the phaseless auxiliary-field quantum Monte Carlo (ph-AFQMC). Although originally developed as the path integral MC algorithm,[1–4] it experienced a renaissance with the introduction of open-ended random walks and the phaseless approximation.[8] Since then, numerous applications for molecules[9,17,27,30,31,35,41,181–183] and solids[10,18,34,42,184] have confirmed that ph-AFQMC is a promising alternative to CCSD(T) and FN-DMC. It has also been successfully applied to excited states[17,18] and at finite temperature.[185–189] ph-AFQMC exhibits low polynomial scaling ($\mathcal{O}(N^3) - \mathcal{O}(N^4)$) with system size that can even be reduced to cubic scaling by utilizing tensor hypercontractions[23,24], stochastic resolution of identity,[26] or employing a plane wave basis.[10] The *phaseless* approximation controls the fermionic sign problem in ph-AFQMC, however, it also introduces systematic errors that are challenging to control.[8,133] Mahajan *et al.* developed a fast method for the evaluation of the local energies for multi-determinantal trial wavefunctions and demonstrated that the phaseless approximation can be systematically improved using better trial wavefunctions.[50,51] Recently, there have been attempts to directly enhance the phaseless approximation.[41,100,190]

In this work, we focus on reducing the computational prefactor of ph-AFQMC by utilizing large time steps. Larger time steps facilitate faster equilibration, diminish the autocorrelation between subsequent local energy evaluations, and thereby significantly reduce the computational cost to achieve fixed statistical errors (see Sec. 5.2.1). Therefore, every projector QMC method employs the largest time step not compromising the accuracy. For typical systems, ph-AFQMC utilizes time steps around $10^{-3}\,E_\mathrm{h}^{-1}$ without significant time-step errors.[41,47,133] In contrast, FN-DMC permits much larger time steps up to $10^{-1}\,E_\mathrm{h}^{-1}$.[191–193] In FCIQMC, the time step is limited by the maximal excitation energy.[87]

Specifically, we modify the AFQMC algorithm to enable size-consistent simulations with large time steps. We demonstrate that the size-consistency errors in the ph-AFQMC method do not originate from the *cosine projection*, as previously suggested[39], but are due to hybrid energy capping. To eliminate the remaining time-step errors, we investigate various approaches to compute the action of the one-body propagator on a Slater determinant. The optimal method minimizes the required number of $\hat{H}\,|\Psi\rangle$ operations for a set of representative systems. Further, we adapt various propagators within the AFQMC framework and analyze their corresponding leading error terms. We show that the time-step errors agree with the theoretical predictions and that a reliable and robust time-step extrapolation to a zero time-step limit is possible. Finally, we show the accuracy of time-step extrapolated AFQMC energies for a variety of molecular systems and Gaussian basis sets.

The remainder of the paper is organized as follows: in Sec. 5.2.1 we explore the advantages associated with the use of large time steps. We investigate different propagators within the ph-AFQMC framework in Sec. 5.3, followed by a comparison

of methods to compute the exponential of the one-body operator in Sec. 5.4). Then, practical recipes for ph-AFQMC simulations with large time steps are presented in Sec. 5.5. We validate our method through various applications in Sec. 6.4. Finally, Sec. 6.6 summarizes our findings and outlines the perspectives of AFQMC in the simulation of real materials.

5.2 Theoretical Background

This section is partially moved to the Chapter 3 and Appendix E.

5.2.1 Computational Advantage of the Large Time-Step AFQMC

The first advantage of ph-AFQMC with large time steps is the reduction of the number of steps to equilibrate the systems. We need to propagate each walker for N_{eq} steps so that the initial state $|\Psi_{\text{I}}\rangle$ is projected to the ground state. The number of required equilibration steps N_{eq} decreases like $1/\tau$ with the size of the time step.

The second advantage of large time-steps is the reduction of the autocorrelation between subsequent samples. After taking a sample of the energy, one needs to propagate for κ steps to avoid autocorrelation between the samples. Ideally, we would increase the time step until $\kappa = 1$ so that we can sample the energy after every time step.

In practice, the benefits of large time steps are reduced by the fact that the energy does not have to be measured at each time step, if the samples are correlated. However, other tasks that constitute the random walk (creation of the effective Hamiltonian, AFQMC propagation, and the force bias calculation) are still needed at each time step.[41]

5.3 AFQMC Propagators

The exact many-body propagator is represented by

$$\hat{U}(\tau) = e^{-\tau(\hat{H}_1+\hat{H}_2)}, \tag{5.1}$$

where $\hat{H}_1$ and $\hat{H}_2$ are the one- and two-body terms defined in Eq. (2.10). In the AFQMC method, it is formally necessary to employ a split-operator method to separate $e^{-\tau\hat{H}_2}$ from $e^{-\tau(\hat{H}_1+\hat{H}_2)}$, for example using first order split technique (Split-1)

$$e^{-\tau(\hat{H}_1+\hat{H}_2)} \approx e^{-\tau\hat{H}_1}e^{-\tau\hat{H}_2}. \tag{5.2}$$

For $e^{-\tau\hat{H}_2}$ the Hubbard-Stratonovich transformation is then used:

$$e^{-\tau\hat{H}_2} = \frac{1}{N_w}\sum_w e^{-\tau\hat{\mathcal{H}}_w} + \tau^2\hat{E}_{\text{HS}} + \mathcal{O}(\tau^3), \tag{5.3}$$

with the effective interaction introduced in Eq. (3.22). After some algebra, we derive the leading error term of this transformation

$$\hat{E}_{\text{HS}} = \frac{1}{48}\sum_{g\neq g'}\{\hat{L}_g\hat{L}_{g'},[\hat{L}_{g'},\hat{L}_g]\} + \frac{1}{24}\sum_{g\neq g'}[\hat{L}_g,[\hat{L}_g,\hat{L}_{g'}^2]], \tag{5.4}$$

where $\{A,B\} = AB + BA$ and $[A,B] = AB - BA$. The exact propagator is reproduced in the limit $N_w \to \infty$ and in case that $\hat{L}_g$ operators commute. Note that in Eq. (5.4), we only show the systematic errors remaining after integrating over the random fields and not the statistical errors from the Monte Carlo sampling.

After applying the Hubbard-Stratonovich transformation, one can choose to either evaluate the split propagator directly or refactorize it back to derive a full effective Hamiltonian $\hat{H}_1 + \hat{\mathcal{H}}_w$ and then apply any approximation to $e^{-\tau(\hat{H}_1+\hat{\mathcal{H}}_w)}$. In the subsequent analysis, we examine two split propagators where the matrix exponentials are evaluated by applying methods outlined in Sec. 5.4. Additionally, we examine two more propagators where the refactorized $e^{-\tau\hat{\mathcal{H}}_w}$ is approximated directly.

5.3.1 Split-1 Propagator

The simplest propagator splitting of the one-body Hamiltonian and the effective interaction is

$$\hat{U}_{\mathrm{S1}}(\tau) = \frac{1}{N_w}\sum_w e^{-\tau\hat{H}_1} e^{-\tau\hat{\mathcal{H}}_w}. \tag{5.5}$$

This has the advantage of reducing the number of necessary operations, however, the split-1 propagator leads to a sizable time-step error

$$\hat{U}_{\mathrm{S1}}(\tau) = \hat{U}(\tau) + \tau^2\hat{E}_{\mathrm{S1}} + \mathcal{O}(\tau^3) \tag{5.6}$$

with the leading term

$$\hat{E}_{\mathrm{S1}} = \frac{1}{2}[\hat{H}_1, \hat{H}_2] + \hat{E}_{\mathrm{HS}}, \tag{5.7}$$

where $\hat{E}_{\mathrm{HS}}$ is the error arising from the Hubbard-Stratonovich transformation (Eq. 5.4). Since, the one-body propagator $e^{-\tau\hat{H}_1}$ remains constant during the simulation, we precomputed it exactly using matrix diagonalization. Conversely, $e^{-\tau\mathcal{H}_w}$ is generated anew for each walker and time step. Sec. 5.4 discusses efficient techniques for the evaluation of this term.

5.3.2 Split-2 Propagator

Split propagators are more accurate with second-order decomposition

$$\hat{U}_{\mathrm{S2}}(\tau) = \frac{1}{N_w}\sum_w e^{-\tau\hat{H}_1/2} e^{-\tau\hat{\mathcal{H}}_w} e^{-\tau\hat{H}_1/2}. \tag{5.8}$$

The advantage of this approach is that it does not introduce additional errors beyond the Hubbard-Stratonovich transformation to quadratic order

$$\hat{U}_{\mathrm{S2}}(\tau) = \hat{U}(\tau) + \tau^2\hat{E}_{\mathrm{HS}}. \tag{5.9}$$

Similar to the Split-1 propagator, the term $e^{-\tau\hat{H}_1/2}$ is precomputed exactly in our implementation.

5.3.3 Taylor Propagator

The simplest propagator within the AFQMC formalism is obtained by the Taylor expansion of the refactorized time propagator $e^{-\tau(\hat{H}_1+\hat{\mathcal{H}}_w)}$

$$\hat{U}_{\mathrm{T}}(\tau) = \frac{1}{N_w}\sum_w e^{-\tau(\hat{H}_1+\hat{\mathcal{H}}_w)} = \hat{U}(\tau) + \tau^2\hat{E}_{\mathrm{T}} + \mathcal{O}(\tau^3). \tag{5.10}$$

The leading error term in this expansion is

$$\hat{E}_{\mathrm{T}} = \frac{1}{12}\sum_g \big[[\hat{L}_g,\hat{H}_1],\hat{L}_g\big] + \hat{E}_{\mathrm{HS}}, \tag{5.11}$$

provided that the Taylor expansion is truncated at an order $k \geq 4$.

5.3.4 Crank-Nicolson Propagator

The Crank-Nicolson propagator replaces the matrix exponential by a linear problem

$$\hat{U}_{\mathrm{CN}}(\tau) = \frac{1}{N_w}\sum_w \big(1+\tau(\hat{H}_1+\hat{\mathcal{H}}_w)/2\big)^{-1}\big(1-\tau(\hat{H}_1+\hat{\mathcal{H}}_w)/2\big). \tag{5.12}$$

The corresponding leading error term is

$$\hat{U}_{\mathrm{CN}}(\tau) = \hat{U}(\tau) + \tau^2\hat{E}_{\mathrm{CN}} + \mathcal{O}(\tau^3) \tag{5.13}$$

with

$$\hat{E}_{\mathrm{CN}} = \frac{1}{4}\{\hat{H}_1,\hat{H}_2\} + \frac{1}{8}\sum_g \big[[\hat{L}_g,\hat{H}_1],\hat{L}_g\big] + \hat{E}_{\mathrm{HS}}. \tag{5.14}$$

5.3.5 Summary

In summary, the error terms specified above suggest that the Split-2 propagator is the optimal propagator within the AFQMC framework with the leading error term dictated by the Hubbard-Stratonovich transformation. We will show below that this is also confirmed by numerical examples, albeit Taylor expansion will also yield excellent results almost on par with the Split-2 propagator. Conversely, the split-1 and the Crank-Nicolson propagator show significantly worse results.

5.4 Exponential of the One-Body Operator within AFQMC

To propagate using the Split-2 propagator, we need to compute the action of the matrix exponential $e^{-\tau\hat{\mathcal{H}}_w}$ and then apply it to the orbitals in $|\Psi_w\rangle$. One could use exact matrix diagonalization[102,194] to compute $e^{-\tau\hat{\mathcal{H}}_w}$; however, this is computationally expensive especially because $\hat{\mathcal{H}}_w$ is non-Hermitian (see Eq. 3.22). While of limited practical utility, spectral decomposition still serves as a valuable benchmark tool. We will use it to evaluate the accuracy of iterative methods.

An alternative is to use iterative methods to directly compute $e^{-\tau\hat{\mathcal{H}}_w}|\Psi_w\rangle$. All iterative methods involve $\hat{\mathcal{H}}_w|\Psi_w\rangle$ operations that are the most expensive part of the procedure. Consequently, the optimal method for a fixed time step τ is the one that minimizes the number of $\hat{\mathcal{H}}_w|\Psi_w\rangle$ operations. To simplify the notation, we will use $\hat{A} = -\tau\hat{\mathcal{H}}_w$ throughout the remainder of this section.

5.4.1 Taylor Expansion

The Taylor expansion offers a simple and robust scheme to approximate matrix exponentials

$$\text{taylor}_k\{A, |\Psi\rangle\} = \sum_{n=0}^{k} \frac{A^n}{n!} |\Psi\rangle \ . \tag{5.15}$$

k is the order of the approximation and the number of $A|\Psi\rangle$ operations needed to approximate the exponential. The scaling of the algorithm is dominated by $A|\Psi\rangle$ operations and scales as kN^2N_e, where k is the expansion order, N denotes the number of basis functions, and N_e is the number of electrons in the system. Taylor expansion with $k = 6$ is usually used in the AFQMC community.[51,144]

5.4.2 Chebyshev Expansion

Ezer *et al.*[195] demonstrated that, although the error terms of different polynomial expansions are of the same order, the Chebyshev polynomials $T_n(x)$ minimize the prefactor of the leading error term compared to other polynomial expansions. They are conveniently defined using the following recurrence relation

$$\begin{aligned} T_0(x) &= 1 \\ T_1(x) &= x \\ T_n(x) &= 2xT_{n-1}(x) - T_{n-2}(x). \end{aligned} \tag{5.16}$$

The Chebyshev expansion is then formally given by

$$\text{cheb}_k\{A, |\Psi\rangle\} = \sum_{n=0}^{k} c_n T_n(A) |\Psi\rangle \ . \tag{5.17}$$

For the matrix exponential, the expansion coefficients c_n are

$$c_n = \begin{cases} J_n(i) & n = 0 \\ 2i^n J_n(-i) & n > 0, \end{cases} \tag{5.18}$$

where $J_n(z)$ are the Bessel functions of the first kind. The k-th order Chebyshev expansion requires $k\,A|\Psi\rangle$ operations and scales as kN^2N_e, same as the Taylor expansion.

5.4.3 Krylov Subspace Projection

The Krylov subspace $\mathcal{K}_k(A, \psi)$ for the matrix A and an orbital vector ψ is

$$\mathcal{K}_k(A, \psi) = \text{span}\{\psi, A\psi, A^2\psi, ..., A^{k-1}\psi\}. \tag{5.19}$$

In our case, ψ is the N-dimensional vector of the orbital expansion coefficients in the Slater determinant $|\Psi\rangle = |\psi_1, \psi_2, ..., \psi_{N_e}\rangle$. For the non-Hermitian A, one can use the Arnoldi algorithm[102,194] to produce an orthonormal basis $B_k = [b_1, b_2, ..., b_k]$ and the operator A_k in the subspace

$$A_k = B_k^\dagger A B_k. \tag{5.20}$$

A_k is a $k \times k$ upper Hessenberg matrix.[102] B_k is a $N \times k$ matrix with the first column $b_1 = \psi/||\psi||$ and

$$B_k^\dagger B_k = \mathbb{1}_{k\times k}, \qquad B_k B_k^\dagger \approx \mathbb{1}_{N\times N}. \tag{5.21}$$

Using this property, one can approximate the matrix exponential as follows:

$$\begin{aligned} e^A \psi &\approx B_k B_k^\dagger e^A \overbrace{B_k e_1 ||\psi||}^{\psi} \\ &= B_k e^{A_k} e_1 ||\psi||, \end{aligned} \tag{5.22}$$

where e_1 is the first unit vector in $\mathbb{C}^k$ and $B_k e_1 = b_1$. The Krylov approximation to the matrix exponential of the order k is then simply given by

$$\text{krylov}_k\{A, \psi\} = B_k e^{A_k} e_1 ||\psi||. \tag{5.23}$$

Like the polynomial expansions, the $A|\Psi\rangle$ applications dominate the computational cost of the Krylov method with kN^2N_e operations. In addition, the Arnoldi algorithm scales as kNN_e^2 and one needs to compute the matrix exponential in subspace $e^{-\tau A_k}$. The latter is typically not expensive because k is very small compared to N; one computes it using matrix diagonalization, a higher-order polynomial expansion, or a Padé approximation.

5.4.4 Block-Krylov Subspace Projection

Contrary to the previous algorithm that expands each orbital in the Slater determinant individually, the block-Krylov projection simultaneously computes the action of the exponential operator on all orbitals. As a consequence, the Krylov subspace increases by N_e elements in each Arnoldi iteration, and k-th order Krylov subspace consists of kN_e vectors. The Krylov subspace is

$$\mathcal{K}_k(A, |\Psi\rangle) = \text{span}\{\Psi, A\Psi, A^2\Psi, ..., A^{k-1}\Psi\}, \tag{5.24}$$

where Ψ denotes the $N \times N_e$ dimensional matrix of the expansion coefficients. The orthonormal basis $B_k = [\bar{B}_1, \bar{B}_2, ..., \bar{B}_k]$ is now a $N \times kN_e$ matrix, where $\Psi = \bar{B}_1 R$, and can be computed using a QR decomposition. Note that the initial orthogonalization of orbitals is necessary due to the imaginary-time propagation employed in AFQMC. The projected operator A_k is computed analogously to Eq. (5.20) and is an upper block Hessenberg matrix of the size $kN_e \times kN_e$. The approximation of the exponential is similar to Eq. (5.23)

$$\text{bkrylov}_k\{A, |\Psi\rangle\} = B_k e^{A_k} E_{N_e} R, \tag{5.25}$$

where E_{N_e} is the $kN_e \times N_e$ part of the kN_e-dimensional identity matrix. For a given order k, the blocked Krylov method requires the same number of $A|\Psi\rangle$ operations as the non-blocked version. The advantage of the blocked algorithm is that it may converge in fewer iterations because the space spanned by other orbitals is used to expand the exponential as well. Furthermore, matrix-matrix multiplications often achieve more floating-point operations per second than matrix-vector multiplications. The disadvantage is that the dimension of the Krylov subspace scales with the number of electrons N_e so that the Arnoldi iteration requires additional $k^2NN_e^2$ operations

and the exponentiation in subspace requires roughly $k^3 N_e^3$ operations. The total computational cost to perform k_K-th order block Krylov expansion increases by the factor $\frac{k_\mathrm{K}}{k_\mathrm{T}}\left(1+\frac{k_\mathrm{K}N_e}{N}+\left(\frac{k_\mathrm{K}N_e}{N}\right)^2\right)$ compared to the k_T-th order Taylor expansion. This can add computational overhead for small basis sets, but for larger basis sets the computational overhead is usually negligible, especially when compared to other more expensive tasks in AFQMC[41].

5.4.5 Performance Comparison

We compare the different matrix-exponential methods for a short ph-AFQMC simulation using 10 time steps and 2 400 walkers and calculate the error in the ph-AFQMC total energy induced by the errors in calculating the matrix exponential. Then we determine the minimal number of $\hat{A}\,|\Psi\rangle$ operations k_min required to achieve a specified accuracy $\varepsilon = 10^{-5}\,E_\mathrm{h}$. The exact diagonalization described at the beginning of the section yields the reference energies. We average k_min over 22 different systems for time steps from $\tau = 0.01\,E_\mathrm{h}^{-1}$ to $\tau = 0.3\,E_\mathrm{h}^{-1}$ and for two different basis sets (cc-pVDZ and cc-pVTZ). In Ref.[196], we provide the list of considered compounds, ranging from small molecules to benzene-like cyclic compounds.

Fig. 5.1 compares the different exponentiation methods and demonstrates that Krylov methods need less $\hat{A}\,|\Psi\rangle$ operations than the Taylor and the Chebyshev expansion. Furthermore, k_min increases with the time step and this is more pronounced for the Taylor and the Chebyshev expansion than for the Krylov methods. k_min is also more sensitive to the system for the Taylor and the Chebyshev expansion leading to larger error bars for these methods. Hence, one needs to verify the order of the expansion for every system in particular for larger timesteps. Finally, the larger cc-pVTZ basis set needs slightly larger k_min than the smaller cc-pVDZ basis set.

5.5 Modified AFQMC Algorithm

In this section, we present modifications of the commonly used AFQMC algorithm[41,47,133] that allow large time steps in AFQMC and reliable time step extrapolation.

5.5.1 Local-Energy Capping

Inspired by Zen *et al.*[192], we implement the local energy capping as

$$\bar{E}_\mathrm{L}(\Psi) = \begin{cases} E_0 - \Delta E & \text{if} \quad E_\mathrm{L}(\Psi) < E_0 - \Delta E \\ E_0 + \Delta E & \text{if} \quad E_\mathrm{L}(\Psi) > E_0 + \Delta E \\ E_\mathrm{L}(\Psi) & \text{else.} \end{cases} \tag{5.26}$$

Here, E_0 is the best estimate of the ground-state energy and the energy window is $\Delta E = \frac{1}{2}\sqrt{\frac{N_e}{\tau}} + \sqrt{N_e \tau}$. This window increases with the number of electrons as opposed to $\Delta E = \sqrt{\frac{2}{\tau}}$ typically used in AFQMC.[184] We also add a term proportional to $\sqrt{\tau}$ to avoid excessively strong capping for large time steps. The energy capping introduces a bias, potentially affecting the accuracy of the time step extrapolation. To strike a balance, we opt to cap the local energy to control its variance only—a parameter far

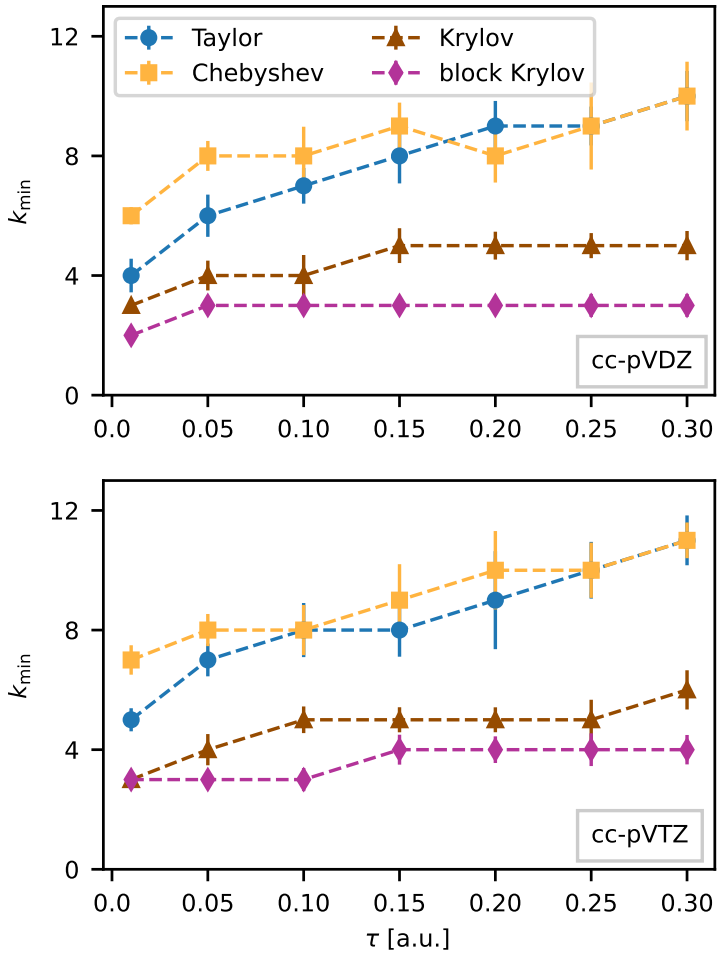

Figure 5.1: The number of $A|\Psi\rangle$ operations, i.e. the order of the method $k_{\min}$ required to achieve an accuracy of $\varepsilon = 10^{-5}\,E_\mathrm{h}$ in the ph-AFQMC energy for different matrix-exponentiation methods. The local energy is averaged over 10 time steps and 2 400 walkers. $k_{\min}$ is averaged over 22 systems. Note that the error bars correspond to the standard deviation of the average over the 22 systems and not the statistical fluctuations of the AFQMC simulation. Krylov methods (nonblocked, brown triangles; blocked, magenta diamonds) outperform the Taylor (blue circles) and the Chebyshev (yellow squares) expansion typically utilized in ph-AFQMC codes. The cc-pVDZ basis set (top) needs fewer $A|\Psi\rangle$ operations than the cc-pVTZ basis set (bottom).

more sensitive to rare events than the mean value. The energy capping is usually applied for the hybrid energy (Eq. (3.37)), too. We turn off hybrid energy capping because it strongly affects the time-step errors.

5.5.2 No Hybrid-Energy Capping

The energy capping is usually applied for the hybrid energy (Eq. (3.37)), too. We turn off hybrid energy capping because it strongly affects the time-step errors. In particular, we observe that hybrid-energy capping can introduce strong size-consistency errors. We will discuss this in more depth later in this section.

5.5.3 Reweighting Factor Capping

To compensate for the lack of hybrid energy capping, we restrict the reweighting factor in Eq. (3.42)

$$\overline{e^{-\tau(E_\mathrm{H}-E_0)}} = \begin{cases} e^{-\tau(E_\mathrm{H}-E_0)} & \text{if} \quad e^{-\tau(E_\mathrm{H}-E_0)} < 10 \\ 0 & \text{else .} \end{cases} \tag{5.27}$$

This is as effective as the hybrid-energy capping and does not cause size-consistency errors.

5.5.4 Force-Bias Capping

Force-bias capping is essential for stable AFQMC simulations. We recommend capping the force bias with

$$\bar{f}_g = \begin{cases} f_g & \text{if} \quad |f_g| < 1 \\ 0 & \text{else .} \end{cases} \tag{5.28}$$

to minimize the fluctuations and time-step errors. We find that removing the force-bias components with large absolute values is more reliable for large time steps than the conventional choice of capping them at an absolute value of 1.

5.5.5 No Energy Mixing

Many implementations modify Eq. (3.42) to include a mixture $E_\mathrm{H}^\mathrm{mix}$ of the current and previous hybrid energy[51,99]

$$W_{k+1,w} e^{i\theta_{k+1,w}} = W_{kw} e^{i\theta_{kw}}\, e^{-\tau(E_\mathrm{H}^\mathrm{mix}-E_0)}, \tag{5.29}$$

However, we find that energy mixing deteriorates the time-step extrapolation, so we do not use it in this work.

5.5.6 Accurate Matrix Exponentials

Reliable time-step extrapolation requires minimizing remaining errors caused by approximating the exponential of the effective interaction $\hat{\mathcal{H}}$. We recommend using either the Krylov projection method with $k = 5$ or the Block-Krylov method with $k = 4$ for this purpose (see Sec. 5.4).

5.5.7 Size Consistency Errors

To quantify the effect of the listed modifications, we test the size consistency of the algorithms similar to Zen *et al.*[192] and Lee *et al.*[39] The former group considers a CH_4-H_2O dimer at a separated C-O distance of 11.44 Å using the cc-pVDZ basis set. We measure the size-consistency error using

$$E_s = E^{\text{separated}}_{CH_4-H_2O} - E_{CH_4} - E_{H_2O}. \tag{5.30}$$

Lee *et al.*[39] investigates a chain of N_2 molecules at large separation. They considered the AFQMC correlation energy per N_2 molecule E_{corr}/k as a measure of size consistency.

We expect that E_s is less than 0.01 mE_h for size-consistent methods. For the CH_4-H_2O dimer (Fig. 5.2, top), the standard algorithm and our modifications yield small size-consistency errors E_s at small time steps $\tau = 0.05\ E_h^{-1}$. However, the standard algorithm exhibits sizable errors at larger time steps ($\approx 0.4\,\text{m}E_h$ at $\tau = 0.20\,E_h^{-1}$), whereas the modified algorithm is size-consistent for all time steps. These size-consistency errors directly impact the binding energy

$$E_b = E^{\text{bonded}}_{CH_4-H_2O} - E_{CH_4} - E_{H_2O}, \tag{5.31}$$

where the bonded C-O distance is 0.63 Å. Fig. 5.2(bottom) shows similar-size deviations of the energy when the dimer is bound. Hence, the standard algorithm requires much smaller time-steps to achieve the same level of accuracy as the algorithm presented in this work.

For the N_2 chain, we revisit the work of Lee *et al.*[39] Using the traditional algorithm, we can reproduce the size-consistency errors for large time steps $0.05\,E_h^{-1}$ (see Fig. 5.3). Previously, it has been suggested[39] that this error originates from the *cosine projection* in the phaseless approximation. However, deactivating the hybrid energy capping suppresses most size-consistency errors. The errors are not larger in magnitude than the size-consistency errors at the small time step $\tau = 0.005\,E_h^{-1}$.

5.5.8 Time-Step Extrapolation of ph-AFQMC Energies

Generally, the time-step errors in the total energy follow a quadratic relation

$$E(\tau) = E_0 + \alpha\tau + \beta\tau^2 \tag{5.32}$$

for all propagators and trial wavefunctions. The quadratic term directly emerges from the analysis of the propagators (Sec. 5.3), whereas the linear term is attributed to the cosine projection (Eq. 4.1) and perturbations introduced in the Monte Carlo algorithm to maintain the stability of the random walk (Sec. 5.5.A – 5.5.D). The top plot in Fig. 5.4 illustrates the time-step errors for the absolute ph-AFQMC energies of the $2C_S$ water dimer with the cc-pVDZ basis set. Notably, the Split-2 propagator exhibits the smallest time-step errors predominantly characterized by the quadratic term. The Taylor propagator shows similar behavior with slightly larger time-step errors. Conversely, both the Crank-Nicolson and the Split-1 propagator show larger time-step errors primarily governed by the linear term.

The bottom plot of Fig. 5.4 displays the time-step extrapolation for relative energies, specifically the binding energy of the $2C_S$ water dimer. For relative energies, time-step

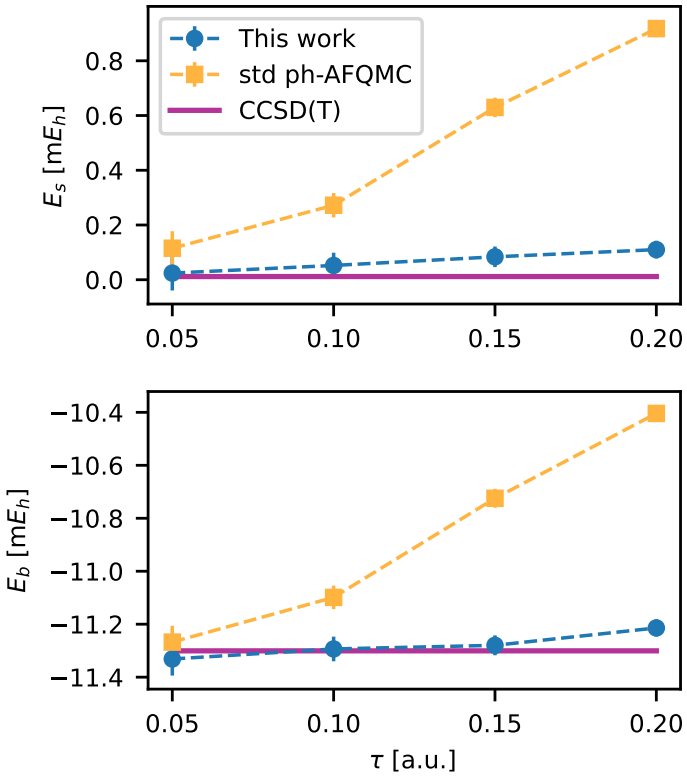

Figure 5.2: (Top) The size-consistency error E_s and (bottom) the binding energy E_b for a CH_4-H_2O dimer using a cc-pVDZ basis set. We compare the standard ph-AFQMC algorithm (yellow squares), our modified algorithm (blue circles), and CCSD(T) results (magenta line).

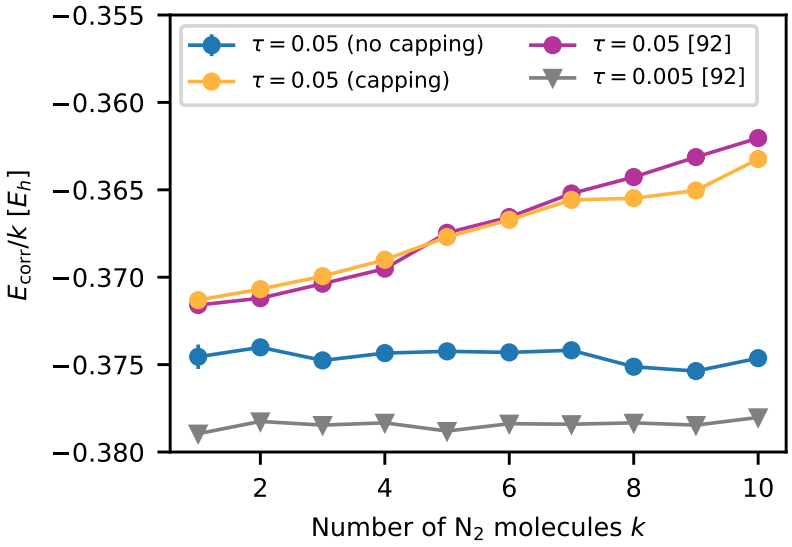

Figure 5.3: Correlation energy per N_2 molecule as a function of the number of infinitely separated N_2 molecules. We compare our data with the data from Lee *et al.*[39] Reference results at $\tau = 0.005\,E_h^{-1}$ (in gray) are size-consistent, while at the larger time step $\tau = 0.05\,E_h^{-1}$, size-consistency is maintained only when hybrid energy capping is not employed (in blue). In contrast, our results using hybrid energy capping show significant size-consistency errors (in yellow) and are consistent with previous results (in magenta).

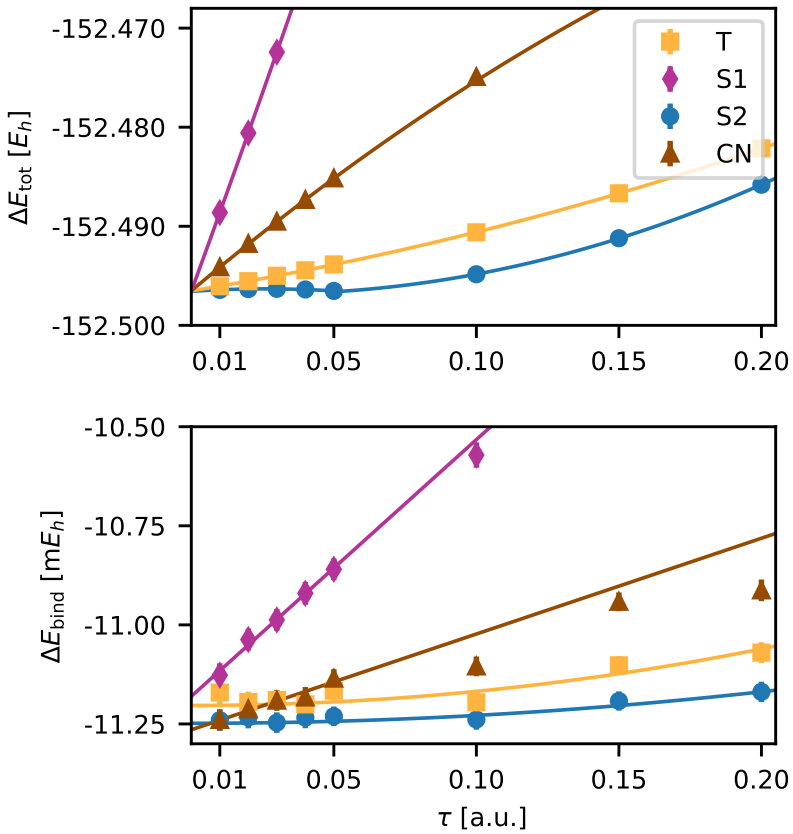

Figure 5.4: Time-step errors in the total energy (top) and the binding energy (bottom) of the $2C_S$ cluster for different AFQMC propagators. Time steps $< 0.05\,E_h^{-1}$ are used for the linear extrapolation of the binding energy with the Crank-Nicolson (brown triangles) and the Split-1 (magenta diamonds) propagators, while all time steps are used for the quadratic extrapolation with the Taylor (yellow squares) and the Split-2 (blue circles) propagator. All calculations use the frozen-core approximation and the cc-pVDZ basis set.

errors cancel by 1–2 orders of magnitude compared to the absolute energies. Again, the Split-2 and Taylor propagators show the smallest time-step errors with vanishingly small linear terms. For these propagators and this system, the time-step errors are so small ($< 0.1\,\mathrm{m}E_\mathrm{h}$) that extrapolation is not necessary and the binding energy could be determined by a single calculation. Conversely, for the Split-1 and Crank-Nicolson propagators, the linear term remains significant, leading to larger time-step errors. Based on these observations, we recommend a general rule for extrapolation of the binding energies: use

$$E(\tau) = E_0 + \beta\tau^2 \tag{5.33}$$

for propagators where quadratic errors dominate (Split-2 and Taylor), and

$$E(\tau) = E_0 + \alpha\tau \tag{5.34}$$

for those propagators with the predominant linear term (Split-1 and Crank-Nicolson). As a rule of thumb, we observe that time-step extrapolation decreases time-step errors by an order of magnitude.

5.6 Applications and Discussion

In the following three subsections, we (i) compare accurate ph-AFQMC energies obtained with small time steps[41] to extrapolating the energies from large time-steps, (ii) extrapolate the binding energies of small water clusters in the heavy-augmented double-zeta basis set and in the CBS limit, and (iii) calculate the equilibrium bond length of the N_2 dimer using large time-step ph-AFQMC calculations.

5.6.1 HEAT Set Total Energies

We calculate the total energies for the molecules in the HEAT set[45] using the Split-2 propagator and time-step extrapolation. We include Cholesky vectors up to a threshold of $10^{-6}\,E_\mathrm{h}$ and sample with the Hartree-Fock trial determinant. We use Dunning's cc-pVDZ basis set and the frozen-core approximation ($1s$ shell for B-F atoms). To verify the reliability of the time-step extrapolation, we utilized 4 equidistant time steps ranging between $0.05\,E_\mathrm{h}^{-1}$ and $0.20\,E_\mathrm{h}^{-1}$. We perform each ph-AFQMC simulation using 2 400 walkers, with 2 000 equilibration steps, and 10 000 time steps during the sampling phase. To have accurate reference values for comparison, we perform small time-step ph-AFQMC simulations with $\tau = 0.002\,E_\mathrm{h}^{-1}$, 4 800 walkers, 100 000 equilibration steps, and 400 000 sampling steps. This setup guarantees roughly identical statistical errors for the small time-step and extrapolated energies, but the CPU time to obtain extrapolated energies is reduced by a factor of 20 using large time steps. All calculations are performed using the QMCFort code and a single CPU node (dual-socket Intel Skylake Platinum 8174) per system.

Fig. 6.7 compares the large time-step and extrapolated ph-AFQMC energies with the reference ones at $\tau = 0.002\,E_\mathrm{h}^{-1}$. The ph-AFQMC energies at $\tau = 0.10\,E_\mathrm{h}^{-1}$ exhibit sizable time-step errors with a mean error of $1.89\,\mathrm{m}E_\mathrm{h}$. The time-step errors lead to a consistent under-correlation. Reducing the time step to $\tau = 0.05\,E_\mathrm{h}^{-1}$ reduces the mean error to $0.53\,\mathrm{m}E_\mathrm{h}$ (already a small fraction of the desired chemical accuracy of $1.59\,\mathrm{m}E_\mathrm{h}$). The extrapolated energies are accurate with a mean absolute error of $0.31\,\mathrm{m}E_\mathrm{h}$. The mean signed error of $0.06\,\mathrm{m}E_\mathrm{h}$ shows that the extrapolated energies are not systematically biased compared to the reference small time-step energies.

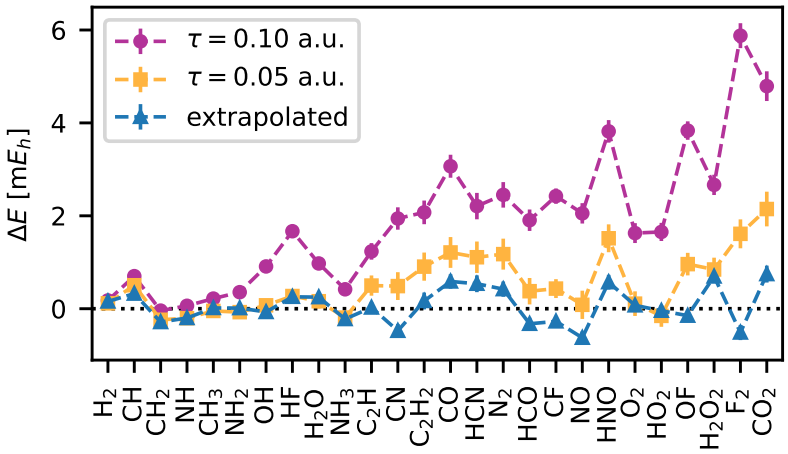

Figure 5.5: Comparison of time-step extrapolated and large time-step energies ($\tau = 0.05\,E_\mathrm{h}^{-1}$ and $\tau = 0.10\,E_\mathrm{h}^{-1}$) against reference values for 26 molecules in the HEAT set. Reference values are obtained using small time-step ph-AFQMC with $\tau = 0.002\,E_\mathrm{h}^{-1}$. All computations use the cc-pVDZ basis set and the frozen-core approximation.

5.6.2 Water Clusters

As a second example, we apply time-step extrapolation to determine the binding energies of the water clusters. We utilize the Split-2 propagator at three distinct time steps ($\tau = 0.10$, $\tau = 0.15$, and $\tau = 0.20\,E_\mathrm{h}^{-1}$) to extrapolate the binding energies using Eq. (5.33). To make reference calculations with a small time step possible, we employ the heavy-augmented double-zeta basis set. Furthermore, we obtain the CBS limit using the aug-cc-pVNZ ($N = \mathrm{D,T,Q}$) basis sets and a 4-5 inverse polynomial extrapolation scheme[145]

$$E_\mathrm{CBS} = E_N + \frac{b}{(N+1)^4} + \frac{c}{(N+1)^5} \tag{5.35}$$

due to its superior behavior compared to the standard inverse cubic extrapolation scheme. Here, E_CBS is the energy in the complete basis set, N is the largest angular momentum in the aug-cc-pVNZ basis set ($N = 2-4$ for $N = \mathrm{D,T,Q}$), and E_N is the corresponding energy.

Each ph-AFQMC calculation is performed using 2 400 walkers and 50 000 time steps, except for the water molecule, where we used 9 600 walkers and 200 000 time steps to minimize binding energy errors. The computational setup is described in more detail in our previous work.[41] As an illustrative example, the largest calculation was performed on the 5CYC cluster using the aug-cc-pVQZ basis set, comprising 855 orbitals, 40 electrons, and 5685 Cholesky vectors. Executed on 4 CPU nodes (dual-socket AMD Epyc 7713), this calculation took 8 days to complete (average performance of 40 GFLOPS/core).

Table 5.1 presents time-step extrapolated ph-AFQMC binding energies for water clusters and compares them with MP2, CCSD(T), and small time-step ($\tau = 0.01\,E_\mathrm{h}^{-1}$) ph-AFQMC values reported in our previous work.[41] The time-step extrapolated binding energies are within the error bars in agreement with the small time-step ph-AFQMC values and also agree with MP2 and CCSD(T) values within chemical accuracy. Com-

Table 5.1: Binding energies of the four most stable water clusters calculated using a heavy-augmented cc-pVDZ basis set and all-electron wavefunctions. MP2, CCSD(T), small time-step ph-AFQMC, and time-step extrapolated ph-AFQMC values (ph-AFQMC(x)) are given in kcal/mol.

Cluster	MP2	CCSD(T)	ph-AFQMC [41]	ph-AFQMC(x)
2Cs	-5.22	-5.18	-5.17(05)	-5.24(3)
3UUD	-15.83	-15.62	-15.67(09)	-15.81(4)
4S4	-28.36	-27.87	-28.12(10)	-28.14(5)
5CYC	-37.48	-36.78	-37.14(28)	-37.27(6)

Table 5.2: CBS binding energies of the four most stable water clusters estimated using aug-cc-pV(D,T,Q) basis sets and 4-5 inverse polynomial extrapolation scheme. Frozen-core approximation is employed. MP2, CCSD(T), and time-step extrapolated ph-AFQMC values in kcal/mol are reported.

Cluster	MP2 [145]	CCSD(T) [145]	ph-AFQMC(x)
2Cs	-5.00	-5.03	-4.98(03)
3UUD	-15.72	-15.70	-15.82(05)
4S4	-27.64	-27.43	-27.53(08)
5CYC	-36.38	-36.01	-36.01(10)

pared to the small time-step ph-AFQMC calculations, the total number of samples is reduced by a factor of 2, while concurrently reducing the statistical errors, too. We used a simple expression to estimate the statistical error σ_x for the extrapolated energies

$$\sigma_x = \frac{\sqrt{\sum_{i=1}^{N_\tau} \sigma_i^2}}{N_\tau} , \tag{5.36}$$

where N_τ is the number of time steps used for the extrapolation and σ_i denotes the estimated 1σ error for each of the time steps.

Table 5.2 lists the MP2, CCSD(T),[145] and our time-step extrapolated ph-AFQMC binding energies in the CBS limit. Small time-step ph-AFQMC calculations are not possible in the CBS limit due to the large computational cost. The mean absolute error between our results and MP2 amounts only to 0.15 kcal/mol. The ph-AFQMC results deviate even less from CCSD(T) with a mean absolute error of 0.07 kcal/mol.

We estimate the statistical errors of the extrapolated binding energies using Eq. (5.36). Moreover, for the statistical errors after the basis set extrapolation, we used the corresponding errors observed at the aug-cc-pVQZ basis set. We note that the CCSD(T) values are approximated by adding the difference between CCSD(T) and MP2 at the aug-cc-pVDZ basis set to the CBS MP2 binding energies.

As an example, we show the time-step extrapolation of the binding energy for the 3UUD water cluster at the aug-cc-pVQZ basis set in Fig. 5.6(top). Fig. 5.6(bottom) illustrates the basis set extrapolation for the same cluster.

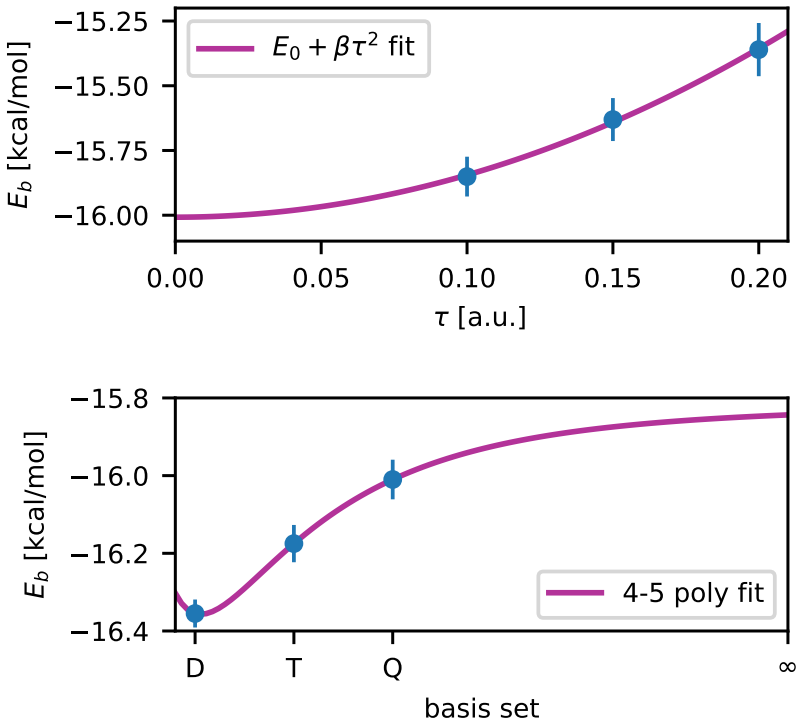

Figure 5.6: (Top) Time-step extrapolation of the binding energy for the 3UUD water cluster at the aug-cc-pVQZ basis set. Eq. (5.33) is used to estimate the zero time-step limit. (Bottom) Basis set extrapolation of the binding energy for the 3UUD water cluster using aug-cc-pV(D,T,Q) basis sets and 4-5 inverse polynomial extrapolation technique.

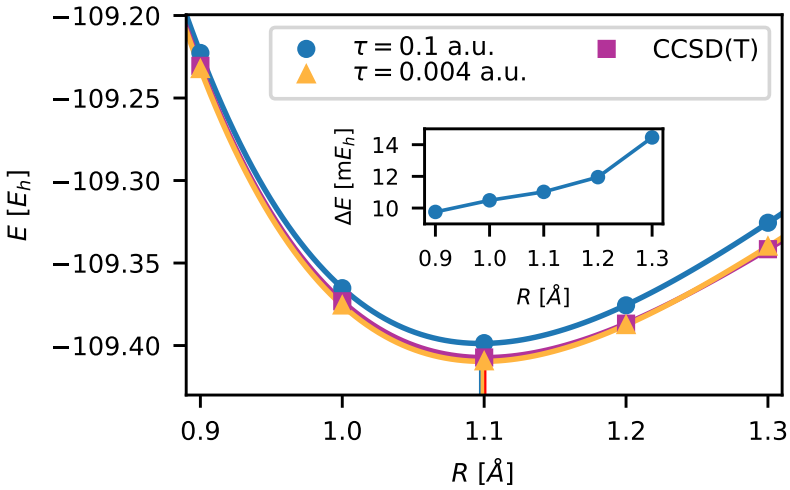

Figure 5.7: The potential energy curves E obtained for CCSD(T), ph-AFQMC with $\tau = 0.004\,E_\mathrm{h}^{-1}$, and ph-AFQMC at $\tau = 0.1\,E_\mathrm{h}^{-1}$ using aug-cc-pVQZ basis set. Five equidistant bond lengths in the range from 0.9 Å to 1.3 Å are used to fit the Morse potential. The equilibrium bond lengths agree closely with the experimental value. Furthermore, the inset illustrates the behavior of ph-AFQMC time-step errors ΔE with increasing bond length.

Table 5.3: Equilibrium bond lengths of the N_2 molecule for different levels of theory: CCSD(T), ph-AFQMC with small time step, and the ph-AFQMC at large time step.

Method	R_0 [Å]
CCSD(T)	1.100(1)
ph-AFQMC @ $0.004\,E_\mathrm{h}^{-1}$	1.099(2)
ph-AFQMC @ $0.1\,E_\mathrm{h}^{-1}$	1.098(2)
Experiment	1.098 [197]

5.6.3 Equilibrium Geometry of the N_2 Molecule

Unlike the total energies, properties such as energy differences, bond lengths, and lattice constants exhibit significantly lower sensitivity to time-step errors. Using the N_2 molecule, we demonstrate that accurate bond lengths are successfully obtained with single-point, large time-step ph-AFQMC calculations. Using the aug-cc-pVQZ basis set and a RHF trial wave function, we calculate ph-AFQMC energies for five equidistant bond lengths ranging from 0.9 Å to 1.3 Å. We compare the results with a small time step of $0.004\,E_\mathrm{h}^{-1}$ to a larger one of $0.1\,E_\mathrm{h}^{-1}$. Fitting total energies to the Morse potential energy curve

$$E(R) = E_0 + D(1 - e^{-a(R-R_0)})^2\,, \tag{5.37}$$

determines the equilibrium bond length R_0, the dissociation energy D, and the parameter a controlling the width of the potential.

Figure 5.7 shows both ph-AFQMC and the reference CCSD(T) potential energy curves. The absolute CCSD(T) and small time step ph-AFQMC energies agree very well, however, the large time step ph-AFQMC energies are shifted by 10 mE_h–14 mE_h (inset in Fig 5.7). The slight increase of the ph-AFQMC time-step errors with increasing bond length may result from the deteriorating quality of the trial RHF wave function. Nevertheless, the observed change in time-step errors is not large enough to compromise the accuracy of the predicted bond length; the predicted bond lengths listed in Table 5.3 are nearly identical and align well with the experimental value within statistical accuracy. Using large-time step ph-AFQMC reduces the computational time for each calculation by a factor of $\tau_L/\tau_S = 25$.

5.7 Conclusion

We implemented modifications of the ph-AFQMC algorithm in the QMCFort code to reduce the size-consistency errors at large time steps. The modifications are mainly related to the control of rare events and the weight update procedure. Addressing size-consistency errors is crucial as they have a consequential impact on the accuracy of binding energies. Using the CH_4-H_2O dimer (Fig. 5.2) and chains of infinitely separated N_2 molecules (Fig. 5.3) we showed that the modified approach markedly diminishes size-consistency errors across all time steps. Revisiting results of Lee *et al.*[39], we could identify hybrid energy capping as the primary source of size-consistency errors.

Employing large time steps required better control of the errors in the matrix exponentiation of the one-body operators. Utilizing a diverse set of 22 different systems using Dunning's cc-pVDZ and cc-pVTZ basis sets, we demonstrated that the common sixth-order Taylor expansion may prove insufficient. Larger time steps require on average up to 10–12 $\hat{\mathcal{H}}|\Psi\rangle$ operations for adequate accuracy. In contrast, Krylov methods— particularly a blocked variant —are more robust, with negligible time-step errors while employing merely 4 $\hat{\mathcal{H}}|\Psi\rangle$ operations even for large time steps. The block-Krylov method is also less sensitive to system and basis set choice than the Taylor expansion. Moreover, it introduces negligible computational overhead, especially for larger systems, making it a promising alternative.

While all AFQMC propagators yield consistent results for small time steps, we have shown that the Split-2 propagator is the optimal propagator within the AFQMC formalism, with the leading error term dictated by the Hubbard-Stratonovich transformation. We demonstrated that reliable time-step extrapolation is possible for all propagators via a second-order polynomial fit. Notably, the Split-1 and Crank-Nicolson propagators exhibit significant linear time-step errors compared to the Taylor and Split-2 propagators that are dominated by quadratic errors. For the HEAT set molecules, using a Split-2 propagator reduced the computational cost by an order of magnitude while retaining almost the same accuracy (mean absolute error of 0.31 mE_h) as the small time-step reference. For water clusters, the time-step extrapolated binding energies at the heavy-augmented double-zeta basis set agree well with those obtained by small time-step calculations. Similarly, the complete basis-set time-step extrapolated binding energies are in excellent agreement with the reference CCSD(T) values (root-mean-square error of 0.08 kcal/mol).

Finally, we showed that certain observables, such as the equilibration bond length, are much less sensitive to time-step errors than total energies. Using the N_2 dimer

as an example, we demonstrated that the ph-AFQMC calculation with $\tau = 0.1\,E_{\mathrm{h}}^{-1}$ yields the same bond length as a calculation with $\tau = 0.002\,E_{\mathrm{h}}^{-1}$, while reducing the computational cost by a factor of 25.

In conclusion, we highlighted the ability to employ larger time steps in ph-AFQMC, resulting in an order of magnitude speedup compared to standard ph-AFQMC calculations. We plan to validate the efficacy of large time-step ph-AFQMC on a wider range of systems where accurate small time-step computations are very expensive.

Chapter 6

Self-Refinement of Auxiliary-Field Quantum Monte Carlo via Non-Orthogonal Configuration Interaction

This chapter is based on:

Self-Refinement of Auxiliary-Field Quantum Monte Carlo via Non-Orthogonal Configuration Interaction
Zoran Sukurma, Martin Schlipf, Georg Kresse

submitted to: Journal of Chemical Theory and Computation (January, 2025)
arXiv: https://arxiv.org/abs/2403.02542

Section 6.2 is partially moved to the Chapter 3.

Author Contribution: conceptualization of the project, analytic derivations, software development, numerical calculations, data acquisition, data analysis, drafting of the initial manuscript, manuscript editing and proofreading (together with coauthors).

For optimal accuracy, auxiliary-field quantum Monte Carlo (AFQMC) requires trial states consisting of multiple Slater determinants. We develop an efficient algorithm to select the determinants from an AFQMC random walk, eliminating the need for other methods. When determinants contribute significantly to the non-orthogonal configuration interaction energy, we include them in the trial state. These refined trial wave functions significantly reduce the phaseless bias and sampling variance of the local energy estimator. With 100 to 200 determinants, we lower the error of AFQMC by up to a factor of 10 for second-row elements that are not accurately described with a Hartree-Fock trial wave function. For the HEAT set, we improve the average error to within chemical accuracy. For benzene, the largest system studied, we reduce AFQMC error by 80% with 214 Slater determinants and find a 10-fold increase of the time to solution. We show that the remaining error of the method prevails in systems with static correlation or strong spin contamination.

6.1 Introduction

Accurate large-scale applications of the post-Hartree-Fock methods have become feasible with advances in computing power.[82,83,198] Coupled-cluster singles, doubles, and perturbative triples (CCSD(T))[146,147] and fixed-node diffusion Monte Carlo (FN-DMC)[80,89,91] are two of the most prominent methods, offering an excellent balance between accuracy and computational cost. However, recent studies[82,83] indicate increasing discrepancies between the two methods for large non-covalent complexes. For example, the discrepancy for a C_{60} buckyball inside a [6]-cycloparaphenyleneacetylene ring (132 atoms) amounts to 7.6 kcal/mol after ruling out all stochastic uncertainties. Such large discrepancies lead to mistrust in both methods, especially as each is considered highly reliable for predicting non-covalent interaction energies. Schäfer *et al.*[198] pointed out that CCSD(T) may not be sufficiently accurate and that correcting the perturbative triples[199] improves interaction energies at the cost of less accurate total energies.

Auxiliary-field quantum Monte Carlo (AFQMC)[8,133,200] has emerged as a promising alternative to CCSD(T), gaining increasing popularity in recent years.[23,28–31,33,37–39,41,42,44,52,131] Several key factors contribute to the growing popularity of AFQMC: (i) its formulation in second quantization, enabling straightforward application on top of the mean-field methods, (ii) its favorable computational scaling—$\mathcal{O}(N^4)$ for AFQMC compared to $\mathcal{O}(N^7)$ for CCSD(T), and (iii) its demonstrated accuracy. In its simplest formulation with a single-determinant trial wave function, AFQMC accuracy typically falls between that of CCSD and CCSD(T).[33,39,41,44] The main source of error in AFQMC is the phaseless approximation[8,41,100,133,190] introduced to control the fermionic phase problem. Additionally, AFQMC requires many steps to reduce the sampling variance leading to a large prefactor of the quartic scaling. Together, these factors continue to hinder efficient large-scale AFQMC calculations.

More accurate trial wave functions reduce the phaseless error and sampling variance and are thus a promising route toward more accurate AFQMC. Particle-hole multi-Slater determinants (PHMSD) are the most convenient choice for constructing such trial wave functions. Since the computational cost of a naive implementation scales linearly with the number of determinants, many groups have developed fast local energy evaluation methods for PHMSD trial wave functions.[46–50,52] Shee *et al.*[46] were the first to report an efficient evaluation of local energies over PHMSD trial wave functions using the Sherman-Morrison-Woodbury formula[102]. Later, Shi and Zhang[47] optimized the algorithm further, performing calculations with 10,000 determinants and achieving a 60-fold speedup compared to the naive implementation. Their algorithm scales as $\mathcal{O}(N_g N^2 N_e \tilde{N}_d)$, where N_g is the number of auxiliary fields, N is the number of orbitals, N_e is the number of electrons, and N_d is the number of determinants. The notation $\tilde{N}_d$ indicates sublinear scaling with the number of determinants. Mahajan *et al.*[48,49] applied the generalized Wick's theorem[201] to design an algorithm that scales as $\mathcal{O}(N_g N^2 N_e + N_g N_d)$. They reported calculations using 10,000 determinants with only a threefold increase in computational cost compared to the single-determinant case.[50] Configuration-interaction-singles-doubles (CISD) trial wave functions containing up to half a billion of PHMSDs represent the largest determinantal expansion used with AFQMC to date.[52]

In addition to the PHMSD wave functions, non-orthogonal multi-Slater determinants (NOMSD) provide an appealing alternative, often requiring fewer determinants

than the orthogonal case. Borda *et al.*[35] performed AFQMC calculations using up to 250 NOMSD determinants. They generated the trial wave functions using the few-determinant approach[202–204] and the resonating Hartree-Fock method.[53,205] For these wave functions, the local energy evaluation scales linearly with the number of determinants, which limits its practical application as the number of determinants grows. Alternative choices for the trial state of AFQMC simulations are general Hartree-Fock (GHF) wave functions,[12] matrix-product states,[206], and states obtained using quantum computers.[136,207–209]

In this work, we use the AFQMC method itself to generate candidate determinants for the non-orthogonal Configuration interaction (NOCI) and refine the AFQMC trial wave functions. We carefully design the selection process to achieve the most compact NOCI expansion. During each epoch of determinant selection, we perform a short AFQMC random walk and select determinants that (1) have sufficiently negative local energies, (2) exhibit a small overlap with the currently selected NOCI wave function, and (3) contribute significantly to the correlation energy. We demonstrate that the resulting method, denoted as AFQMC/NOCI, substantially reduces phaseless errors and the AFQMC sampling variance. Reducing sampling variance often offsets the additional computational cost introduced by the NOCI trial wave function. We note that the idea of self-refinement in AFQMC is not new. Qin *et al.*[210] tuned independent-electron calculations to reproduce the same density matrix as the constrained-phase AFQMC[6,7], thereby generating an optimized trial determinant for subsequent AFQMC calculations.

The remainder of the paper is structured as follows: we briefly recapitulate the AFQMC and NOCI methods and describe the selection process in detail in the next section. Then, the practical implementation details of the selection process that yields the most compact NOCI expansion are described in the section Implementation Details. We validate our approach through various applications on small molecular systems in the Result section. Finally, we summarize our work and possibilities for future developments in the Conclusion.

6.2 Theoretical Background

The section about AFQMC random walk is moved to the Chapter 3. Further, we discuss the NOCI method and the selection process in Sec. 6.2.1.

6.2.1 NOCI Selection Process

Following from Eqs. (3.1), (3.3), and (3.38), the exact ground-state wave function is approximated by an integral over random fields

$$|\Phi\rangle \approx \int \mathrm{d}^{N_g}x \, c(\mathbf{x})\hat{B}(\mathbf{x})\,|\Psi_0\rangle\,, \tag{6.1}$$

where $c(\mathbf{x})$ is an unknown amplitude function representing $|\Phi\rangle$, and $\hat{B}(\mathbf{x})\,|\Psi_0\rangle$ denotes non-orthogonal Slater determinants for different $\mathbf{x}$ vectors. Here, $|\Psi_0\rangle$ is a reference determinant, usually a Hartree-Fock wave function. This approximation would become an equality if $\hat{B}(\mathbf{x}^1)\hat{B}(\mathbf{x}^2) = \hat{B}(\mathbf{x}^1 + \mathbf{x}^2)$. The discretized form of the previous equation

serves as the basis for the NOCI expansion

$$|\Phi_{N_\mathrm{d}}\rangle = \sum_{\alpha}^{N_\mathrm{d}} c_\alpha \hat{B}(\mathbf{x}^\alpha)\,|\Psi_0\rangle = \sum_{\alpha}^{N_\mathrm{d}} c_\alpha\,|\Psi_\alpha\rangle\,. \tag{6.2}$$

The selection process extracts N_d Slater determinants $|\Psi_\alpha\rangle$ from the AFQMC random walk and determines the optimal coefficients c_α solving the NOCI equation

$$\sum_\beta H_{\alpha\beta} c_\beta = E \sum_\beta S_{\alpha\beta} c_\beta, \tag{6.3}$$

where E is an upper bound to the true ground state energy E_0. The Hamiltonian and the overlap matrix elements

$$H_{\alpha\beta} = \langle\Psi_\alpha|\hat{H}|\Psi_\beta\rangle\,, \qquad\qquad S_{\alpha\beta} = \langle\Psi_\alpha|\Psi_\beta\rangle\,, \tag{6.4}$$

are computed using the non-orthogonal Wick theorem,[98] similar to Eq. (3.34).

We divide the selection process into three stages: (1) preselection based on AFQMC local energies, (2) a metric test, and (3) an energy test, both typically employed in NOCI.[211,212]

AFQMC Preselection

AFQMC walkers with low negative local energies tend to have large weights, small overlap with the trial wave function $|\Psi_\mathrm{T}\rangle$, and significant contribution to the total AFQMC energy (Eq. 3.32). This makes them suitable candidates for inclusion in the NOCI expansion. For a given ensemble of walkers in $|\Phi_k\rangle$ defined in Eq. (3.3), we calculate the mean local energy

$$\bar{E}_\mathrm{L} = \frac{1}{N_w} \sum_w E_\mathrm{L}(\Psi_w) \tag{6.5}$$

and the standard deviation

$$\sigma^2_{E_\mathrm{L}} = \frac{1}{N_w - 1} \sum_w \big(E_\mathrm{L}(\Psi_w) - \bar{E}_\mathrm{L}\big)^2. \tag{6.6}$$

Walkers with local energies satisfying

$$E_\mathrm{L}(\Psi_w) \leq \bar{E}_\mathrm{L} - \lambda\,\sigma_{E_\mathrm{L}} \tag{6.7}$$

are advanced to the further NOCI selection. λ is a numeric parameter that needs to be adjusted to obtain an optimized trial state. This step requires only local energy information, making it computationally simpler than the subsequent two tests.

Metric Test

We define the projection operator

$$\hat{Q} = 1 - \sum_{\alpha,\beta=1}^{N_d} |\Psi_\alpha\rangle\, S^{-1}_{\alpha\beta}\, \langle\Psi_\beta| \tag{6.8}$$

that projects the candidate determinant $|\Psi\rangle$ on the space orthogonal to the space spanned by N_d determinants in $|\Phi_{N_\mathrm{d}}\rangle$. We note that the projection operator $\hat{Q}$ is Hermitian $\hat{Q}^\dagger = \hat{Q}$ and idempotent $\hat{Q}^2 = \hat{Q}$. The projection $\hat{Q}|\Psi\rangle$ is not a single Slater determinant and can be interpreted as a residual vector to the space spanned by determinants in $|\Phi_{N_\mathrm{d}}\rangle$. We define a metric threshold μ and require

$$\sqrt{\frac{\langle\Psi|\hat{Q}|\Psi\rangle}{\langle\Psi|\Psi\rangle}} \geq \mu. \tag{6.9}$$

This constraint effectively eliminates linear dependencies between Slater determinants in $|\Phi_{N_d}\rangle$ and prevents the NOCI overlap matrix $S_{\alpha\beta}$ from becoming singular.

Energy Test

The energy test measures the contribution of the candidate determinant $|\Psi\rangle$ to the total energy of $|\Phi_{N_\mathrm{d}}\rangle$. We could compute the exact contribution with the NOCI equation (6.3), but solving it for every candidate determinant is computationally too expensive. Instead, we determine coefficients of a smaller variational problem with only two degrees of freedom

$$|\Phi_{N_\mathrm{d}+1}\rangle = \tilde{c}_1 |\Phi_{N_\mathrm{d}}\rangle + \tilde{c}_2 \hat{Q}|\Psi\rangle \tag{6.10}$$

by solving

$$\begin{pmatrix} \langle\Phi_{N_\mathrm{d}}|\hat{H}|\Phi_{N_\mathrm{d}}\rangle & \langle\Phi_{N_\mathrm{d}}|\hat{H}\hat{Q}|\Psi\rangle \\ \langle\Psi|\hat{Q}\hat{H}|\Phi_{N_\mathrm{d}}\rangle & \langle\Psi|\hat{Q}\hat{H}\hat{Q}|\Psi\rangle \end{pmatrix} \begin{pmatrix} \tilde{c}_1 \\ \tilde{c}_2 \end{pmatrix} = \tilde{E} \begin{pmatrix} \langle\Phi_{N_\mathrm{d}}|\Phi_{N_\mathrm{d}}\rangle\, \tilde{c}_1 \\ \langle\Psi|\hat{Q}|\Psi\rangle\, \tilde{c}_2 \end{pmatrix}. \tag{6.11}$$

The variational energy $\tilde{E}$ is the approximation of the full variational energy, and it is sufficiently accurate for the selection process. A candidate determinant $|\Psi\rangle$ passes the energy test if

$$\frac{E - \tilde{E}}{|E|} > \varepsilon \tag{6.12}$$

for an energy threshold ε.

If a candidate determinant $|\Psi\rangle$ meets all three criteria, it is added to the NOCI expansion, and the NOCI equation (6.3) is solved again to update the coefficients c_α.

6.3 Implementation Details

In this section, we study the impact of all parameters on the efficiency of the optimized NOCI selection algorithm. We benchmark the algorithm on the O_2 molecule using the cc-pVDZ basis set and frozen-core approximation, a representative system for which AFQMC/HF performs poorly.[41]

Inspired by Chen *et al.*,[213] we constrain the AFQMC random walk during the NOCI selection process to the first 100 Cholesky vectors for all systems considered in this work. This is achieved by setting $\hat{L}_g = 0$ for $g > 100$ in Eq. (3.12). While not essential, this constraint accelerates the selection process and produces more compact NOCI wave functions.

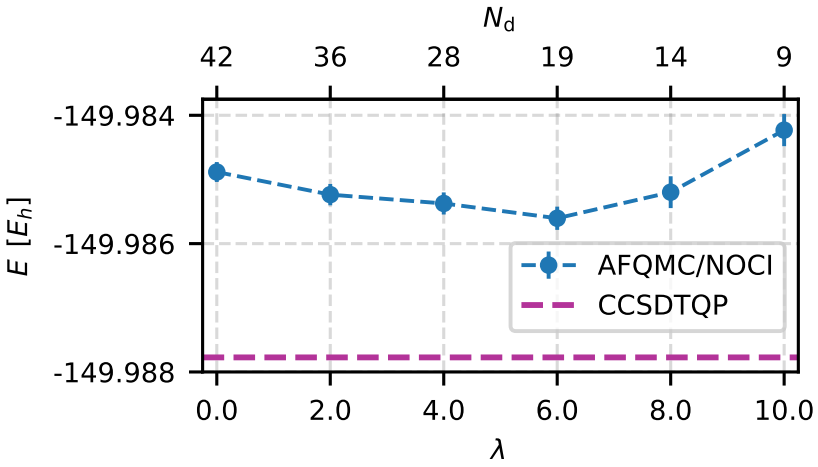

Figure 6.1: AFQMC/NOCI energy (blue dots) does not depend strongly on the preselection parameter λ, with the deviation from the reference CCSDTQP energy (magenta line) being nearly constant. Small λ values increase the number of determinants N_d, whereas large values yield a larger sample variance. We select $\lambda = 4.0$ as a balanced choice between accuracy and efficiency. The system under consideration is O_2 in the cc-pVDZ basis set. Other selection parameters are chosen as specified in Table 6.1, with $\varepsilon_{\text{min}} = 10^{-5}$.

We optimize the trial wave function over N_ξ epochs. From one epoch to the next, we systematically decrease the energy threshold ε

$$\varepsilon_\xi = \varepsilon_{\text{max}} \left(\frac{\varepsilon_{\text{min}}}{\varepsilon_{\text{max}}} \right)^{(\xi-1)/(N_\xi-1)} \tag{6.13}$$

for $\xi = 1, 2, \ldots, N_\xi$. As a consequence, we add only determinants with a large impact on the energy in early epochs. In later epochs, where the trial wave function is already more accurate, we also add determinants with a smaller impact on the energy. In each epoch, we must provide a sufficiently large number of candidate determinants for the energy test to ensure convergence of the selection process with respect to the current energy threshold ε_ξ. We use a fixed number of walkers $N_w = 6,400$ and $N_k = 100$ time steps of length $\tau = 0.05\, E_{\text{h}}^{-1}$. This ensures convergence for all reasonable choices of λ and μ. After each time step, we update the NOCI wave function with determinants that meet all three criteria given in the section NOCI Selection Process. At the end of the epoch, we update the trial wave function for the next one.

The parameters λ for the preselection and μ for the metric test are constant across all epochs because they have a smaller impact on the accuracy of the method. Let us consider λ first. Fig. 6.1 shows the AFQMC energy with a NOCI trial wave function (AFQMC/NOCI energy) as a function of the parameter λ for otherwise fixed parameters. Small λ values increase the number of determinants without significant improvement of the energy. Conversely, large λ values are overly restrictive and may compromise selection accuracy. We find that any $\lambda \in [2.0, 6.0]$ leads to a balanced and converged selection. We choose $\lambda = 4.0$ because it consistently selects up to one percent of the walkers as candidates.

Next, we consider the dependence of the AFQMC/NOCI energy on the parameter μ (Fig. 6.2). For a wide range of values, μ has little impact on the number of

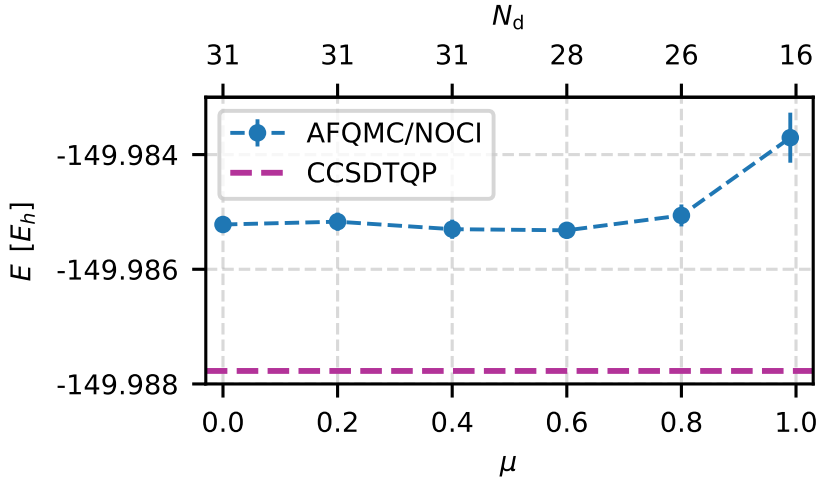

Figure 6.2: AFQMC/NOCI energy (blue dots) converges rapidly as the metric parameter μ decreases. The number of determinants N_d remains nearly constant as long as μ is not too large. We use $\mu = 0.6$ throughout this work. The system under consideration is O_2 in the cc-pVDZ basis set. Other selection parameters are chosen as specified in Table 6.1, with $\varepsilon_{\text{min}} = 10^{-5}$.

Table 6.1: List of optimal NOCI selection parameter values used throughout this work, unless stated otherwise. The ε_{min} parameter is the only remaining adjustable parameter that determines the accuracy of the NOCI selection.

N_w	N_k	τ	λ	μ	ε_{max}	N_ξ
6 400	100	$0.05E_h^{-1}$	4.0	0.6	$\geq 10^{-4}$	10

determinants and the AFQMC/NOCI energy. Too large values of μ remove too many candidates, leading to a significant increase in the variance. In other systems, we also observed that small values of μ may lead to linear-dependency issues. We set $\mu = 0.6$ as a balanced compromise.

Introducing epochs to dynamically adjust the energy test increases the number of adjustable parameters of the selection process. However, as we will show, this effort is justified because the lower bound ε_{min} for the energy is the single most important convergence parameter. The upper bound ε_{max} used in the first epoch and the number of epochs N_ξ do not significantly alter the results. ε_{max} should be large enough that only a few determinants are selected in the first epoch. For all systems considered in this work, we find that $10^{-4} \leq \varepsilon_{\text{max}} \leq 4 \times 10^{-4}$ is an appropriate choice.

The number of epochs N_ξ controls the final number of determinants in $|\Psi_{N_d}\rangle$ for fixed ε_{min} and ε_{max} values. Fig. 6.3 shows the AFQMC/NOCI energy as a function of N_ξ. For a small number of epochs, ε decreases rapidly toward ε_{min} and more determinants are selected. As the number of epochs increases, the number of determinants decreases without compromising accuracy. Beyond a certain N_ξ value, the number of determinants no longer changes, while the computational cost increases linearly with N_ξ. As a reasonable compromise, we fix $N_\xi = 10$ throughout this work.

The remaining tunable parameter ε_{min} controls the accuracy of the trial wave function. For all other parameters, we use the values listed in Table 6.1. Fig. 6.4 illustrates

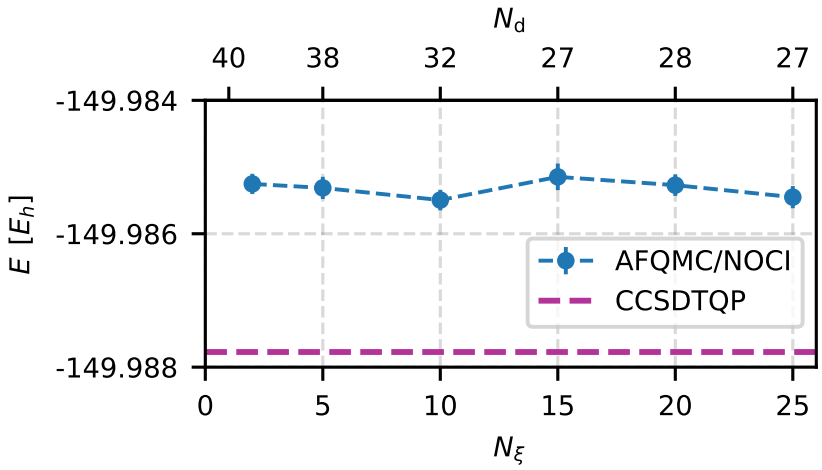

Figure 6.3: AFQMC/NOCI energy (blue dots) depends weakly on the number of epochs N_ξ for fixed ε_{min}, ε_{max} values. However, the number of determinants N_d decreases as N_ξ increases. For typical ε_{min} and ε_{max} values, we use $N_\xi = 10$ throughout this work. The system under consideration is O_2 in the cc-pVDZ basis set. Other selection parameters are chosen as specified in Table 6.1, with $\varepsilon_{\text{min}} = 10^{-5}$.

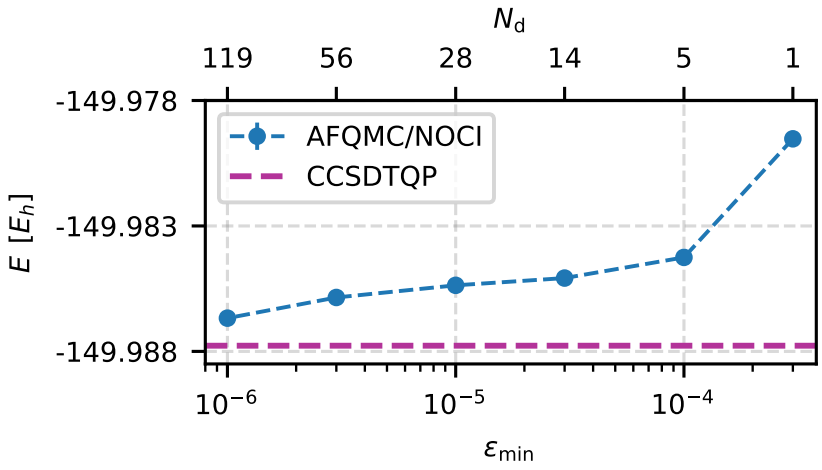

Figure 6.4: AFQMC/NOCI energy (blue dots) converges toward the reference CCSDTQP energy (magenta line) as ε_{min} decreases. Simultaneously, the number of determinants N_d increases with decreasing ε_{min}. The system under consideration is O_2 in the cc-pVDZ basis set. Other selection parameters are chosen as specified in Table 6.1.

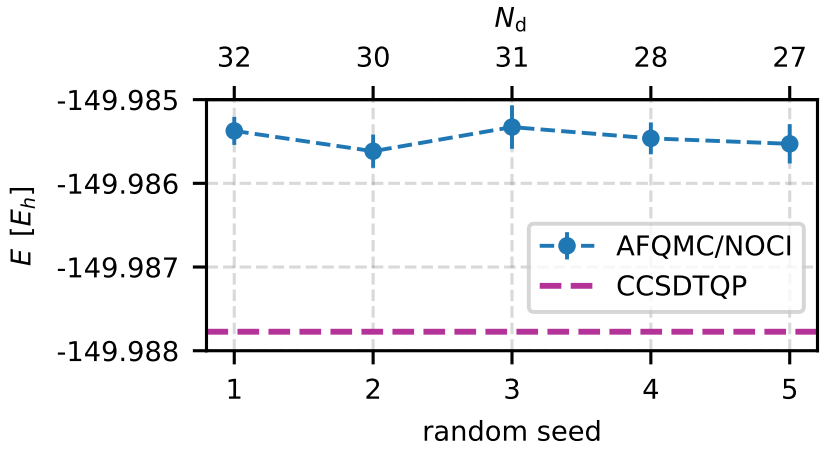

Figure 6.5: AFQMC/NOCI energy does not depend on the randomness of the NOCI selection process. Similarly, the number of determinants N_d remains nearly constant across all five random seeds used to initialize the AFQMC random walk. The system under consideration is O_2 in the cc-pVDZ basis set. Other selection parameters are chosen as specified in Table 6.1, with $\varepsilon_{min} = 10^{-5}$.

the systematic convergence of the AFQMC/NOCI result to the reference value as ε_{min} decreases. At $\varepsilon_{min} = 10^{-6}$, the trial wave function contains 119 determinants, reduces the error by 7.1 mE_h, and agrees with the reference value within chemical accuracy.

Finally, we demonstrate that the randomness of selecting the trial wave function does not impact its accuracy. We perform five identical selections with $\varepsilon_{min} = 10^{-5}$, each using a different random seed. Fig. 6.5 shows the AFQMC energies and their corresponding standard deviations for each random seed. The AFQMC energies are consistent within statistical errors, and the standard deviations remain nearly identical across all random seeds. Although the final number of determinants in the trial wave function varies slightly, as indicated on the top x-axis of Fig. 6.5, this variation does not affect the accuracy or efficiency of the AFQMC simulation.

To demonstrate the transferability of the selection parameters listed in Table 6.1, we perform a similar analysis to that presented in Figures 6.1–6.5 for three additional systems: CN, N_2 with equilibrium bond length R_0, and N_2 stretched to $2R_0$, as illustrated in Fig. S1 of the Supporting Information. These results demonstrate that the choice of parameters is transferable and that the single parameter ε_{min} primarily governs the accuracy of the trial state as well as the number of determinants.

6.4 Results and Discussion

In this section, we report AFQMC results using NOCI trial wave functions for the following cases: (i) second-row atoms, where the Hartree-Fock (HF) trial wave function performs poorly, (ii) HEAT set molecules,[41,45,120] (iii) the benzene molecule[142]—a system with a dominant dynamic correlation, and (iv) the N_2 dissociation as an example of strong static correlation effects.

We conduct all HF, NOCI, and AFQMC calculations using the QMCFort code[41] with the cc-pVDZ basis set and the frozen-core approximation. For open-shell systems,

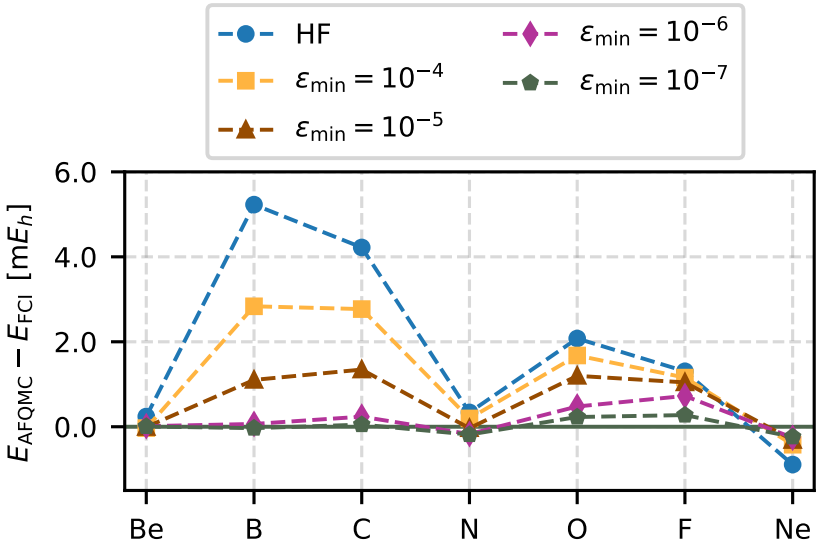

Figure 6.6: For second-row atoms, AFQMC/NOCI energies converge from AFQMC/HF toward the exact FCI energies as one tightens $\varepsilon_{\min}$. Calculations are performed using the cc-pVDZ basis set and frozen-core approximation.

we use the UHF (unrestricted HF) ground state in both NOCI selection and AFQMC calculations unless explicitly stated otherwise. The numerical parameters of the NOCI selection were described in detail in the previous section. We use modified Cholesky decomposition[64–66] with a threshold of 10^{-6} to represent ERIs. Our large time-step algorithm[54] enables a time step of $0.02\,E_{\mathrm{h}}^{-1}$ without residual time-step errors. All AFQMC calculations employ 6,400 walkers and run until the statistical error is below $0.2\,\mathrm{m}E_{\mathrm{h}}$. Consequently, the figures showing AFQMC energies have no visible error bars. On the other hand, free-projection AFQMC calculations are performed using 64,000 walkers and 5,000 time steps, with a time step of $\tau = 0.005\,E_{\mathrm{h}}^{-1}$. All AFQMC values are provided in Tables S1-S4 of the Supporting Information.

6.4.1 2nd Row Atoms

While CCSD(T) energies for second-row isolated atoms are nearly exact, AFQMC with a HF trial wave function (AFQMC/HF) exhibits unexpectedly large errors.[35,41] Therefore, single-determinant AFQMC could only predict quantities that do not involve the atomic energies of these elements. Consequently, these systems provide an ideal starting point for assessing the quality of the AFQMC using NOCI trial wave functions. We exclude the Li atom for which HF theory is already exact in the frozen-core approximation.

Fig. 6.6 depicts atomic AFQMC energies relative to FCI energies for the HF trial determinant and NOCI trial wave functions at several $\varepsilon_{\min}$ values. The AFQMC energies systematically converge toward the FCI values as $\varepsilon_{\min}$ decreases. The root-mean-square deviation (RMSD) reduces from $2.7\,\mathrm{m}E_{\mathrm{h}}$ for the HF trial wave function to within chemical accuracy for the NOCI trial wave function at $\varepsilon_{\min} = 10^{-5}$. At this threshold, the NOCI selection yields an average of 25 Slater determinants. Tighter thresholds of $\varepsilon_{\min} = 10^{-6}$ or $\varepsilon_{\min} = 10^{-7}$ reduce the error to $0.4\,\mathrm{m}E_{\mathrm{h}}$ and $0.2\,\mathrm{m}E_{\mathrm{h}}$ with

Table 6.2: Statistics for second-row elements for AFQMC/HF and AFQMC/NOCI at various ε_{min} values with the cc-pVDZ basis set and frozen-core approximation. Root-mean-square deviation (RMSD), mean absolute deviation (MAD), and maximal absolute deviation $\max(|\Delta E|)$ are presented in E_h units. $\langle N_\text{d} \rangle$ is the average number of determinants for each ε_{min} value and $\max(N_\text{d})$ is the maximum number of determinants across all atoms for a given ε_{min} value.

ε_{min}	RMSD	MAD	$\max(\lvert\Delta E\rvert)$	$\langle N_\text{d} \rangle$	$\max(N_\text{d})$
HF	2.7	2.0	5.2	1	1
10^{-4}	1.7	1.3	2.8	5	9
10^{-5}	0.9	0.7	1.3	25	34
10^{-6}	0.4	0.3	0.7	82	111
10^{-7}	0.2	0.1	0.3	129	179

Table 6.3: Statistics for HEAT set molecules for AFQMC/HF and AFQMC/NOCI at various ε_{min} values, with the cc-pVDZ basis set and frozen-core approximation. Root-mean-square deviation (RMSD), mean absolute deviation (MAD), and maximal absolute deviation $\max(|\Delta E|)$ are presented in E_h units. $\langle N_\text{d} \rangle$ is the average number of determinants for each ε_{min} value and $\max(N_\text{d})$ represents the maximum number of determinants across all HEAT molecules for a given ε_{min} value.

ε_{min}	RMSD	MAD	$\max(\lvert\Delta E\rvert)$	$\langle N_\text{d} \rangle$	$\max(N_\text{d})$
HF	2.8	1.7	8.5	1	1
10^{-4}	1.7	1.3	4.8	6	30
10^{-5}	1.5	1.1	3.9	35	59
10^{-6}	1.1	0.7	3.2	194	324

an average of 82 and 129 Slater determinants, respectively. More detailed statistics are provided in Table 6.2.

6.4.2 HEAT Set

The HEAT dataset[45,120] serves as a reliable benchmark for testing state-of-the-art correlation-consistent methods. We compare nearly exact CCSDTQP energies to AFQMC/HF, AFQMC/NOCI, and CCSD(T) ones. Although the largest system in the HEAT set (CO_2 molecule) consists of 16 electrons in 39 orbitals, both CCSD(T) and AFQMC/HF have a relatively high RMSD of 1.7 mE_h and 2.9 mE_h, respectively. This could be attributed to the fact that 14 systems are open-shell molecules, which are generally more challenging for quantum chemistry methods.

We calculate AFQMC/HF and AFQMC/NOCI energies at three different ε_{min} values. Fig. 6.7 illustrates the errors in AFQMC/HF and AFQMC/NOCI energies at different ε_{min} values relative to the CCSDTQP values. The RMSD decreases from 2.8 mE_h for AFQMC/HF to 1.5 mE_h at $\varepsilon_{\text{min}} = 10^{-5}$, and further to 1.1 m$E_\text{h}$ at $\varepsilon_{\text{min}} = 10^{-6}$. The average number of determinants in these calculations is 35 and 194, respectively. It is noteworthy that the residual errors are mainly associated with open-shell molecules. To demonstrate this, we calculate the RMSD for a subset of closed-shell HEAT molecules. For AFQMC/NOCI at $\varepsilon_{\text{min}} = 10^{-6}$, the RMSD is reduced to 0.7 mE_h compared to 2.3 mE_h for AFQMC/HF. More detailed statistics are

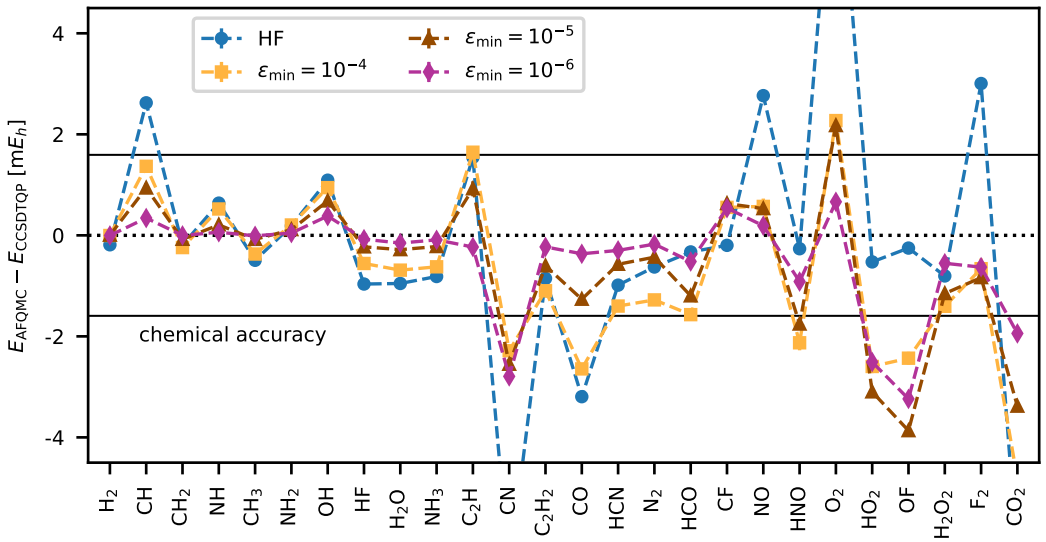

Figure 6.7: For HEAT set molecules, AFQMC/NOCI energies converge toward the CCSDTQP values as we tighten $\varepsilon_{\min}$. The RMSD decreases from 2.8 mE_h for AFQMC/HF to 1.1 mE_h for AFQMC/NOCI at $\varepsilon_{\min} = 10^{-6}$. Calculations are performed using the cc-pVDZ basis set and frozen-core approximation.

given in Table 6.3.

We take a closer look at the molecules for which AFQMC/NOCI exhibits unexpected behavior. Specifically, we examine six molecules: CN, HCO, CF, HNO, HO_2, and OF. In these cases, AFQMC/NOCI either underperforms compared to AFQMC/HF, or its performance deteriorates as the energy threshold $\varepsilon_{\min}$ decreases. Notably, five of these molecules are open-shell radicals, while only HNO is a closed-shell molecule. While HNO, like the isoelectronic O_2, exhibits an open-shell ground state at the Hartree-Fock level, for post-Hartree-Fock methods, the closed-shell Hartree-Fock determinant is generally the preferred starting point.

We begin by investigating the difference between AFQMC energies using restricted HF (RHF) and unrestricted HF (UHF) trial wave functions. The AFQMC/RHF and AFQMC/UHF differ significantly only for the CN molecule, the only system in the HEAT set exhibiting strong spin contamination. For all other systems, RHF and UHF wave functions are of similar quality, with the UHF energies being only a few mE_h lower than the RHF values. Consequently, AFQMC/RHF and AFQMC/UHF yield a similar mean absolute deviation (MAD) of 1.3 and 1.4 mE_h, respectively.

Next, we examine NOCI trial wave functions generated from RHF and UHF reference, denoted as RNOCI and UNOCI, respectively. In Fig. 6.8, we see that AFQMC/RNOCI to AFQMC/UNOCI have larger deviations than the single Slater-determinant alternative. This leads to a larger MAD of 2.1 mE_h for AFQMC/RNOCI and 3.6 mE_h for AFQMC/UNOCI. The difference between AFQMC/RNOCI and AFQMC/UNOCI originates mostly from the CN molecule, for which AFQMC/RNOCI is much closer to the reference energy. For this reason, the RNOCI trial wave function was used for CN in Fig. 6.7.

To analyze the origin of these errors, we compare these results to free-projection AFQMC (fp-AFQMC) with UHF and UNOCI trial wave functions (see Fig. 6.9). For these fp-AFQMC calculations, we employed the spin-projected AFQMC technique,[214]

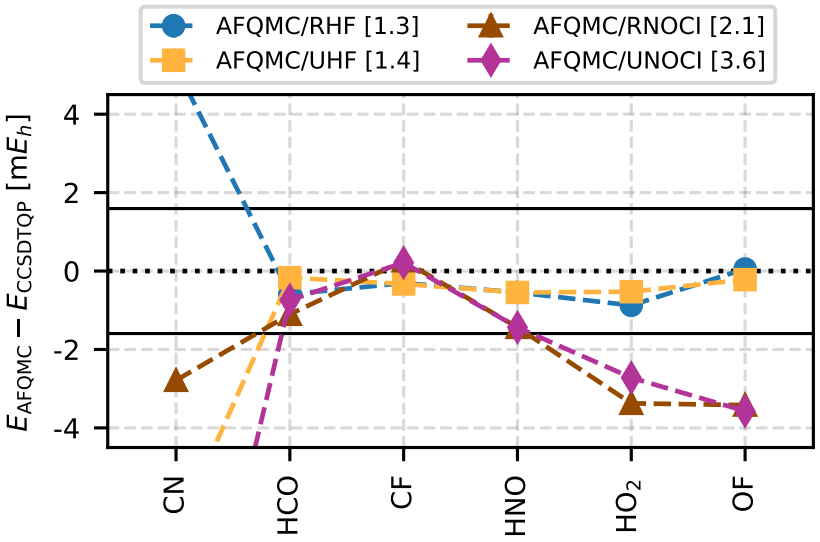

Figure 6.8: Restricted and unrestricted trial wave functions, both HF and NOCI, yield similar AFQMC energies for five out of six selected outliers from the HEAT set. The exception is the CN molecule, where the UHF wave function exhibits strong spin contamination and significantly deviates from the RHF wave function. As a result, AFQMC energies differ significantly between RHF and UHF, as well as between RNOCI and UNOCI trial wave functions. The numbers in square brackets represent the mean absolute deviation (MAD) of each method across the six selected HEAT molecules.

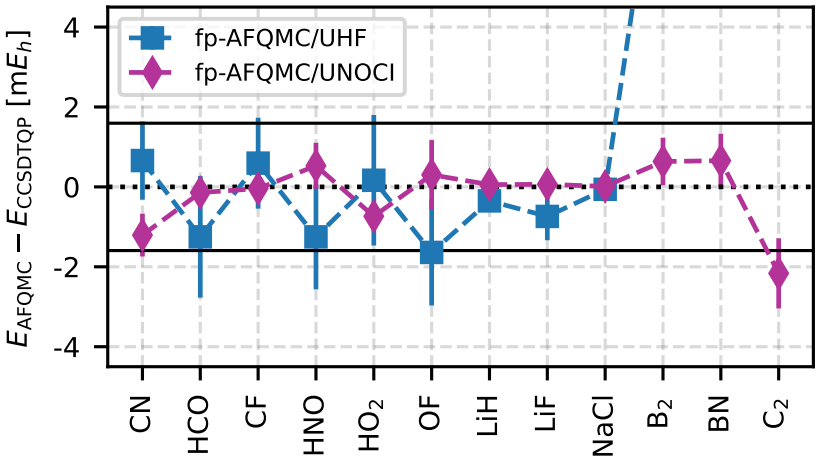

Figure 6.9: Free-projection (fp)-AFQMC using UHF and UNOCI trial wave functions yields more accurate energies than the corresponding ph-AFQMC calculations. However, the large statistical errors observed for UHF trial wave functions due to the phase problem highlight the advantage of UNOCI trial wave functions. Moreover, for strongly correlated systems such as B_2, BN and C_2, we were unable to obtain accurate fp-AFQMC/UHF energies, while fp-AFQMC/UNOCI yields both small systematic and statistical errors.

which combines UHF or UNOCI trial wave functions with an RHF walker population. While this method does not affect the final AFQMC energy as long as the system is properly equilibrated, it significantly reduces the AFQMC equilibration time. As a result, it mitigates the onset of the phase problem, which is crucial for accumulating enough samples to estimate fp-AFQMC energies.

For the six outliers of the HEAT dataset, fp-AFQMC/UHF yields an MAD of $0.9(6)\,\mathrm{m}E_\mathrm{h}$, sligthly lower than that of AFQMC/UHF. However, the phase problem of the fp-AFQMC method leads to large error bars. In contrast, fp-AFQMC/UNOCI achieves a lower MAD of $0.5(2)\,\mathrm{m}E_\mathrm{h}$, more than seven times smaller than the corresponding AFQMC/UNOCI value. The better trial state seems to reduce the phase problem, leading to much smaller statistical errors. To further support this claim, we include six additional systems in Fig. 6.9: three G1 molecules with strong ionic character (LiH, LiF, NaCl), for which Morales *et al.*[35] observed slow convergence with respect to the number of non-orthogonal Slater determinants, and three strongly correlated W4-MR molecules (B_2, BN, C_2), for which Mahajan *et al.*[52] reported the largest errors using AFQMC/CISD. For the first three molecules, both fp-AFQMC/UHF and fp-AFQMC/UNOCI yield almost exact energies with well-controlled statistical errors. In contrast, for the strongly correlated W4-MR molecules, only fp-AFMQC/UNOCI gives accurate results (within chemical accuracy), while fp-AFQMC/UHF even fails to properly equilibrate due to the onset of a severe phase problem. This again illustrates the advantage of the NOCI trial wave functions.

To summarize, these results demonstrate that the phaseless approximation is responsible for the large AFQMC/UNOCI errors. Notably, a higher quality trial wave function does not necessarily lead to smaller phaseless errors. Due to the ad hoc nature of the phaseless approximation, quantifying the dependence of the phaseless errors on the underlying trial wave function remains challenging. Our findings suggest that open-shell systems and strong spin contamination tend to exhibit larger AFQMC/NOCI errors compared to AFQMC/HF. Motivated by these observations, we investigate the dissociation of the N_2 molecule.

6.4.3 N_2 Dissociation

The dissociation of the N_2 molecule is a well-known example of strong static correlation effects caused by the breaking of the triple bond. The system also undergoes a symmetry-breaking transition, with a molecular-like RHF ground state at equilibrium geometry and an atomic-like UHF ground state at stretched geometries. The latter exhibits strong spin contamination and poses a significant challenge for AFQMC/NOCI.

We compute AFQMC total energies at six different bond lengths R, ranging from the equilibrium bond length of $2.118\,a_0$ to $4.2\,a_0$. We report AFQMC results for three trial wave functions: (i) the UHF determinant, denoted as AFQMC/UHF; (ii) the UNOCI wave function selected through the AFQMC random walk, denoted as AFQMC/UNOCI; and (iii) a special NOCI wave function obtained by diagonalizing only the RHF and two UHF determinants, denoted as AFQMC/RHF-UHF. Two UHF determinants are constructed by swapping the spin-up and spin-down orbitals. This trial wave function is motivated by the observation that both molecular and atomic-like solutions contribute significantly to the ground state near bond dissociation.

Fig. 6.10 shows the errors in our various AFQMC energies, CCSD(T) energies, and recently published AFQMC/CISD energies.[52] The reference values are highly accurate

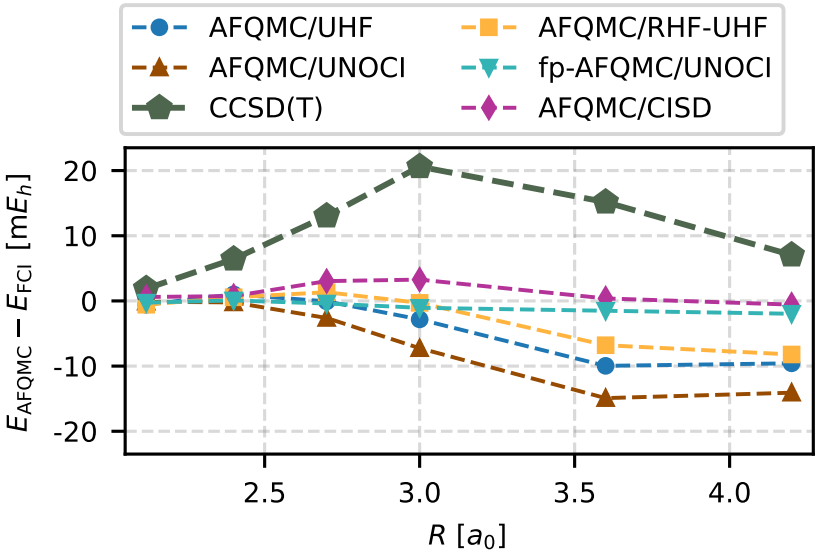

Figure 6.10: CCSD(T) energies and AFQMC energies with different trial wave functions, shown relative to the FCI energies. AFQMC/UNOCI performs worse than AFQMC/UHF for UHF trial wave functions with strong spin contamination. AFQMC/RHF-UHF yields nearly exact energies at intermediate bond lengths, where CCSD(T) and AFQMC/UNOCI exhibit the largest errors. Exact FCI energies are taken from Ref.[215], and AFQMC/CISD energies are taken from Ref.[52]. All calculations are performed using the cc-pVDZ basis set and the frozen-core approximation.

DMRG energies taken from Ref.[215]. CCSD(T) performs poorly with a maximal error of 20.6 mE_h. In contrast, AFQMC/CISD achieves good accuracy, with a maximal error of approximately 4.0 mE_h.

Our AFQMC/UHF energies agree well with those published in Ref.[52], yielding a maximal error of 10.0 mE_h. Unfortunately, our AFQMC/UNOCI results are even less reliable than AFQMC/UHF, with an error of 14.6 mE_h. We calculate fp-AFQMC/UNOCI energies to assess whether this mismatch is due to inappropriate UNOCI trial wave functions or phaseless errors. The maximal error of 2.0 mE_h demonstrates the quality of the UNOCI wave functions. This supports our hypothesis that AFQMC/UNOCI can exhibit phaseless errors larger than AFQMC/UHF for systems with strong spin contamination. In these simulations, we used RHF walkers to reduce the equilibration time, which allowed us to keep the statistical errors below 0.6 mE_h for all bond lengths. In contrast, we were unable to obtain meaningful fp-AFQMC results using UHF trial wave functions due to the severe phase problem.

In addition, AFQMC/RHF-UHF achieves nearly exact results at $R = 2.7\ a_0$ and $R = 3.0\ a_0$, which lie in the strongly correlated regime. Consequently, both CCSD(T) and AFQMC/CISD exhibit their largest errors at these bond lengths. This is an advantage of the AFQMC method, where compact trial wave functions, straightforwardly constructed using chemical intuition, outperform more sophisticated approaches that rely on the brute-force inclusion of determinants. However, AFQMC/RHF-UHF still fails at larger bond lengths, where the CI coefficient of the RHF determinant practically drops to zero. As a result of these large errors at stretched geometries, AFQMC/RHF-UHF produces errors up to 8.2 mE_h.

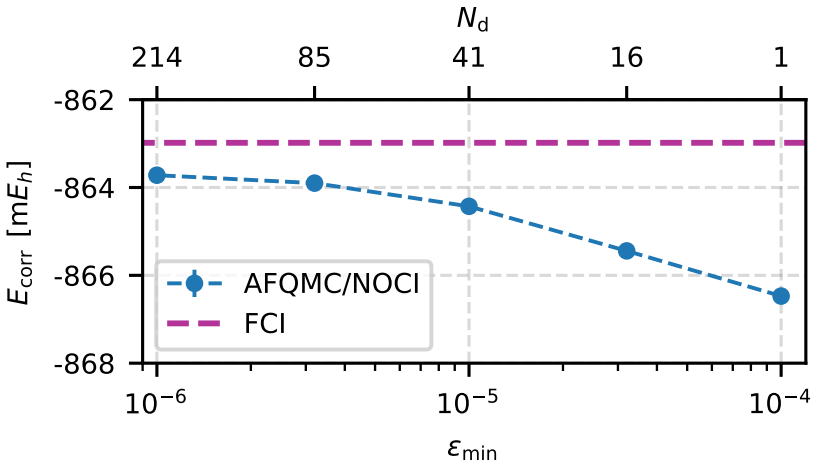

Figure 6.11: The correlation energy of benzene converges smoothly to the FCI value as ε_{min} decreases. Similarly, the number of determinants N_{d} increases with decreasing ε_{min}, achieving chemical accuracy with only 41 Slater determinants. Calculations are performed using the cc-pVDZ basis set and frozen-core approximation.

6.4.4 Benzene Molecule

The ground state of benzene, a singlet closed-shell configuration without near-degeneracies, is accurately represented by the Hartree-Fock determinant. However, the magnitude of the correlation energy is relatively large, amounting to $-863\,\text{m}E_{\text{h}}$ in the double-zeta basis set.[142] Although the total correlation energy is dominated by dynamic correlation, both CCSD(T) and AFQMC/RHF exhibit notable errors. Specifically, CCSD(T) undercorrelates by $3.6\,\text{m}E_{\text{h}}$, while AFQMC/RHF overcorrelates by $3.2\,\text{m}E_{\text{h}}$.[41] This makes benzene an excellent system to demonstrate the capabilities of post-Hartree-Fock quantum chemistry methods.

We compute the benzene molecule with 30 electrons in 108 orbitals and compare AFQMC/NOCI to AFQMC/HF. Fig. 6.11 illustrates that the AFQMC/NOCI correlation energy converges smoothly toward the FCI limit with tighter thresholds ε_{min}. At $\varepsilon_{\text{min}} = 10^{-5}$ (41 Slater determinants), the method reaches chemical accuracy with an error of $1.4\,\text{m}E_{\text{h}}$. This error is reduced further to $0.7\,\text{m}E_{\text{h}}$ at $\varepsilon_{\text{min}} = 10^{-6}$, where the trial wave function contains 214 determinants.

Next, we compare our AFQMC energies with the previously published AFQMC values. Lee *et al.*[37] reported AFQMC/RHF energies that agree with our AFQMC/RHF values within statistical error bars. They also performed AFQMC calculations using a CAS(6,6) trial wave function, where the full CAS expansion of 400 Slater determinants was truncated by discarding determinants with CI coefficients smaller than 10^{-6}, resulting in 87 significant determinants.

Fig. 6.12 summarizes these results and demonstrates that both CAS and NOCI trial wave functions effectively reduce the phaseless error. We find that the AFQMC/NOCI trial wave function with 41 determinants ($\varepsilon_{\text{min}} = 10^{-5}$) achieves an accuracy comparable to the CAS(6,6) trial wave function with 87 determinants. Increasing the number of NOCI determinants to 214, by tightening the energy threshold to $\varepsilon_{\text{min}} = 10^{-6}$, further reduces the phaseless error and yields the most accurate AFQMC energy for the benzene molecule reported to date.

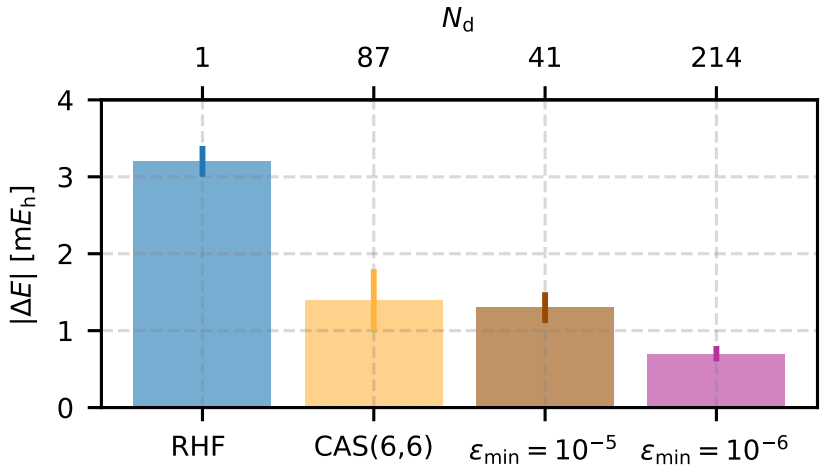

Figure 6.12: NOCI and CAS(6,6) trial wave functions effectively reduce the phaseless bias for the benzene molecule compared to the RHF trial wave function. Despite using fewer determinants, the AFQMC/NOCI trial wave function with $\varepsilon_{\text{min}} = 10^{-5}$ (41 Slater determinants) achieves an accuracy similar to AFQMC/CAS(6,6), which includes 87 significant determinants in the CAS expansion. Lowering the energy threshold to $\varepsilon_{\text{min}} = 10^{-6}$ results in the most accurate AFQMC energy for benzene reported to date.

6.5 Performance and Scaling Analysis of AFQMC/NOCI

In this section, we systematically benchmark the accuracy and performance of the AFQMC/NOCI method. We begin by analyzing the size-consistency of AFQMC/NOCI energies, followed by the analysis of the time-step errors. Finally, we investigate the computational cost scaling of AFQMC/NOCI with respect to the number of determinants in the trial wave function and determine conditions under which AFQMC/NOCI becomes a more efficient alternative to conventional AFQMC/HF.

6.5.1 Size-Consistency

An important property of any quantum chemistry method is size-consistency. A method is size-consistent if the total energy of two non-interacting fragments A and B equals the sum of their individual energies, i.e., $E(A+B) = E(A) + E(B)$. This property ensures that the method correctly describes systems in the dissociation limit. This is essential for accurately predicting binding and reaction energies.

While exact full configuration interaction (FCI) is guaranteed to be size-consistent, several approximate methods, such as Hartree-Fock and coupled-cluster theory, also satisfy this requirement. Lee *et al.*[39] proved that AFQMC/HF is size-consistent in the limit of vanishing time steps. We have recently shown that AFQMC/HF retains size-consistency for large time steps, provided that rare events are carefully controlled.[54]

In contrast, truncated CI methods are generally not size-consistent. This includes the NOCI approach we used throughout this work to refine AFQMC trial wave functions. Therefore, we investigate whether the size inconsistency of the NOCI method taints the size consistency of the AFQMC/NOCI. To this end, we examine non-interacting chains of N_2 molecules in the cc-pVDZ basis set.

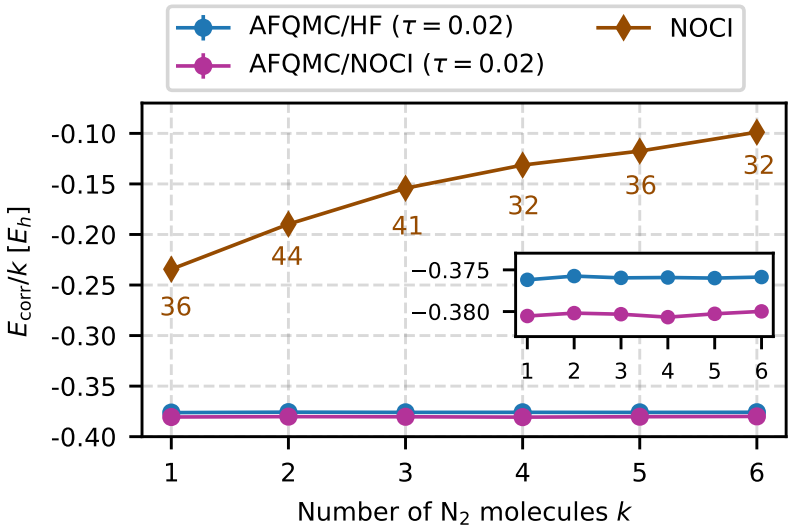

Figure 6.13: AFQMC/NOCI correlation energies (magenta line) per N_2 molecule are independent of the number of molecules k, demonstrating size-consistency, even though the underlying NOCI trial wave functions (brown line) are not. The inset provides a zoomed-in comparison between the size-consistent AFQMC/HF (blue line) and AFQMC/NOCI energies. The numbers below the brown line indicate the number of determinants in the NOCI trial wave function for each k.

Fig. 6.13 shows the correlation energy per N_2 molecule as a function of the number of molecules k in the chain. As expected, AFQMC/HF (blue line) is size-consistent. Remarkably, AFQMC/NOCI (magenta line) also yields size-consistent correlation energies, even though the NOCI trial wave functions themselves are not size-consistent (brown line). It is also noteworthy that the number of determinants in the NOCI expansions remains nearly constant across all chain lengths k.

6.5.2 Time-Step Errors

Next, we examine time-step errors of the AFQMC method by analyzing the total energies of the N_2 molecule, and binding energies of the water dimer, both in the cc-pVDZ basis set.

Fig. 6.14 shows time-step errors in the total AFQMC energy of the N_2 molecule for the HF trial wave function and AFQMC/NOCI trials at several ε_{min} values. As ε_{min} decreases, time-step errors decrease as well. For $\varepsilon_{\text{min}} = 10^{-6}$ (208 Slater determinants), time-step errors are essentially negligible for all considered time steps.

Next, Fig. 6.15 shows the binding energies of the water dimer as a function of the time step for both AFQMC/HF and AFQMC/NOCI trial wave function at $\varepsilon_{\text{min}} = 10^{-5}$ containing 37 Slater determinants for the water monomer and 36 determinants for the dimer. For small time steps, both methods yield consistent binding energies within statistical error bars. However, for larger time steps ($\tau > 0.10\, E_{\text{h}}^{-1}$), AFQMC/NOCI shows larger errors. We attribute this behavior to the NOCI selection process. Since the HF determinant is a unique choice, errors in different geometries can benefit from error cancellation. In contrast, the NOCI selection may yield different quality trial

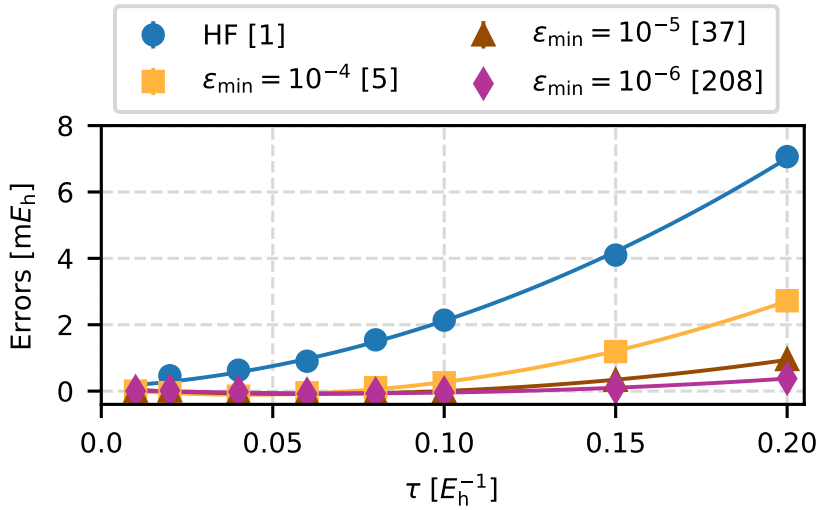

Figure 6.14: Time-step errors in the AFQMC total energy for N_2 in the cc-pVDZ basis set. Errors decrease significantly as ε_{min} tightens. For $\varepsilon_{\text{min}} = 10^{-6}$, time-step errors become negligible for all time steps up to $\tau = 0.20\,E_\text{h}^{-1}$. The numbers in square brackets indicate the number of Slater determinants in the corresponding trial wave functions.

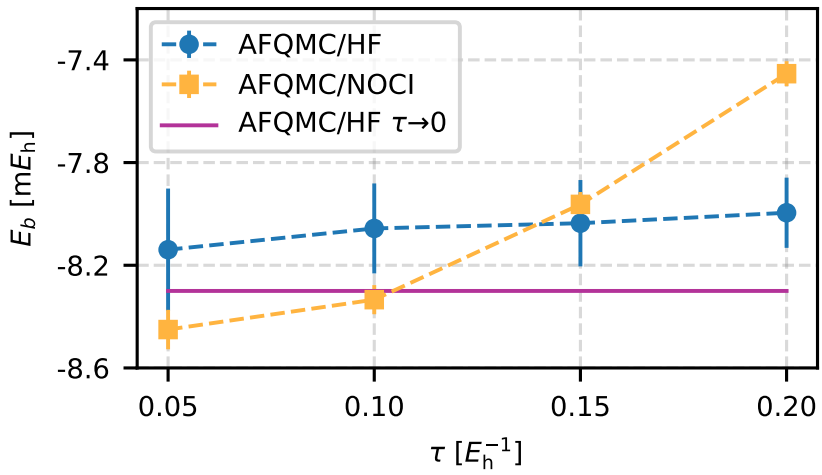

Figure 6.15: Time-step errors in AFQMC binding energies are larger for AFQMC/NOCI compared to AFQMC/HF due to the imperfect cancellation of the time-step errors between NOCI trial wave functions. For the water dimer in the cc-pVDZ basis set, AFQMC/NOCI exhibits larger time-step errors for $\tau \geq 0.10\,E_\text{h}^{-1}$. The NOCI trial wave function was generated using $\varepsilon_{\text{min}} = 10^{-5}$, yielding 37 Slater determinants for the water monomer and 36 for the dimer.

wavefunctions for different geometries which impedes this error cancellation.

In summary, improved trial wave functions reduce time-step errors in total energies, enabling the use of larger time steps in AFQMC simulations. However, for relative energies such as binding energies, AFQMC/NOCI may show larger time-step errors due to imperfect cancellation of time-step errors between different NOCI trial wave functions.

6.5.3 Computational Scaling with Number of Determinants

For a fixed number of AFQMC steps, the computational cost of AFQMC/NOCI, denoted as T_{NOCI}, scales linearly with the number of determinants N_{d} in the trial wave function, relative to the cost of AFQMC/HF T_{HF}:

$$T_{\mathrm{NOCI}}/T_{\mathrm{HF}} \sim N_{\mathrm{d}}. \tag{6.14}$$

However, it is more relevant to examine how the AFQMC/NOCI method scales with N_{d} for fixed variance. To account for this, we consider the quantity $\frac{T_{\mathrm{NOCI}}}{T_{\mathrm{HF}}}\frac{\sigma^2_{\mathrm{NOCI}}}{\sigma^2_{\mathrm{HF}}}$, where σ represents the standard deviation of the AFQMC local energies corresponding to a given trial wave function $|\Phi_{N_{\mathrm{d}}}\rangle$. For the purpose of this analysis, we use the empirically observed relationship $\sigma \approx |E_0 - E_{N_{\mathrm{d}}}|$, with supporting data in Fig. S2 of the Supporting Information. Here, E_0 is the exact ground-state energy of the system, and $E_{N_{\mathrm{d}}} = \frac{\langle\Phi_{N_{\mathrm{d}}}|\hat{H}|\Phi_{N_{\mathrm{d}}}\rangle}{\langle\Phi_{N_{\mathrm{d}}}|\Phi_{N_{\mathrm{d}}}\rangle}$ is the trial energy.

Furthermore, we assume that the correlation energy in the NOCI state converges as

$$|E_0 - E_{N_{\mathrm{d}}}| \sim |E_0 - E_{\mathrm{HF}}|\, N_{\mathrm{d}}^{-\alpha}, \tag{6.15}$$

where α is the NOCI convergence exponent. This finally leads to:

$$\frac{T_{\mathrm{NOCI}}}{T_{\mathrm{HF}}}\frac{\sigma^2_{\mathrm{NOCI}}}{\sigma^2_{\mathrm{HF}}} \sim N_{\mathrm{d}} \left(\frac{|E_0 - E_{\mathrm{HF}}|\, N_d^{-\alpha}}{|E_0 - E_{\mathrm{HF}}|}\right)^2 = N_{\mathrm{d}}^{1-2\alpha}. \tag{6.16}$$

This result suggests that the overall scaling of AFQMC/NOCI is determined by the NOCI convergence exponent α. Notably, it implies that for $\alpha > 0.5$, AFQMC/NOCI becomes more efficient than AFQMC/HF.

To verify our hypothesis, we first determine the exponent α for two representative molecules from the HEAT set, as illustrated in Fig. 6.16. Extending the analysis to 25 molecules from the HEAT set, we observe an average exponent of $\alpha = 0.46 \pm 0.14$—close to the critical value of 0.5. Similar α values are observed for N_2 at different bond lengths, indicating that the analysis is also valid for strongly correlated systems.

Finally, Fig. 6.17 illustrates the scaling behavior of the AFQMC/NOCI method on the example of the N_2 molecule, for which we estimated $\alpha = 0.34$. The blue curve shows the ratio $T_{\mathrm{NOCI}}/T_{\mathrm{HF}}$ for a fixed number of AFQMC steps, confirming the expected linear scaling with respect to N_{d}. In contrast, the magenta curve shows $T_{\mathrm{NOCI}}/T_{\mathrm{HF}}$ for a fixed statistical variance, revealing sublinear scaling $\sim N_{\mathrm{d}}^{0.3}$, which is in excellent agreement with the predicted behavior $\sim N_{\mathrm{d}}^{1-2\alpha}$, where $1 - 2\alpha = 0.32$.

6.6 Conclusion

In this work, we combined the non-orthogonal configuration interaction (NOCI) method with the phaseless auxiliary-field quantum Monte Carlo (AFQMC) random

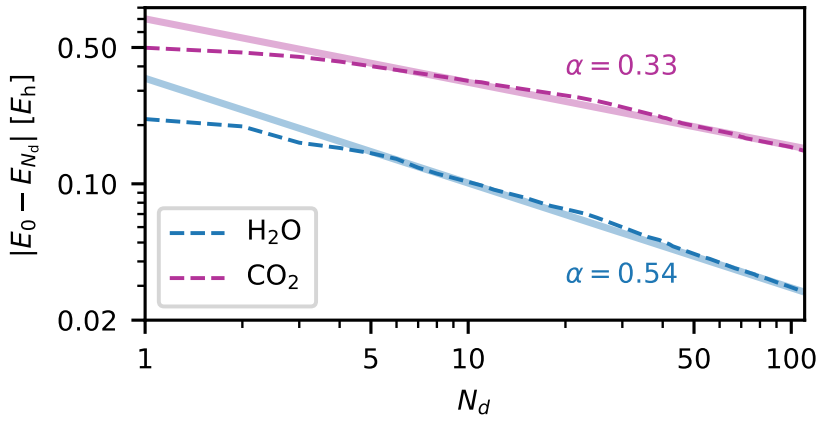

Figure 6.16: The missing correlation energy $|E_0 - E_{N_\mathrm{d}}|$ of the NOCI wave function $|\Phi_{N_\mathrm{d}}\rangle$ decreases sublinearly with the number of determinants N_d, following a power law governed by an exponent α. This exponent determines the efficiency of the AFQMC/NOCI procedure. For $\alpha \geq 0.5$, AFQMC/NOCI becomes more efficient than the conventional AFQMC/HF at fixed variance.

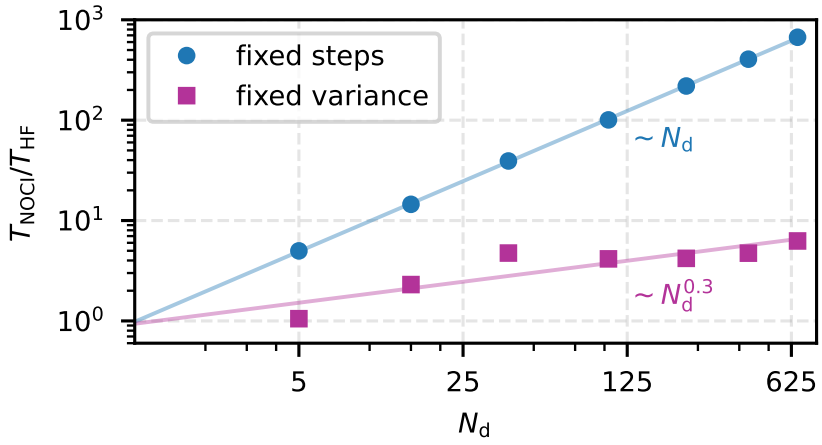

Figure 6.17: The AFQMC/NOCI wall time for a fixed number of AFQMC steps scales linearly with the number of determinants. In contrast, for a fixed variance, the scaling becomes sublinear, following a power law with an exponent of $1 - 2\alpha$, where α characterizes the convergence of the NOCI correlation energy. For the specific case of the N_2 molecule in the cc-pVDZ basis set, we observe $T_{\mathrm{NOCI}}/T_{\mathrm{HF}} \sim N_\mathrm{d}^{0.3}$. As a result, an AFQMC/NOCI simulation with 664 determinants is only eight times more expensive than the corresponding AFQMC/HF calculation.

walk to generate more accurate trial wave functions for AFQMC. We introduced an efficient selection algorithm to identify the most important AFQMC random walkers based on three criteria: (i) low local energies, (ii) small overlap with the currently sampled trial wave function, and (iii) a significant lowering of the variational energy of the trial wave function. We used the O_2 molecule, a system where AFQMC/HF performs poorly, to calibrate the algorithm. Most parameters of the selection algorithm have minimal impact on its accuracy and can be set to reasonable default values. In the end, a single adjustable parameter ε_{min} governs the accuracy and the number of determinants in the sampled trial wave function. We showed that AFQMC/NOCI systematically converges to the reference value as we tighten ε_{min}.

We demonstrated that the NOCI trial wave function improves AFQMC to achieve chemical accuracy for atoms and the HEAT set. For second-row elements, AFQMC/NOCI reduces the RMSD compared to AFQMC/HF by a factor of 10 using an average of 129 Slater determinants. Similarly, an average of 35 determinants obtained with $\varepsilon_{\text{min}} = 10^{-5}$ are sufficient to reduce the RMSD for the HEAT molecules to less than 1 kcal/mol. For the benzene molecule, we reduced the AFQMC errors by 80% with a NOCI trial wave function of 214 determinants.

In addition, we show that AFQMC/NOCI yields size-consistent energies, although the underlying trial wave functions are not strictly size-consistent. Furthermore, the NOCI wave functions significantly reduce AFQMC time-step errors. Finally, we found that the computational cost of AFQMC/NOCI scales sublinearly with the number of determinants, following a power law whose exponent α is fully determined by the convergence rate of the correlation energy recovered by the NOCI trial wave function. Notably, for exponents $\alpha > 0.5$, AFQMC/NOCI becomes more efficient than conventional AFQMC/HF, because it significantly reduces the AFQMC sampling variance.

For strongly correlated systems, phaseless errors do not always decrease smoothly with improved NOCI trial wave functions. Using the N_2 dissociation as an example, we show that AFQMC/NOCI can sometimes lead to larger errors than AFQMC/HF. The near-exact free-projection AFQMC/NOCI energies across all bond lengths suggest that the dominant source of error arises from the phaseless approximation itself. Therefore, future work should focus on improving the AFQMC/NOCI for strongly correlated systems. Two promising directions are: (i) further optimization of the NOCI trial wave functions, potentially including orbital rotations, and (ii) a systematic revision of the phaseless approximation.

However, for weakly correlated systems, our selection algorithm, based on AFQMC random walks, provides a systematic approach to refine AFQMC trial wave functions without the need for another approach to determine multi-determinantal trial wave functions. We have shown that trial states with 100-200 non-orthogonal Slater determinants achieve AFQMC energies within chemical accuracy for all weakly correlated systems analyzed in this work. This is particularly exciting for solid-state systems, where sophisticated many-body approaches are often not yet available or computationally still very expensive.

Chapter 7

Summary and Conclusion

Phaseless auxiliary-field quantum Monte Carlo (ph-AFQMC) has been gaining increasing popularity in quantum chemistry and condensed matter physics. Its broad applicability, combined with a favorable balance between accuracy, computational cost, and system size scaling, makes it an attractive alternative to existing methods. Additionally, recent discrepancies between fixed-node diffusion Monte Carlo (FN-DMC) and coupled cluster singles, doubles, and perturbative triples (CCSD(T)) for large non-covalent molecular complexes highlight the need for an additional high-accuracy reference method.

In this work, we systematically investigated the AFQMC method, addressing its accuracy, computational efficiency, and potential improvements. First, we presented a scalable FORTRAN implementation of the AFQMC code, QMCFort, optimized for peak performance on CPUs. We used QMCFort to compute ph-AFQMC energies for 26 molecules from the HEAT dataset and compared them against CCSD(T) and the more accurate CCSDTQP method, used as a reference. The observed mean absolute deviation (MAD) of 1.15 kcal/mol for AFQMC is slightly worse than that of CCSD(T) (MAD=0.87 kcal/mol). The poor performance for a few molecules (CN, CO, CO_2, O_2) accounts for a significant portion of this deviation in AFQMC. For most molecules, however, AFQMC performs comparably to or even better than CCSD(T).

A key challenge in AFQMC is the tendency to overcorrelate, a well-known issue linked to the phaseless approximation, which is introduced to control the fermionic sign problem. To address this issue, we modified the phaseless approximation, denoted as ph*-AFQMC. For molecules such as CN, CO, CO_2, C_6H_6, where overcorrelation effects are pronounced, ph*-AFQMC substantially reduces phaseless errors. While these modifications show promising results, a more extensive study is required to determine whether ph*-AFQMC consistently outperforms standard ph-AFQMC.

For optimal performance, AFQMC should use the largest possible time steps to decorrelate consecutive walkers. However, significantly smaller time steps are required to control time-step errors. To address this trade-off, we conducted a detailed investigation of AFQMC propagation, developing a robust protocol to enable large time-step AFQMC simulations while maintaining accuracy.

We first examined various propagators within the AFQMC framework and identified the second-order split propagator as the optimal choice, as the leading time-step errors are already dictated by the Hubbard-Stratonovich transformation. Furthermore, we found that the commonly used sixth-order Taylor expansion for approximating matrix exponentials lacks sufficient accuracy for large time steps. As a more robust

alternative, we demonstrated that iterative Krylov methods provide significantly improved stability, with the fifth-order Krylov expansion being exact across all time steps. Moreover, we implemented modifications to rare event control, effectively minimizing size-consistency errors in ph-AFQMC.

With these improvements, large time-step ph-AFQMC simulations became significantly more stable. In cases where residual time-step errors persisted, we demonstrated that a second-order polynomial fit provides a robust extrapolation of ph-AFQMC energies. Applying this large-time-step protocol to HEAT molecules and small water clusters, we found that accurate AFQMC results were consistently reproduced while reducing the computational cost by an order of magnitude.

Finally, to enhance AFQMC accuracy, we explored the use of non-orthogonal multi-Slater determinants (NOMSD) as trial wave functions. Unlike previous approaches, we generate NOMSD trial wave functions directly from the AFQMC random walk and optimize their linear coefficients using non-orthogonal configuration interaction (NOCI). Specifically, we developed a selection algorithm that identifies those random walkers most effective in lowering the variational energy of the trial state. The algorithm was calibrated so that a single adjustable energy parameter simultaneously controls both the accuracy of the trial state and the number of Slater determinants it contains.

Using trial wave functions with 100–200 Slater determinants, phaseless errors are significantly reduced, achieving chemical accuracy for all tested weakly-correlated systems. Specifically, we observed: (i) a 20-fold reduction in MAD for second-row atoms compared to AFQMC with a Hartree-Fock trial wave function, (ii) a 2.5-fold reduction in MAD for HEAT set molecules, surpassing CCSD(T) accuracy, and (iii) an 80% error reduction for the benzene molecule using a trial wave function with 214 determinants. However, additional refinement is needed to extend this approach to strongly correlated systems.

In summary, we systematically studied AFQMC, addressing its accuracy, computational performance, and methodological improvements with the goal of establishing it as an additional high-accuracy reference method in quantum chemistry. By developing an optimized Fortran implementation, refining propagation techniques, and introducing more accurate trial wave functions, we significantly enhanced the reliability and efficiency of AFQMC simulations. Our results demonstrate that AFQMC achieves accuracy comparable to or exceeding CCSD(T) for weakly correlated systems, while offering a computationally efficient alternative to higher-order coupled-cluster methods. With further refinements, particularly for strongly correlated systems, AFQMC has the potential to become a standard benchmark method, complementing existing quantum chemistry approaches and expanding the toolkit available for accurate many-body electronic structure calculations.

Appendix A

Notation

The notation used in this work is summarized in the following table.

Table A.1: Notation used in this work

Symbol	Meaning / Definition
N	number of basis functions
N_e	number of electrons in the system
$N_o(N_v)$	number of occupied (virtual) states
N_g	number of auxiliary fields (i.e. Cholesky vectors)
N_d	number of Slater determinants
p, q, r, s	indices that run over all basis functions
i, j, k, l	indices that run over occupied states
a, b, c, d	indices that run over virtual states
$\langle pq\|rs\rangle = V_{pqrs}$	electron repulsion integrals (ERIs) in Dirac's notation
$[pq\|rs] = \langle pr\|qs\rangle$	ERIs in chemist's notation
$L_{g,pq}$	matrix element of the Cholesky vector $\hat{L}_g$
Ψ_{pi}	$N \times N_e$ matrix representing the single Slater determinant
$\|\Psi\rangle$	single Slater determinant
$\|\Psi_0\rangle$	Hartree-Fock Slater determinant
$\|\Psi_\mathrm{T}\rangle$	single-determinantal trial wave function
$\|\Phi\rangle$	exact ground-state many-body wave function
$\|\Phi_\mathrm{T}\rangle$	multi-determinantal trial wave function
$\|\Phi_k\rangle$	AFQMC wave function at time step k
E_0	exact ground-state energy
E_k	AFQMC energy at time step k
$\bar{E}_k$	running AFQMC average energy
$\hat{c}_p^{(\dagger)}$	Annihilation (creation) operator for the basis state labeled by orbital index p
$\hat{a}_p^{(\dagger)} \equiv \hat{a}_{\psi_{p\sigma}}^{(\dagger)}$	Annihilation (creation) operator for the state $\|\psi_p\rangle$: $\hat{a}_{\psi_p}^\dagger = \sum_q \Psi_{qp}\hat{c}_q^\dagger$

Appendix B

Thouless's Theorem

After the Hubbard-Stratonovich transformation, Thouless's theorem is arguably the most important theorem that makes the auxiliary-field quantum Monte Carlo (AFQMC) method feasible and successful. Therefore, this appendix is dedicated to a comprehensive derivation of the theorem.

Thouless's theorem[94,95] states that a single Slater determinant propagated by the exponential of a one-body operator remains a single Slater determinant. This theorem is implicitly used in all quantum chemistry methods that involve orbital rotations.[59] In methods that employ the Hubbard-Stratonovich transformation, Thouless's theorem simplifies the many-body propagation to the propagation of single Slater determinants. These determinants are conveniently represented with matrices, and their propagation is efficiently evaluated using linear algebra operations.

Consider a Slater determinant

$$|\Psi\rangle = \prod_{i=1}^{N_e} \hat{a}^\dagger_{\psi_i} |0\rangle \,, \tag{B.1}$$

where the creation operators $\hat{a}^\dagger_{\psi_i}$ create an electron in the state $|\psi_i\rangle$:

$$\hat{a}^\dagger_{\psi_i} = \sum_r \Psi_{ri}\, \hat{c}^\dagger_r. \tag{B.2}$$

Here, the creation operator $\hat{c}^\dagger_r$ creates an electron in the basis states $|\varphi_r\rangle$, and the $N \times N_e$ matrix Ψ_{ri} parameterizes the Slater determinant. We also consider a general one-body operator of the form

$$\hat{A} = \sum_{pq} A_{pq}\, \hat{c}^\dagger_p \hat{c}_q, \tag{B.3}$$

where the $N \times N$ matrix A_{pq} represents the operator $\hat{A}$ in the basis $|\varphi_p\rangle$.

First, we examine the effect of the operator $\hat{A}$ on the creation operator $\hat{a}^\dagger_{\psi_i}$:

$$\begin{aligned} \hat{A}\,\hat{a}^\dagger_{\psi_i} &= \overbrace{\sum_{pq} A_{pq}\, \hat{c}^\dagger_p \hat{c}_q}^{\hat{A}} \overbrace{\sum_r \Psi_{ri}\, \hat{c}^\dagger_r}^{\hat{a}^\dagger_{\psi_i}} \\ &= \sum_{pqr} A_{pq}\, \Psi_{ri}\, \hat{c}^\dagger_p \hat{c}_q \hat{c}^\dagger_r. \end{aligned} \tag{B.4}$$

By commuting $\hat{c}_r^\dagger$ two positions to the left and using the fermionic anticommutation relations $\{c_p, c_q^\dagger\} = \delta_{pq}$ and $\{c_p^\dagger, c_q^\dagger\} = 0$, we obtain:

$$\begin{aligned}\hat{A}\,\hat{a}_{\psi_i}^\dagger &= \sum_{pqr} A_{pq}\,\Psi_{ri}\,\hat{c}_p^\dagger\left(\delta_{qr} - \hat{c}_r^\dagger\hat{c}_q\right)\\ &= \sum_{pq} A_{pq}\Psi_{qi}\,\hat{c}_p^\dagger + \sum_r \Psi_{ri}\,\hat{c}_r^\dagger \sum_{pq} A_{pq}\,\hat{c}_p^\dagger\hat{c}_q\\ &= \hat{a}_{\hat{A}\psi_i}^\dagger + \hat{a}_{\psi_i}^\dagger\hat{A}.\end{aligned} \tag{B.5}$$

To summarize this result, we act with the operator $\hat{A}$ on a single-electron state $\hat{a}_\psi^\dagger|0\rangle$:

$$\hat{A}\,\hat{a}_\psi^\dagger|0\rangle = \hat{a}_{\hat{A}\psi}^\dagger|0\rangle + \hat{a}_\psi^\dagger\hat{A}\,|0\rangle = \hat{a}_{\hat{A}\psi}^\dagger|0\rangle\,, \tag{B.6}$$

where we used the fact that

$$\hat{A}\,|0\rangle = \sum_{pq} A_{pq}\,\hat{c}_p^\dagger\hat{c}_q\,|0\rangle = 0. \tag{B.7}$$

This shows that applying the one-body operator $\hat{A}$ to a single-electron state effectively rotates the orbitals ψ into a new orbital $\hat{A}\psi$, yielding another single-electron state.

Next, we generalize the Eq. (B.5) to the case $\hat{A}^n\,\hat{a}_{\psi_i}^\dagger$. To do so, we prove the following lemma by induction:

$$\hat{A}^n\,\hat{a}_{\psi_i}^\dagger = \sum_{k=0}^{n}\binom{n}{k}\hat{a}_{\hat{A}^k\psi_i}^\dagger\hat{A}^{n-k}. \tag{B.8}$$

- **Base case:** For $n = 1$, Eq. (B.8) simplifies to Eq. (B.5), which is already proven.
- **Induction step:** Let us suppose, it is true for n. Then:

$$\begin{aligned}\hat{A}^{n+1}\,\hat{a}_{\psi_i}^\dagger &= \hat{A}\hat{A}^n\,\hat{a}_{\psi_i}^\dagger = \sum_{k=0}^{n}\binom{n}{k}\hat{A}\,\hat{a}_{\hat{A}^k\psi_i}^\dagger\hat{A}^{n-k}\\ &= \sum_{k=0}^{n}\binom{n}{k}\left[\hat{a}_{\hat{A}^k\psi_i}^\dagger\hat{A} + \hat{a}_{\hat{A}^{k+1}\psi_i}^\dagger\right]\hat{A}^{n-k}\\ &= \sum_{k=0}^{n}\binom{n}{k}\hat{a}_{\hat{A}^k\psi_i}^\dagger\hat{A}^{n-k+1} + \sum_{k=0}^{n}\binom{n}{k}\hat{a}_{\hat{A}^{k+1}\psi_i}^\dagger\hat{A}^{n-k}\\ &= \hat{a}_{\psi_i}^\dagger\hat{A}^{n+1} + \sum_{k=1}^{n}\binom{n}{k}\hat{a}_{\hat{A}^k\psi_i}^\dagger\hat{A}^{n-k+1} + \sum_{k=0}^{n-1}\binom{n}{k}\hat{a}_{\hat{A}^{k+1}\psi_i}^\dagger\hat{A}^{n-k} + \hat{a}_{\hat{A}^{n+1}\psi_i}^\dagger\\ &= \hat{a}_{\psi_i}^\dagger\hat{A}^m + \sum_{k=1}^{m-1}\binom{m-1}{k}\hat{a}_{\hat{A}^k\psi_i}^\dagger\hat{A}^{m-k} + \sum_{k=1}^{m-1}\binom{m-1}{k-1}\hat{a}_{\hat{A}^k\psi_i}^\dagger\hat{A}^{m-k} + \hat{a}_{\hat{A}^m\psi_i}^\dagger\\ &= \hat{a}_{\psi_i}^\dagger\hat{A}^m + \sum_{k=1}^{m-1}\left[\binom{m-1}{k} + \binom{m-1}{k-1}\right]\hat{a}_{\hat{A}^k\psi_i}^\dagger\hat{A}^{m-k} + \hat{a}_{\hat{A}^m\psi_i}^\dagger\\ &= \hat{a}_{\psi_i}^\dagger\hat{A}^m + \sum_{k=1}^{m-1}\binom{m}{k}\hat{a}_{\hat{A}^k\psi_i}^\dagger\hat{A}^{m-k} + \hat{a}_{\hat{A}^m\psi_i}^\dagger\\ &= \sum_{k=0}^{m}\binom{m}{k}\hat{A}\,\hat{a}_{\hat{A}^k\psi_i}^\dagger\hat{A}^{m-k}\\ &= \sum_{k=0}^{n+1}\binom{n+1}{k}\hat{A}\,\hat{a}_{\hat{A}^k\psi_i}^\dagger\hat{A}^{n+1-k},\end{aligned} \tag{B.9}$$

where we use recursion relation $\binom{n-1}{k} + \binom{n-1}{k-1} = \binom{n}{k}$ as well as the change of variable $m = n+1$ to make the derivation more transparent.

- **Conclusion:** By induction, Eq. (B.8) applies for all $n \geq 0$.

We now consider the action of the exponential operator $e^{\hat{A}}$ on the creation operator $\hat{a}^\dagger_{\psi_i}$:

$$\begin{aligned} e^{\hat{A}}\, \hat{a}^\dagger_{\psi_i} &= \sum_{n=0}^{\infty} \frac{1}{n!} \hat{A}^n\, \hat{a}^\dagger_{\psi_i} = \\ &= \sum_{n=0}^{\infty} \sum_{k=0}^{n} \binom{n}{k} \frac{1}{n!}\, \hat{a}^\dagger_{A^k \psi_i} \hat{A}^{n-k} = \sum_{n=0}^{\infty} \sum_{k=0}^{n} \frac{\hat{a}^\dagger_{A^k \psi_i}}{k!} \frac{\hat{A}^{n-k}}{(n-k)!} \\ &= \left(\sum_{n=0}^{\infty} \frac{\hat{a}^\dagger_{A^n \psi_i}}{n!} \right) \left(\sum_{n=0}^{\infty} \frac{\hat{A}^n}{n!} \right) \\ &= \hat{a}^\dagger_{e^A \psi_i}\, e^{\hat{A}}, \end{aligned} \tag{B.10}$$

where we used Taylor expansion to expand the exponential function and the Cauchy product rule.

The final result is obtained by applying the exponential operator $e^{\hat{A}}$ to the Slater determinant $|\Psi\rangle$ and utilizing the result derived above:

$$\begin{aligned} e^{\hat{A}}\, |\Psi\rangle &= e^{\hat{A}}\, \hat{a}^\dagger_{\psi_N} \cdots \hat{a}^\dagger_{\psi_2} \hat{a}^\dagger_{\psi_1}\, |0\rangle \\ &= \hat{a}^\dagger_{e^A \psi_N} e^{\hat{A}} \cdots \hat{a}^\dagger_{\psi_2} \hat{a}^\dagger_{\psi_1}\, |0\rangle \\ &= \hat{a}^\dagger_{e^A \psi_N} \cdots \hat{a}^\dagger_{e^A \psi_2} e^{\hat{A}}\, \hat{a}^\dagger_{\psi_1}\, |0\rangle \\ &= \hat{a}^\dagger_{e^A \psi_N} \cdots \hat{a}^\dagger_{e^A \psi_2} \hat{a}^\dagger_{e^A \psi_1} e^{\hat{A}}\, |0\rangle \\ &= \hat{a}^\dagger_{e^A \psi_N} \cdots \hat{a}^\dagger_{e^A \psi_2} \hat{a}^\dagger_{e^A \psi_1}\, |0\rangle = |\Psi'\rangle\,, \end{aligned} \tag{B.11}$$

where we used $e^{\hat{A}}\, |0\rangle = (1 + \hat{A} + \cdots)\, |0\rangle = |0\rangle$. It is evident that the wave function $|\Psi'\rangle$ remains a single Slater determinant. If the initial Slater determinant is parameterized by the matrix Ψ, then the resulting Slater determinant is parameterized by the matrix

$$\Psi' = e^A\, \Psi. \tag{B.12}$$

In summary, Thouless's theorem can be expressed as follows:

$$|\Psi'\rangle = e^{\hat{A}}\, |\Psi\rangle \quad \rightarrow \quad \Psi' = e^A \Psi, \tag{B.13}$$

where we distinguish between the one-body propagator $e^{\hat{A}}$ on the left-hand side and the simple matrix exponential e^A on the right-hand side.

Appendix C

Monte Carlo Integration

Monte Carlo methods are a class of numerical techniques that use random numbers to solve deterministic problems. The most common application of Monte Carlo methods is the evaluation of definite integrals of the form

$$\mathbb{E}_p[f] = \int_\chi p(x) f(x)\,\mathrm{d}x, \tag{C.1}$$

where the integral is interpreted as the expectation value of $f(x)$ with respect to the probability density $p(x)$. The probability density satisfies the normalization condition

$$\int_\chi p(x)\,\mathrm{d}x = 1. \tag{C.2}$$

In its simplest form, direct sampling Monte Carlo, we draw random samples $x_1, x_2, \ldots x_N$ from the distribution $p(x)$ and estimate the integral in Eq. (C.1) as

$$\bar{f} = \frac{1}{N}\sum_i^N f(x_i). \tag{C.3}$$

The *strong law of large numbers*[216] guarantees that the estimator $\bar{f}$ approaches $\mathbb{E}_p[f]$ in the limit of an infinite number of samples, i.e.

$$\lim_{N\to\infty} \bar{f} = \lim_{N\to\infty} \frac{1}{N}\sum_i^N f(x_i) = \mathbb{E}_p[f]. \tag{C.4}$$

Since the method is stochastic, every observed result $\bar{f}$ comes with an uncertainty $\sigma_{\bar{f}}$, which depends on the underlying variance

$$\begin{aligned}
\sigma_f^2 = \mathrm{Var}_p[f] &= \int_\chi p(x)\big(f(x) - \mathbb{E}_p[f]\big)^2\,\mathrm{d}x \\
&= \int_\chi p(x) f^2(x)\,\mathrm{d}x - \Big(\int_\chi p(x) f(x)\mathrm{d}x\Big)^2 \\
&= \mathbb{E}_p[f^2] - \mathbb{E}_p[f]^2,
\end{aligned} \tag{C.5}$$

as

$$\sigma_{\bar{f}} = \frac{\sigma_f}{\sqrt{N}}. \tag{C.6}$$

The variance σ_f^2 can be computed analytically only for simple functions, where the Monte Carlo method is unnecessary. For all interesting examples, the variance is estimated using the finite sample $x_1, x_2, \ldots x_N$ as

$$\sigma_f^2 \approx \frac{1}{N-1} \sum_i^N \big(f(x_i) - \bar{f}\big)^2. \tag{C.7}$$

As a consequence of the *central limit theorem*,[216] the estimator $\bar{f}$ is normally distributed around the expectation value $\mathbb{E}_p[f]$ with the variance $\sigma_{\bar{f}}^2$, i.e.

$$\frac{\bar{f} - \mathbb{E}_p[f]}{\sigma_{\bar{f}}} \sim \mathcal{N}(0,1). \tag{C.8}$$

In other words, this result defines the following confidence intervals

$$P(\bar{f} - 1\sigma_{\bar{f}} < \mathbb{E}_p[f] < \bar{f} + 1\sigma_{\bar{f}}) \approx 0.68, \tag{C.9}$$
$$P(\bar{f} - 2\sigma_{\bar{f}} < \mathbb{E}_p[f] < \bar{f} + 2\sigma_{\bar{f}}) \approx 0.95, \tag{C.10}$$
$$P(\bar{f} - 3\sigma_{\bar{f}} < \mathbb{E}_p[f] < \bar{f} + 3\sigma_{\bar{f}}) \approx 0.997, \tag{C.11}$$

which are known as "one-sigma", "two-sigma", and "three-sigma" rules.

Finally, we compare Monte Carlo integration with conventional quadrature methods. In quadrature methods, we usually have a spacing h that depends on the total number of grid points N and the dimensionality of the system d as $h \propto N^{-1/d}$. The integration error per integration cell of volume h^d behaves as $\mathcal{O}(h^{d+2})$, i.e. $\mathcal{O}(N^{-1-2/d})$ for most quadrature methods. The total integration error for N cells behaves as $\mathcal{O}(N^{-2/d})$, showing that the accuracy of quadrature methods decreases with increasing dimensionality of the integration space. This phenomenon is known as the *curse of dimensionality*.

On the other hand, the accuracy of Monte Carlo integration behaves as $\mathcal{O}(N^{-1/2})$, independent of d. A direct comparison of integration errors reveals that Monte Carlo integration becomes more efficient than quadrature methods for $d \geq 4$. Although this estimate depends on specific technical details and the particular quadrature method used, the key takeaway is that as the dimensionality increases, Monte Carlo integration becomes the method of choice.

Appendix D

Importance Sampling

Importance sampling, also commonly known as a reweighting technique, relies on the following transformation of Eq. (C.1)

$$\mathbb{E}_p[f(x)] = \int_\chi p(x)f(x)\,\mathrm{d}x = \int_\chi q(x)f(x)\frac{p(x)}{q(x)}\,\mathrm{d}x = \mathbb{E}_q\left[f(x)\frac{p(x)}{q(x)}\right], \tag{D.1}$$

where $p(x)$ is the target distribution and $q(x)$ is the proposal distribution. Sampling $x_1, x_2, \ldots, x_N$ form the proposal distribution $q(x)$ and defining importance sampling weights

$$R(x_i) = \frac{p(x_i)}{q(x_i)} \tag{D.2}$$

leads to the importance-sampled estimator of $\mathbb{E}_p[f]$:

$$\bar{f}_p = \frac{1}{N}\sum_i f(x_i)R(x_i). \tag{D.3}$$

Alternatively, we can use a weighted estimator

$$\bar{f}_p = \frac{\sum_i f(x_i)R(x_i)}{\sum_i R(x_i)}, \tag{D.4}$$

which typically introduces a small bias but also reduces the sampling variance.

For more efficient sampling, the proposal distribution $q(x)$ should have the following properties:

Approximating target distribution: $q(x) \approx p(x)$, as this ensures that frequently sampled points from $q(x)$ are also significant for the integral over $p(x)$.

Heavy Tails: $q(x)$ should have heavier tails than $p(x)$ to ensure well-behaved importance weights $R(x) = p(x)/q(x) < 1$.

Support Compatibility: $q(x) \neq 0\ \forall x \in \chi : p(x) \neq 0$. This guarantees that the weight function $R(x)$ is well-defined throughout the entire integration domain χ.

Variance of the Importance-Sampled Estimator

The variance of the importance-sampled estimator is given by

$$\begin{aligned}\mathrm{Var}_q\left[f(x)\frac{p(x)}{q(x)}\right] &= \int_\chi \mathrm{d}x\, q(x)\,\frac{f^2(x)p^2(x)}{q^2(x)} - \left(\int_\chi q(x)\frac{f(x)p(x)}{q(x)}\right)^2 \\ &= \mathbb{E}_q\left[\frac{f^2(x)p^2(x)}{q^2(x)}\right] - \mathbb{E}_p[f(x)]^2.\end{aligned} \tag{D.5}$$

It can be proven that the proposal distribution

$$q^*(x) = \frac{p(x)|f(x)|}{\int_\chi p(x)|f(x)|\,\mathrm{d}x} \tag{D.6}$$

minimizes the variance, i.e. the expectation $\mathbb{E}_q[f^2p^2/q^2]$.[217] However, this result is only of theoretical value, as it requires knowledge of $\mathbb{E}_p[f]$, which is precisely what we aim to estimate using the Monte Carlo method. Nevertheless, the result is still useful because it provides insight into the ideal form of $q^*(x)$. Substituting the optimal proposal $q^*(x)$ into the importance-sampled integral $\mathbb{E}_q[fp/q]$ simplifies it to $\mathbb{E}_q[f/|f|]$, revealing that the variance is minimized for the proposal distribution that makes the integrand nearly constant.

Application of Importance Sampling

Importance sampling proves to be useful in various scenarios, including

Variance Reduction: A well-chosen proposal distribution $q(x)$ decreases the sampling variance of the importance-sampled estimator (Eq. D.3) compared to the naive estimator (Eq. C.1).

Unknown Target Distibution: When direct sampling from the target distribution $p(x)$ is not feasible, we use a proposal distribution $q(x)$ that approximates $p(x)$, and from which we know how to sample. The original integral is then efficiently evaluated using the importance-sampled estimator.

Multiple Target Distributions: Importance sampling allows simultaneous evaluation of integrals over multiple target distributions $p_j(x)$ for $j = 1,2,\ldots,n$ using a single set of samples $x_1,x_2,\ldots,x_N \sim q(x)$. If the proposal distribution reasonably represents all target distributions, the weights $R_j(x_i) = p_j(x_i)/q(x_i)$ can be used to estimate integrals over multiple target distributions. For this reason, importance sampling is often called a reweighting technique.

Rare Event Sampling: For rare events, direct sampling from the target distribution is typically inefficient. A carefully chosen proposal distribution can enhance the frequency of rare events.

Appendix E

Statistical Data Analysis in Auxiliary-Field Quantum Monte Carlo

AFQMC simulations generate a set of weights W_{kw} and local energies $E_{kw} = E_{\mathrm{L}}(\Psi_{kw})$. These data are neither statistically independent nor identically distributed. Therefore, this appendix outlines a robust procedure for calculating average values and corresponding error bars of AFQMC energies. Without loss of generality, we assume that these quantities are real-valued, as is typical for ph-AFQMC.

The first step is to average weights and energies over all walkers at each time step

$$w_k = \frac{1}{N_w} \sum_w W_{kw} \qquad\qquad E_k = \frac{\sum_w W_{kw} E_{kw}}{\sum_w W_{kw}}, \tag{E.1}$$

where N_w is the number of walkers in the simulation.

Equilibration Phase

Like all projector quantum Monte Carlo methods, AFQMC simulation begins with sampling from the trial distribution $|\Phi_{\mathrm{T}}\rangle$. The system then rapidly relaxes to the equilibrium distribution $|\Phi\rangle$, as illustrated in Fig. E.1. This initial stage of the AFQMC simulation is known as the equilibration phase.

The number of equilibration steps N_{eq} depends on the observable being measured, the trial distribution $|\Phi_{\mathrm{T}}\rangle$, and system-specific characteristics such as the fundamental gap. N_{eq} is conveniently determined by plotting E_k as a function of k, as shown in Fig. E.1. The equilibration phase ends when E_k stabilizes and begins to fluctuate around its average value. Based on the plot, we estimate $N_{\mathrm{eq}} = 2500$.

Since data from the equilibration phase are not identically distributed and are strongly biased toward the trial distribution, they are excluded from statistical analysis.

Sampling Phase: Average Values and Error Bars

The remaining N steps constitute the sampling phase of the AFQMC simulation, during which the samples are assumed to be identically distributed. The weighted average

$$\bar{E} = \frac{\sum_k w_k E_k}{\sum_k w_k} \tag{E.2}$$

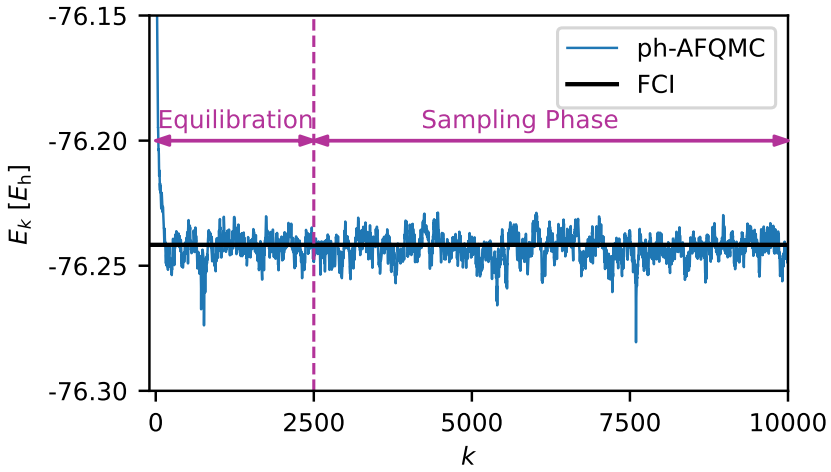

Figure E.1: During the equilibration phase, the AFQMC energy relaxes from the trial energy E_T toward the ground-state energy E_0. The sampling phase begins once the energy stabilizes and oscillates around a fixed value. Samples from the equilibration phase are not used for estimating the averages.

is in principle an unbiased estimator of the ground state energy.

Estimating error bars, however, is more complicated. The first challenge is the necessity of using weighted expressions for the standard deviation

$$\sigma_{\bar{E}}^2 = \frac{\sum_k w_k (E_k - \bar{E})^2}{v_1 - \frac{v_2}{v_1}}, \tag{E.3}$$

and the standard deviation of the mean

$$\sigma_{\bar{E}} = \frac{\sigma_E}{\sqrt{\frac{v_1^2}{v_2}}}. \tag{E.4}$$

Here, the p-th moments of the weights are defined as $v_p = \sum_k w_k^p$, and the factors $v_1 - v_2/v_1$ and v_1^2/v_2 are the weighted equivalents of the factors $N-1$ and N, respectively, used in the corresponding unweighted expressions.

A more significant complication is that the estimator $\sigma_{\bar{E}}$ defined above systematically underestimates the true standard deviation. This underestimation arises from correlations in the data, a direct consequence of PQMC methods, where the propagated state explicitly depends on the current state. To correct for this, the estimator must be adjusted as

$$\sigma_{\bar{E}} = \frac{\sigma_E}{\sqrt{\frac{v_1^2}{v_2}}} \sqrt{\kappa}, \tag{E.5}$$

where κ is the correlation length, representing the number of steps after which two samples, $w_k E_k$ and $w_{k+\kappa} E_{k+\kappa}$, become statistically independent. In the following, we outline two standard methods for estimating error bars of the correlated data. Note that all expressions for unweighted data are recovered by setting $w_k = 1$.

Autocorrelation Coefficients

The correlation length can be estimated in terms of the normalized autocorrelation coefficients ρ_L as

$$\kappa = 1 + 2\sum_{L=1}^{N} \rho_L, \tag{E.6}$$

where the autocorrelation coefficients for a given lag time L are defined using the autocovariance function

$$\Gamma_L = \frac{\sum_{k=1}^{N-L} \sqrt{w_k w_{k+L}}(E_k - \bar{E})(E_{k+L} - \bar{E})}{\sum_{k=1}^{N-L} \sqrt{w_k w_{k+L}}} \tag{E.7}$$

as

$$\rho_L = \frac{\Gamma_L}{\Gamma_0}. \tag{E.8}$$

They measure the correlation between data points and decrease rapidly with L. At the same time, ρ_L becomes less precise as L increases, since the number of data samples used for its calculation decreases according to Eq. (E.7). Therefore, it is instructive to truncate the summation in Eq. (E.6) to the frist L_c terms:

$$\kappa = 1 + 2\sum_{L=1}^{L_c} \rho_L, \tag{E.9}$$

where the cutoff L_c is determined as the smallest integer that satisfies

$$\kappa \leq \frac{L_c}{2} - 1. \tag{E.10}$$

Fig. E.2(top) shows the autocorrelation coefficients as a function of lag time in a typical ph-AFQMC simulation, while Fig. E.2(bottom) illustrates the determination of the cutoff L_c and the resulting correlation length κ.

Block Averaging

The block averaging method partitions the original data $\{w_k, E_k\}$ into N_b blocks of length L. For each block $b = 1, 2, \ldots, N_b$, the block averages

$$w'_b = \sum_{k=(b-1)L+1}^{bL} w_k \qquad E'_b = \frac{\sum_{k=(b-1)L+1}^{bL} w_k E_k}{w'_b} \tag{E.11}$$

are assumed to be less correlated. This property can be used to estimate the correlation length.

The overall weighted average value

$$\bar{E}_L = \frac{\sum_{b=1}^{N_b} w'_b E'_b}{\sum_{b=1}^{N_b} w'_b} = \frac{\sum_{k}^{N} w_k E_k}{\sum_{k}^{N} w_k E_k} = \bar{E} \tag{E.12}$$

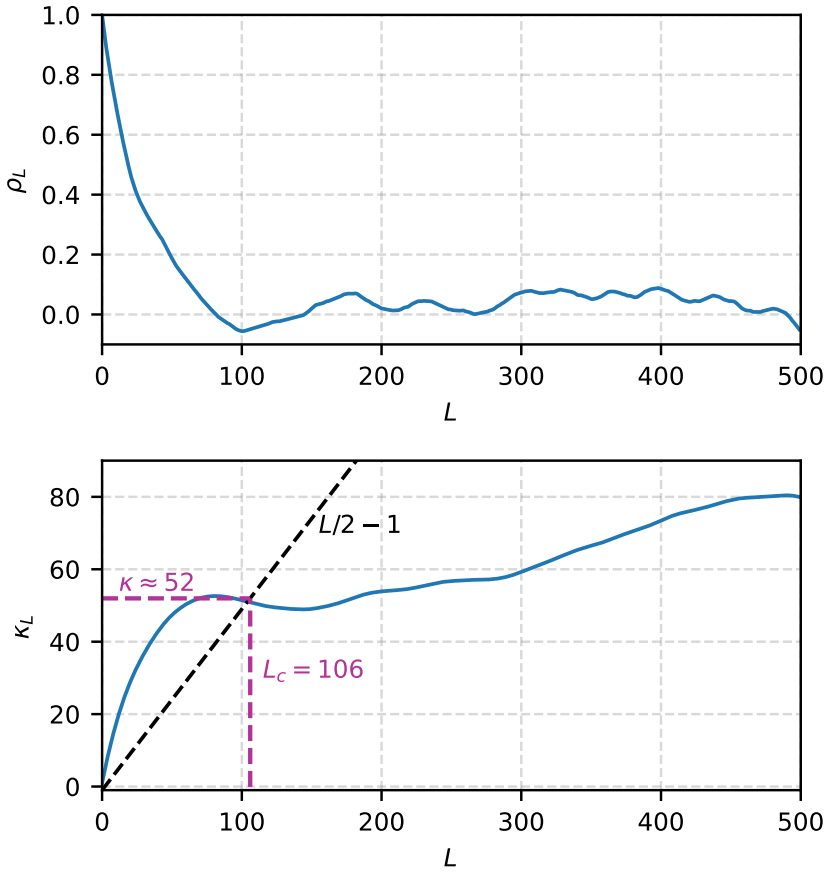

Figure E.2: (Top) The autocorrelation coefficients ρ_L decrease rapidly with increasing lag time L. A faster decay of ρ_L indicates a shorter correlation length. (Bottom) The robust estimation of the correlation length is determined by the intersection of the curve $\kappa_L = 1 + \sum_{l=1}^{L} 2\rho_l$ with the straight line $L/2 - 1$.

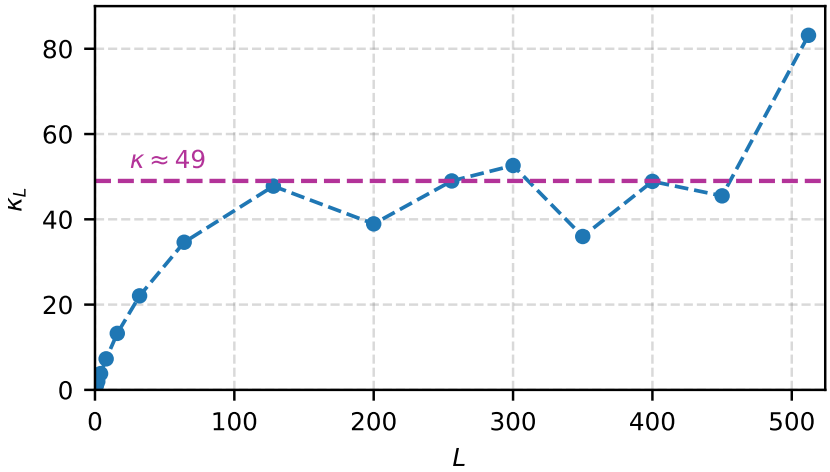

Figure E.3: In block averaging, the estimated correlation lengths κ_L increase with block size L and eventually saturate at a fixed value κ.

is independent of the block length L. On the other hand, the standard deviation

$$\sigma^2_{\bar{E},L} = \frac{\sum_b w'_b (E'_b - \bar{E})^2}{v_1 - \frac{v_2}{v_1}}, \tag{E.13}$$

and the standard deviation of the mean

$$\sigma_{\bar{E},L} = \frac{\sigma_{E,L}}{\sqrt{\frac{v_1^2}{v_2}}} \tag{E.14}$$

increase with the block length L. Here, the weight moments v_p are computed using the block weights w'_b.

The correlation length for various block sizes L can be estimated as

$$\kappa_L = \frac{\frac{\sigma^2_{E,L}}{N_b}}{\frac{\sigma^2_E}{N}} = \frac{L\sigma^2_{E,L}}{\sigma^2_E}, \tag{E.15}$$

where κ_L saturates to a fixed value κ as the block size L increases. To estimate κ, it is convenient to plot κ_L versus L, as shown in Fig. E.3.

A more practical approach involves calculating κ_L for block sizes that are powers of 2[218]. We estimate the final correlation length $\kappa = \kappa_L$ by determining the smallest L that satisfies the stopping criterion

$$\frac{\kappa_L}{\kappa_{L/2}} \leq \sqrt{2}, \tag{E.16}$$

ensuring a robust estimate of the correlation length. The magenta line in Fig. E.3 highlights the correlation length determined using this stopping criterion.

Appendix F

Short Time AFQMC Propagation

In this appendix, we provide arguments supporting the use of the hybrid energy (Eq. 3.37) as an energy estimator in AFQMC. Since the computation of hybrid energies requires AFQMC propagation, they also serve as a valuable tool for verifying the correctness of the AFQMC propagation.

We begin this appendix by demonstrating how the local energy of a walker can be extracted from short-time many-body propagation. In the following section, we extend this result to the Hubbard-Stratonovich transformed propagator. Finally, the last section presents a practical implementation of the short-time propagation, establishing the connection to the hybrid energy estimator.

Expectation Value of the Exact Propagator

The expectation value of the Hamiltonian $\hat{H}$ can be extracted from the short-time imaginary propagation $\hat{P}(\tau)$ as follows:

$$\begin{aligned}\langle \hat{H} \rangle &= \lim_{\tau\to 0} \frac{-\log\langle \hat{P}(\tau)\rangle}{\tau} = \lim_{\tau\to 0} \frac{-\log\langle e^{-\tau\hat{H}}\rangle}{\tau} = \\ &= \lim_{\tau\to 0} \frac{-\log\langle 1-\tau\hat{H}+\frac{1}{2}\tau^2\hat{H}^2+\cdots\rangle}{\tau} \\ &= \lim_{\tau\to 0} \frac{-\log\langle 1-\tau\hat{H}\rangle}{\tau} \\ &= \langle \hat{H}\rangle\,,\end{aligned} \tag{F.1}$$

where we used the following approximation for the logarithm

$$\lim_{x\to 0} \log(1+x) = x. \tag{F.2}$$

For a many-body Hamiltonian defined in Eq. (2.4), the mixed expectation value of the form

$$\langle \hat{H}\rangle = \frac{\langle \Phi_{\mathrm{T}}|\hat{H}|\Psi\rangle}{\langle \Phi_{\mathrm{T}}|\Psi\rangle} = E_{\mathrm{L}}(\Psi) \tag{F.3}$$

is equivalent to the local energy defined in Sec. 3.3. In the remainder of the text, we will implicitly assume that the expectation value $\langle\cdot\rangle$ refers to the mixed expectation value of the form $\frac{\langle \Phi_{\mathrm{T}}|\cdot|\Psi\rangle}{\langle \Phi_{\mathrm{T}}|\Psi\rangle}$.

Expectation Value of the Hubbard-Stratonovich Transformed Propagator

In AFQMC, the exact propagator is replaced by the Hubbard-Stratonovich transformed propagator

$$\hat{P}(\tau) \to \hat{P}_{\mathrm{HS}}(\tau) = \int \mathrm{d}\mathbf{x}\; p(\mathbf{x})\, \hat{B}(\mathbf{x}), \tag{F.4}$$

where $p(\mathbf{x})$, $\hat{B}(\mathbf{x})$, and $\hat{\mathcal{H}}(\mathbf{x})$ are defined in Sec. 3.1.

Similar to Eq. (F.1), we demonstrate that the expectation value of the Hamiltonian can be extracted from the short-time propagation using the Hubbard-Stratonovich transformed propagator:

$$\begin{aligned}
\langle \hat{H} \rangle &= \lim_{\tau\to 0} \frac{-\log \langle \hat{P}_{\mathrm{HS}}(\tau) \rangle}{\tau} \\
&= \lim_{\tau\to 0} \frac{-\log \int \mathrm{d}\mathbf{x}\; p(\mathbf{x})\, \langle \hat{B}(\mathbf{x}) \rangle}{\tau} \\
&= \lim_{\tau\to 0} \frac{-\log \langle 1 - \tau\hat{H}_1 - i\sqrt{\tau}\sum_g \hat{L}_g \overbrace{\int \mathrm{d}\mathbf{x}\; p(\mathbf{x})\, x_g}^{0} - \frac{\tau}{2}\sum_{gg'} \hat{L}_g \hat{L}_{g'} \overbrace{\int \mathrm{d}\mathbf{x}\; p(\mathbf{x})\, x_g x_{g'}}^{\delta_{gg'}} \rangle}{\tau} \\
&= \lim_{\tau\to 0} \frac{-\log \langle 1 - \tau(\hat{H}_1 + \frac{1}{2}\sum_g \hat{L}_g^2) \rangle}{\tau} \\
&= \lim_{\tau\to 0} \frac{-\log \langle 1 - \tau\hat{H} \rangle}{\tau} \\
&= \langle \hat{H} \rangle .
\end{aligned} \tag{F.5}$$

Here, we used Eq. (3.12) for the effective interaction $\hat{\mathcal{H}}(\mathbf{x})$ and expanded the propagator up to terms linear in τ, as higher-order terms vanish in the limit $\tau \to 0$. In addition, we used the following properties of the standard normal distribution:

$$\int \mathrm{d}\mathbf{x}\; p(\mathbf{x})\, x_g = 0, \qquad \int \mathrm{d}\mathbf{x}\; p(\mathbf{x})\, x_g x_{g'} = \delta_{gg'}. \tag{F.6}$$

Stochastic Evaluation of the Energy: Hybrid Energy Estimator

For a practical evaluation, the integral in Eq. (F.4) is computed using Monte Carlo sampling. To achieve this, we initialize N_w walkers as $|\Psi_w\rangle = |\Psi\rangle$, and propagate them for a single time step, yielding:

$$|\Psi'_w\rangle = \hat{B}(\mathbf{x}_w)\, |\Psi_w\rangle . \tag{F.7}$$

The average value of the hybrid energy (Eq. 3.37) in the limit of zero time step, and in the limit of infinitely many walkers

$$\lim_{\substack{\tau\to 0 \\ N_w\to\infty}} \frac{1}{N_w} \sum_w E_{\mathrm{H}}(\Psi_w) \tag{F.8}$$

converges to the expectation value $E_{\mathrm{L}}(\Psi)$ as proven below:

$$
\begin{aligned}
&\lim_{\substack{\tau\to 0\\ N_w\to\infty}} \frac{1}{N_w}\sum_w E_{\mathrm{H}}(\Psi_w) \\
&= \lim_{\substack{\tau\to 0\\ N_w\to\infty}} \frac{1}{N_w}\sum_w \frac{-\log\frac{\langle\Phi_{\mathrm{T}}|\Psi'_w\rangle}{\langle\Phi_{\mathrm{T}}|\Psi_w\rangle}}{\tau} \\
&= \lim_{\substack{\tau\to 0\\ N_w\to\infty}} \frac{1}{N_w}\sum_w \frac{-\log\frac{\langle\Phi_{\mathrm{T}}|\hat{B}(\mathbf{x}_w)|\Psi\rangle}{\langle\Phi_{\mathrm{T}}|\Psi\rangle}}{\tau} \\
&= \lim_{\substack{\tau\to 0\\ N_w\to\infty}} \frac{1}{N_w}\sum_w \frac{-\log\langle\hat{B}(\mathbf{x}_w)\rangle}{\tau} \\
&= \lim_{\tau\to 0} \frac{-\log\langle 1-\tau\hat{H}_1 - i\sqrt{\tau}\sum_g \hat{L}_g \overbrace{\lim_{N_w\to\infty}\frac{1}{N_w}\sum_w x_{gw}}^{0} - \frac{\tau}{2}\sum_{gg'}\hat{L}_g\hat{L}_{g'}\overbrace{\lim_{N_w\to\infty}\frac{1}{N_w}\sum_w x_{gw}x_{g'w}}^{\delta_{gg'}}\rangle}{\tau} \\
&= \lim_{\tau\to 0} \frac{-\log\langle 1-\tau\hat{H}_1 - \frac{\tau}{2}\sum_g \hat{L}_g^2\rangle}{\tau} \\
&= \lim_{\tau\to 0} \frac{-\log\langle 1-\tau\hat{H}\rangle}{\tau} \\
&= \langle\hat{H}\rangle = \frac{\langle\Phi_{\mathrm{T}}|\hat{H}|\Psi\rangle}{\langle\Phi_{\mathrm{T}}|\Psi\rangle} = E_{\mathrm{L}}(\Psi).
\end{aligned}
\tag{F.9}
$$

In the fifth row of the derivation above, we expanded the propagator $\hat{B}(\mathbf{x}_w)$ to first order in τ, and used the discrete form of Eq. (F.6) to evaluate the sums over walkers.

The advantage of this approach is that energy evaluation requires only the computation of overlaps between non-orthogonal Slater determinants, resulting in cubic scaling in the case of a Hartree-Fock trial wave function. However, achieving accurate energy estimates requires small time steps and a large number of walkers, typically $N_w >> N$, to minimize statistical errors. Despite this limitation, the hybrid energy estimator remains useful when local energy evaluation is computationally too expensive or as a verification tool for AFQMC propagation.

List of Figures

List of Tables

Bibliography

[1] D. J. Scalapino and R. L. Sugar, "Monte carlo calculations of coupled boson-fermion systems. ii," *Phys. Rev. B*, vol. 24, pp. 4295–4308, 8 Oct. 1981. DOI: 10.1103/physrevb.24.4295. [Online]. Available: http://dx.doi.org/10.1103/physrevb.24.4295.

[2] R. Blankenbecler, D. J. Scalapino, and R. L. Sugar, "Monte carlo calculations of coupled boson-fermion systems. i," *Phys. Rev. D*, vol. 24, pp. 2278–2286, 8 Oct. 1981. DOI: 10.1103/physrevd.24.2278. [Online]. Available: http://dx.doi.org/10.1103/physrevd.24.2278.

[3] G. Sugiyama and S. Koonin, "Auxiliary field monte-carlo for quantum many-body ground states," *Ann. Phys.*, vol. 168, no. 1, pp. 1–26, 1986, ISSN: 0003-4916. DOI: https://doi.org/10.1016/0003-4916(86)90107-7. [Online]. Available: https://www.sciencedirect.com/science/article/pii/0003491686901077.

[4] S. Sorella, S. Baroni, R. Car, and M. Parrinello, "A novel technique for the simulation of interacting fermion systems," *Europhys. Lett.*, vol. 8, no. 7, pp. 663–668, Apr. 1989. DOI: 10.1209/0295-5075/8/7/014. [Online]. Available: https://doi.org/10.1209/0295-5075/8/7/014.

[5] S. R. White, D. J. Scalapino, R. L. Sugar, E. Y. Loh, J. E. Gubernatis, and R. T. Scalettar, "Numerical study of the two-dimensional hubbard model," *Phys. Rev. B*, vol. 40, pp. 506–516, 1 Jul. 1989. DOI: 10.1103/PhysRevB.40.506. [Online]. Available: https://link.aps.org/doi/10.1103/PhysRevB.40.506.

[6] S. Zhang, J. Carlson, and J. E. Gubernatis, "Constrained path quantum monte carlo method for fermion ground states," *Phys. Rev. Lett.*, vol. 74, pp. 3652–3655, 18 May 1995. DOI: 10.1103/PhysRevLett.74.3652. [Online]. Available: https://link.aps.org/doi/10.1103/PhysRevLett.74.3652.

[7] S. Zhang, J. Carlson, and J. Gubernatis, "Constrained path monte carlo method for fermion ground states," *Phys. Rev. B*, vol. 55, p. 7464, 1997. DOI: 10.1103/PhysRevB.55.7464.

[8] S. Zhang and H. Krakauer, "Quantum monte carlo method using phase-free random walks with slater determinants," *Phys. Rev. Lett.*, vol. 90, p. 136 401, 2003. DOI: 10.1103/PhysRevLett.90.136401.

[9] W. A. Al-Saidi, S. Zhang, and H. Krakauer, "Auxiliary-field quantum monte carlo calculations of molecular systems with a gaussian basis," *J. Chem. Phys.*, vol. 124, no. 22, p. 224 101, 2006. DOI: 10.1063/1.2200885.

[10] M. Suewattana, W. Purwanto, S. Zhang, H. Krakauer, and E. J. Walter, "Phaseless auxiliary-field quantum monte carlo calculations with plane waves and pseudopotentials: Applications to atoms and molecules," *Phys. Rev. B*, vol. 75, p. 245 123, 2007. DOI: 10.1103/PhysRevB.75.245123.

[11] P. Rosenberg, H. Shi, and S. Zhang, "Accurate computations of rashba spin-orbit coupling in interacting systems: From the fermi gas to real materials," *J. Phys. Chem. Solids*, vol. 128, pp. 161–168, 2019, Spin-Orbit Coupled Materials, ISSN: 0022-3697. DOI: https://doi.org/10.1016/j.jpcs.2017.12.026. [Online]. Available: https://www.sciencedirect.com/science/article/pii/S0022369717316554.

[12] D. Danilov, B. Ganoe, M. Munyi, and J. Shee, "Capturing strong correlation in molecules with phaseless auxiliary-field quantum monte carlo using generalized hartree–fock trial wave functions," *J. Chem. Theory Comput.*, vol. 21, no. 3, pp. 1136–1152, 2025, PMID: 39817358. DOI: 10.1021/acs.jctc.4c01251. [Online]. Available: https://doi.org/10.1021/acs.jctc.4c01251.

[13] J. Carlson, S. Gandolfi, K. E. Schmidt, and S. Zhang, "Auxiliary-field quantum monte carlo method for strongly paired fermions," *Phys. Rev. A*, vol. 84, p. 061 602, 6 Dec. 2011. DOI: 10.1103/PhysRevA.84.061602. [Online]. Available: https://link.aps.org/doi/10.1103/PhysRevA.84.061602.

[14] E. Vitali, P. Rosenberg, and S. Zhang, "Calculating ground-state properties of correlated fermionic systems with bcs trial wave functions in slater determinant path-integral approaches," *Phys. Rev. A*, vol. 100, p. 023 621, 2 Aug. 2019. DOI: 10.1103/PhysRevA.100.023621. [Online]. Available: https://link.aps.org/doi/10.1103/PhysRevA.100.023621.

[15] J. Lee, S. Zhang, and D. R. Reichman, "Constrained-path auxiliary-field quantum monte carlo for coupled electrons and phonons," *Phys. Rev. B*, vol. 103, p. 115 123, 11 Mar. 2021. DOI: 10.1103/PhysRevB.103.115123. [Online]. Available: https://link.aps.org/doi/10.1103/PhysRevB.103.115123.

[16] L. Weber, L. dos Anjos Cunha, M. A. Morales, A. Rubio, and S. Zhang, *Phaseless auxiliary-field quantum monte carlo method for cavity-qed matter systems*, arXiv:physics.chem-ph/2410.18838. arXiv.org ePrint archive. https://arxiv.org/abs/2410.18838 (accessed Feb, 12, 2025), 2024.

[17] W. Purwanto, S. Zhang, and H. Krakauer, "Excited state calculations using phaseless auxiliary-field quantum monte carlo: Potential energy curves of low-lying c2 singlet states," *J. Chem. Phys.*, vol. 130, no. 9, p. 094 107, 2009. DOI: 10.1063/1.3077920. [Online]. Available: https://doi.org/10.1063/1.3077920.

[18] F. Ma, S. Zhang, and H. Krakauer, "Excited state calculations in solids by auxiliary-field quantum monte carlo," *New J. Phys.*, vol. 15, p. 093 017, 9 Sep. 2013. DOI: 10.1088/1367-2630/15/9/093017. [Online]. Available: http://dx.doi.org/10.1088/1367-2630/15/9/093017.

[19] B. M. Rubenstein, S. Zhang, and D. R. Reichman, "Finite-temperature auxiliary-field quantum monte carlo technique for bose-fermi mixtures," *Phys. Rev. A*, vol. 86, p. 053 606, 5 Nov. 2012. DOI: 10.1103/PhysRevA.86.053606. [Online]. Available: https://link.aps.org/doi/10.1103/PhysRevA.86.053606.

[20] Y.-Y. He, M. Qin, H. Shi, Z.-Y. Lu, and S. Zhang, "Finite-temperature auxiliary-field quantum monte carlo: Self-consistent constraint and systematic approach to low temperatures," *Phys. Rev. B*, vol. 99, p. 045 108, 4 Jan. 2019. DOI: 10.1103/PhysRevB.99.045108. [Online]. Available: https://link.aps.org/doi/10.1103/PhysRevB.99.045108.

[21] M. Motta and S. Zhang, "Communication: Calculation of interatomic forces and optimization of molecular geometry with auxiliary-field quantum monte carlo," *The Journal of Chemical Physics*, vol. 148, no. 18, p. 181 101, May 2018, ISSN: 0021-9606. DOI: 10.1063/1.5029508. [Online]. Available: https://doi.org/10.1063/1.5029508.

[22] S. Chen, M. Motta, F. Ma, and S. Zhang, "Ab initio electronic density in solids by many-body plane-wave auxiliary-field quantum monte carlo calculations," *Phys. Rev. B*, vol. 103, p. 075 138, 7 Feb. 2021. DOI: 10.1103/PhysRevB.103.075138. [Online]. Available: https://link.aps.org/doi/10.1103/PhysRevB.103.075138.

[23] M. Motta, J. Shee, S. Zhang, and G. K.-L. Chan, "Efficient ab initio auxiliary-field quantum monte carlo calculations in gaussian bases via low-rank tensor decomposition," *J. Chem. Theory Comput.*, vol. 15, no. 6, pp. 3510–3521, 2019, PMID: 31091103. DOI: 10.1021/acs.jctc.8b00996. [Online]. Available: https://doi.org/10.1021/acs.jctc.8b00996.

[24] F. D. Malone, S. Zhang, and M. A. Morales, "Overcoming the memory bottleneck in auxiliary field quantum monte carlo simulations with interpolative separable density fitting," *J. Chem. Theory Comput.*, vol. 15, no. 1, pp. 256–264, 2019. DOI: 10.1021/acs.jctc.8b00944. [Online]. Available: https://doi.org/10.1021/acs.jctc.8b00944.

[25] J. L. Weber *et al.*, "A localized-orbital energy evaluation for auxiliary-field quantum monte carlo," *J. Chem. Theory Comput.*, vol. 18, no. 6, pp. 3447–3459, 2022, PMID: 35507769. DOI: 10.1021/acs.jctc.2c00111. [Online]. Available: https://doi.org/10.1021/acs.jctc.2c00111.

[26] J. Lee and D. R. Reichman, "Stochastic resolution-of-the-identity auxiliary-field quantum monte carlo: Scaling reduction without overhead," *J. Chem. Phys.*, vol. 153, no. 4, p. 044 131, 2020. DOI: 10.1063/5.0015077. [Online]. Available: https://doi.org/10.1063/5.0015077.

[27] W. A. Al-Saidi, S. Zhang, and H. Krakauer, "Bond breaking with auxiliary-field quantum monte carlo," *J. Chem. Phys.*, vol. 127, no. 14, p. 144 101, 2007. DOI: 10.1063/1.2770707. [Online]. Available: https://doi.org/10.1063/1.2770707.

[28] W. Purwanto, H. Krakauer, Y. Virgus, and S. Zhang, "Assessing weak hydrogen binding on ca+ centers: An accurate many-body study with large basis sets," *J. Chem. Phys.*, vol. 135, no. 16, p. 164 105, 2011. DOI: 10.1063/1.3654002. [Online]. Available: https://doi.org/10.1063/1.3654002.

[29] Y. Virgus, W. Purwanto, H. Krakauer, and S. Zhang, "Ab initio many-body study of cobalt adatoms adsorbed on graphene," *Phys. Rev. B*, vol. 86, p. 241 406, 24 Dec. 2012. DOI: 10.1103/PhysRevB.86.241406. [Online]. Available: https://link.aps.org/doi/10.1103/PhysRevB.86.241406.

[30] W. Purwanto, S. Zhang, and H. Krakauer, "An auxiliary-field quantum monte carlo study of the chromium dimer," *J. Chem. Phys.*, vol. 142, no. 6, p. 064 302, 2015. DOI: 10.1063/1.4906829. [Online]. Available: https://doi.org/10.1063/1.4906829.

[31] M. Motta *et al.*, "Towards the solution of the many-electron problem in real materials: Equation of state of the hydrogen chain with state-of-the-art many-body methods," *Phys. Rev. X*, vol. 7, p. 031 059, 3 Sep. 2017. DOI: 10.1103/PhysRevX.7.031059. [Online]. Available: https://link.aps.org/doi/10.1103/PhysRevX.7.031059.

[32] H. Hao, J. Shee, S. Upadhyay, C. Ataca, K. D. Jordan, and B. M. Rubenstein, "Accurate predictions of electron binding energies of dipole-bound anions via quantum monte carlo methods," *J. Phys. Chem. Lett.*, vol. 9, pp. 6185–6190, 21 Nov. 2018, ISSN: 19487185. DOI: 10.1021/acs.jpclett.8b02733.

[33] J. Shee, B. Rudshteyn, E. J. Arthur, S. Zhang, D. R. Reichman, and R. A. Friesner, "On achieving high accuracy in quantum chemical calculations of 3d transition metal-containing systems: A comparison of auxiliary-field quantum monte carlo with coupled cluster, density functional theory, and experiment for diatomic molecules," *J. Chem. Theory Comput.*, vol. 15, no. 4, pp. 2346–2358, 2019, PMID: 30883110. DOI: 10.1021/acs.jctc.9b00083. [Online]. Available: https://doi.org/10.1021/acs.jctc.9b00083.

[34] J. Lee, F. D. Malone, and M. A. Morales, "An auxiliary-field quantum monte carlo perspective on the ground state of the dense uniform electron gas: An investigation with hartree-fock trial wavefunctions," *J. Chem. Phys.*, vol. 151, p. 064 122, 6 Aug. 2019. DOI: 10.1063/1.5109572. [Online]. Available: http://dx.doi.org/10.1063/1.5109572.

[35] E. J. Landinez Borda, J. Gomez, and M. A. Morales, "Non-orthogonal multi-slater determinant expansions in auxiliary field quantum monte carlo," *J. Chem. Phys.*, vol. 150, no. 7, p. 074 105, 2019. DOI: 10.1063/1.5049143. [Online]. Available: https://doi.org/10.1063/1.5049143.

[36] B. Rudshteyn *et al.*, "Predicting ligand-dissociation energies of 3d coordination complexes with auxiliary-field quantum monte carlo," *J. Chem. Theory Comput.*, vol. 16, pp. 3041–3054, 5 May 2020, ISSN: 15499626. DOI: 10.1021/acs.jctc.0c00070.

[37] J. Lee, F. D. Malone, and D. R. Reichman, "The performance of phaseless auxiliary-field quantum monte carlo on the ground state electronic energy of benzene," *J. Chem. Phys.*, vol. 153, no. 12, p. 126 101, 2020. DOI: 10.1063/5.0024835. [Online]. Available: https://doi.org/10.1063/5.0024835.

[38] B. Rudshteyn *et al.*, "Calculation of metallocene ionization potentials via auxiliary field quantum monte carlo: Toward benchmark quantum chemistry for transition metals," *J. Chem. Theory Comput.*, vol. 18, no. 5, pp. 2845–2862, 2022, PMID: 35377642. DOI: 10.1021/acs.jctc.1c01071. [Online]. Available: https://doi.org/10.1021/acs.jctc.1c01071.

[39] J. Lee, H. Q. Pham, and D. R. Reichman, "Twenty years of auxiliary-field quantum monte carlo in quantum chemistry: An overview and assessment on main group chemistry and bond-breaking," *J. Chem. Theory Comput.*, vol. 18, no. 12, pp. 7024–7042, 2022, PMID: 36255074. DOI: 10.1021/acs.jctc.2c00802. eprint: https://doi.org/10.1021/acs.jctc.2c00802. [Online]. Available: https://doi.org/10.1021/acs.jctc.2c00802.

[40] J. Shee, J. L. Weber, D. R. Reichman, R. A. Friesner, and S. Zhang, "On the potentially transformative role of auxiliary-field quantum Monte Carlo in quantum chemistry: A highly accurate method for transition metals and beyond," *J. Chem. Phys.*, vol. 158, no. 14, p. 140 901, 2023. DOI: 10.1063/5.0134009. [Online]. Available: https://doi.org/10.1063/5.0134009.

[41] Z. Sukurma, M. Schlipf, M. Humer, A. Taheridehkordi, and G. Kresse, "Benchmark phaseless auxiliary-field quantum monte carlo method for small molecules," *J. Chem. Theory Comput.*, vol. 19, no. 15, pp. 4921–4934, 2023. DOI: 10.1021/acs.jctc.3c00322.

[42] A. Taheridehkordi, M. Schlipf, Z. Sukurma, M. Humer, A. Grüneis, and G. Kresse, "Phaseless auxiliary field quantum Monte Carlo with projector-augmented wave method for solids," *J. Chem. Phys.*, vol. 159, no. 4, p. 044 109, Jul. 2023. DOI: 10.1063/5.0156657.

[43] H. Neugebauer, H. T. Vuong, J. L. Weber, R. A. Friesner, J. Shee, and A. Hansen, "Toward benchmark-quality ab initio predictions for 3d transition metal electrocatalysts: A comparison of ccsd(t) and ph-afqmc," *J. Chem. Theory Comput.*, vol. 19, no. 18, pp. 6208–6225, 2023, PMID: 37655473. DOI: 10.1021/acs.jctc.3c00617. [Online]. Available: https://doi.org/10.1021/acs.jctc.3c00617.

[44] Y. Wei, S. Debnath, J. L. Weber, A. Mahajan, D. R. Reichman, and R. A. Friesner, "Scalable ab initio electronic structure methods with near chemical accuracy for main group chemistry," *J. Phys. Chem. A*, vol. 128, no. 28, pp. 5796–5807, 2024, PMID: 38970826. DOI: 10.1021/acs.jpca.4c02853. [Online]. Available: https://doi.org/10.1021/acs.jpca.4c02853.

[45] A. Tajti *et al.*, "Heat: High accuracy extrapolated ab initio thermochemistry," *J. Chem. Phys.*, vol. 121, no. 23, pp. 11 599–11 613, 2004. DOI: 10.1063/1.1811608. [Online]. Available: https://doi.org/10.1063/1.1811608.

[46] J. Shee, E. J. Arthur, S. Zhang, D. R. Reichman, and R. A. Friesner, "Phaseless auxiliary-field quantum monte carlo on graphical processing units," *J. Chem. Theory Comput.*, vol. 14, no. 8, pp. 4109–4121, 2018, PMID: 29897748. DOI: 10.1021/acs.jctc.8b00342. [Online]. Available: https://doi.org/10.1021/acs.jctc.8b00342.

[47] H. Shi and S. Zhang, "Some recent developments in auxiliary-field quantum monte carlo for real materials," *J. Chem. Phys.*, vol. 154, no. 2, p. 024 107, 2021. DOI: 10.1063/5.0031024. [Online]. Available: https://doi.org/10.1063/5.0031024.

[48] A. Mahajan and S. Sharma, "Efficient local energy evaluation for multi-Slater wave functions in orbital space quantum Monte Carlo," *J. Chem. Phys.*, vol. 153, no. 19, p. 194 108, 2020, ISSN: 0021-9606. DOI: 10.1063/5.0025055. [Online]. Available: https://doi.org/10.1063/5.0025055.

[49] A. Mahajan and S. Sharma, "Taming the sign problem in auxiliary-field quantum monte carlo using accurate wave functions," *J. Chem. Theory Comput.*, vol. 17, no. 8, pp. 4786–4798, 2021, PMID: 34232637. DOI: 10.1021/acs.jctc.1c00371. [Online]. Available: https://doi.org/10.1021/acs.jctc.1c00371.

[50] A. Mahajan, J. Lee, and S. Sharma, "Selected configuration interaction wave functions in phaseless auxiliary field quantum monte carlo," *J. Chem. Phys.*, vol. 156, no. 17, p. 174 111, 2022. DOI: 10.1063/5.0087047. [Online]. Available: https://doi.org/10.1063/5.0087047.

[51] F. D. Malone, A. Mahajan, J. S. Spencer, and J. Lee, "<tt>ipie</tt>: A python-based auxiliary-field quantum monte carlo program with flexibility and efficiency on cpus and gpus," *J. Chem. Theory Comput.*, vol. 19, pp. 109–121, 1 Jan. 2023. DOI: 10.1021/acs.jctc.2c00934. [Online]. Available: http://dx.doi.org/10.1021/acs.jctc.2c00934.

[52] A. Mahajan, J. H. Thorpe, J. S. Kurian, D. R. Reichman, D. A. Matthews, and S. Sharma, "Beyond ccsd(t) accuracy at lower scaling with auxiliary field quantum monte carlo," *J.Chem. Theory Comput.*, vol. 21, no. 4, pp. 1626–1642, 2025, PMID: 39907123. DOI: 10.1021/acs.jctc.4c01314. [Online]. Available: https://doi.org/10.1021/acs.jctc.4c01314.

[53] H. Fukutome, "Theory of Resonating Quantum Fluctuations in a Fermion System: Resonating Hartree-Fock Approximation," *Prog. Theor. Phys.*, vol. 80, no. 3, pp. 417–432, Sep. 1988, ISSN: 0033-068X. DOI: 10.1143/PTP.80.417. [Online]. Available: https://doi.org/10.1143/PTP.80.417.

[54] Z. Sukurma, M. Schlipf, M. Humer, A. Taheridehkordi, and G. Kresse, "Toward large-scale afqmc calculations: Large time step auxiliary-field quantum monte carlo," *J. Chem. Theory Comput.*, vol. 20, no. 10, pp. 4205–4217, 2024. DOI: 10.1021/acs.jctc.4c00304. [Online]. Available: https://doi.org/10.1021/acs.jctc.4c00304.

[55] Z. Sukurma, M. Schlipf, and G. Kresse, *Self-refinement of auxiliary-field quantum monte carlo via non-orthogonal configuration interaction*, arXiv:physics.chem-ph/2501.12765. arXiv.org ePrint archive. https://arxiv.org/abs/2501.12765 (accessed Feb, 05, 2025), 2025.

[56] M. Born and R. Oppenheimer, "Zur Quantentheorie der Molekeln," *Ann. Phys.*, vol. 389, no. 20, pp. 457–484, Jan. 1927. DOI: 10.1002/andp.19273892002.

[57] A. Quarteroni, R. Sacco, and S. F., *Numerical Mathematics (Texts in Applied Mathematics)*. Berlin, Heidelberg: Springer-Verlag, 2006, ISBN: 3540346589.

[58] A. Szabo and N. S. Ostlund, *Modern Quantum Chemistry: Introduction to Advanced Electronic Structure Theory*, First. Mineola: Dover Publications, Inc., 1996.

[59] T. Helgaker, P. Jørgensen, and J. Olsen, *Molecular Electronic Structure Theory*. Chichester: John Wiley & Sons, LTD, 2000.

[60] A. L. Fetter and J. D. Walecka, *Quantum Theory of Many-Particle Systems*. Boston: McGraw-Hill, 1971.

[61] H. Bruus and F. K., *Many-Body Quantum Theory in Condensed Matter Physics: An Introduction*. Oxford University Press, 2004, ISBN: 978-1-383-02959-8. [Online]. Available: https://academic.oup.com/book/54902.

[62] B. I. Dunlap, "Robust and variational fitting," *Phys. Chem. Chem. Phys.*, vol. 2, pp. 2113–2116, 10 2000. DOI: 10.1039/b000027m. [Online]. Available: http://dx.doi.org/10.1039/b000027m.

[63] M. J. Field, "Density fitting for qc/mm interactions," *J. Phys. Chem. A*, vol. 126, pp. 6348–6357, 36 Sep. 2022, ISSN: 15205215. DOI: 10.1021/acs.jpca.2c05655.

[64] N. H. F. Beebe and J. Linderberg, "Simplifications in the generation and transformation of two-electron integrals in molecular calculations," *Int. J. Quantum Chem.*, vol. 12, no. 4, pp. 683–705, 1977. DOI: https://doi.org/10.1002/qua.560120408. eprint: https://onlinelibrary.wiley.com/doi/pdf/10.1002/qua.560120408. [Online]. Available: https://onlinelibrary.wiley.com/doi/abs/10.1002/qua.560120408.

[65] H. Koch, A. Sánchez de Merás, and T. B. Pedersen, "Reduced scaling in electronic structure calculations using cholesky decompositions," *J. Chem. Phys.*, vol. 118, no. 21, pp. 9481–9484, 2003. DOI: 10.1063/1.1578621. [Online]. Available: https://doi.org/10.1063/1.1578621.

[66] F. Aquilante *et al.*, "Molcas 7: The next generation," *J. Comput. Chem.*, vol. 31, no. 1, pp. 224–247, 2010. DOI: https://doi.org/10.1002/jcc.21318. [Online]. Available: https://onlinelibrary.wiley.com/doi/abs/10.1002/jcc.21318.

[67] F. Hummel, T. Tsatsoulis, and A. Grüneis, "Low rank factorization of the coulomb integrals for periodic coupled cluster theory," *J. Chem. Phys.*, vol. 146, no. 12, p. 124 105, 2017. DOI: 10.1063/1.4977994. [Online]. Available: https://doi.org/10.1063/1.4977994.

[68] H. B. Schlegel and J. J. W. McDouall, "Do you have scf stability and convergence problems?" In *Computational Advances in Organic Chemistry: Molecular Structure and Reactivity*, C. Ögretir and I. G. Csizmadia, Eds. Dordrecht: Springer Netherlands, 1991, pp. 167–185, ISBN: 978-94-011-3262-6. DOI: 10.1007/978-94-011-3262-6_2. [Online]. Available: https://doi.org/10.1007/978-94-011-3262-6_2.

[69] Kudin, Konstantin N. and Scuseria, Gustavo E., "Converging self-consistent field equations in quantum chemistry – recent achievements and remaining challenges," *ESAIM: M2AN*, vol. 41, no. 2, pp. 281–296, 2007. DOI: 10.1051/m2an:2007022. [Online]. Available: https://doi.org/10.1051/m2an:2007022.

[70] V. R. Saunders and I. H. Hillier, "A "level–shifting" method for converging closed shell hartree–fock wave functions," *Int. J. Quantum Chem.*, vol. 7, no. 4, pp. 699–705, 1973. DOI: https://doi.org/10.1002/qua.560070407. [Online]. Available: https://onlinelibrary.wiley.com/doi/abs/10.1002/qua.560070407.

[71] P. Pulay, "Convergence acceleration of iterative sequences. the case of scf iteration," *Chem. Phys. Lett.*, vol. 73, no. 2, pp. 393–398, 1980, ISSN: 0009-2614. DOI: https://doi.org/10.1016/0009-2614(80)80396-4. [Online]. Available: https://www.sciencedirect.com/science/article/pii/0009261480803964.

[72] P. Pulay, "Improved scf convergence acceleration," *J. Comp. Chem.*, vol. 3, no. 4, pp. 556–560, 1982. DOI: https://doi.org/10.1002/jcc.540030413. [Online]. Available: https://onlinelibrary.wiley.com/doi/abs/10.1002/jcc.540030413.

[73] G. B. Bacskay, "A quadratically convergent hartree—fock (qc-scf) method. application to closed shell systems," *Chem. Phys.*, vol. 61, no. 3, pp. 385–404, 1981, ISSN: 0301-0104. DOI: https://doi.org/10.1016/0301-0104(81)85156-7. [Online]. Available: https://www.sciencedirect.com/science/article/pii/0301010481851567.

[74] R. Hoffmann, "An extended hückel theory. i. hydrocarbons," *J. Chem. Phys.*, vol. 39, no. 6, pp. 1397–1412, Sep. 1963, ISSN: 0021-9606. DOI: 10.1063/1.1734456. [Online]. Available: https://doi.org/10.1063/1.1734456.

[75] S. Lehtola, "Assessment of initial guesses for self-consistent field calculations. superposition of atomic potentials: Simple yet efficient," *J. Chem. Theory Comput.*, vol. 15, no. 3, pp. 1593–1604, 2019, PMID: 30653322. DOI: 10.1021/acs.jctc.8b01089. [Online]. Available: https://doi.org/10.1021/acs.jctc.8b01089.

[76] C. Møller and M. S. Plesset, "Note on an approximation treatment for many-electron systems," *Phys. Rev.*, vol. 46, pp. 618–622, 7 Oct. 1934. DOI: 10.1103/PhysRev.46.618. [Online]. Available: https://link.aps.org/doi/10.1103/PhysRev.46.618.

[77] N. Handy, "Multi-root configuration interaction calculations," *Chem. Phys. Lett.*, vol. 74, no. 2, pp. 280–283, 1980, ISSN: 0009-2614. DOI: https://doi.org/10.1016/0009-2614(80)85158-X. [Online]. Available: https://www.sciencedirect.com/science/article/pii/000926148085158X.

[78] K. Raghavachari, G. W. Trucks, J. A. Pople, and M. Head-Gordon, "A fifth-order perturbation comparison of electron correlation theories," *Chem. Phys. Lett.*, vol. 157, pp. 479–483, 6 May 1989. DOI: 10.1016/s0009-2614(89)87395-6. [Online]. Available: http://dx.doi.org/10.1016/s0009-2614(89)87395-6.

[79] J. B. Anderson, "A random-walk simulation of the schrödinger equation: H+3," *J. Chem. Phys.*, vol. 63, no. 4, pp. 1499–1503, Aug. 1975, ISSN: 0021-9606. DOI: 10.1063/1.431514. [Online]. Available: https://doi.org/10.1063/1.431514.

[80] J. B. Anderson, "Quantum chemistry by random walk," *J. Chem. Phys.*, vol. 65, p. 4121, 1976. DOI: 10.1063/1.441022.

[81] D. M. Ceperley and B. J. Alder, "Ground state of the electron gas by a stochastic method," *Phys. Rev. Lett.*, vol. 45, pp. 566–569, 7 Aug. 1980. DOI: 10.1103/PhysRevLett.45.566. [Online]. Available: https://link.aps.org/doi/10.1103/PhysRevLett.45.566.

[82] A. Benali, H. Shin, and O. Heinonen, "Quantum Monte Carlo benchmarking of large noncovalent complexes in the L7 benchmark set," *J. Chem. Phys.*, vol. 153, no. 19, p. 194 113, 2020, ISSN: 0021-9606. DOI: 10.1063/5.0026275. [Online]. Available: https://doi.org/10.1063/5.0026275.

[83] Y. S. Al-Hamdani *et al.*, "Interactions between large molecules pose a puzzle for reference quantum mechanical methods," *Nat. Commun.*, vol. 12, p. 3927, 2021. DOI: 10.1038/s41467-021-24119-3.

[84] F. Becca and S. Sorella, *Quantum Monte Carlo Approaches for Correlated Systems*. Cambridge University Press, 2017.

[85] J. Gubernatis, N. Kawashima, and P. Werner, *Quantum Monte Carlo Methods: Algorithms for Lattice Models*. Cambridge University Press, 2016.

[86] R. M. Martin, L. Reining, and D. M. Ceperley, *Interacting Electrons: Theory and Computational Approaches*. Cambridge University Press, 2016.

[87] G. H. Booth, A. J. Thom, and A. Alavi, "Fermion monte carlo without fixed nodes: A game of life, death, and annihilation in slater determinant space," *J. Chem. Phys.*, vol. 131, p. 054 106, 2009. DOI: 10.1063/1.3193710.

[88] D. Cleland, G. H. Booth, and A. Alavi, "Communications: Survival of the fittest: Accelerating convergence in full configuration-interaction quantum monte carlo," *J. Chem. Phys.*, vol. 132, p. 041 103, 2010. DOI: 10.1063/1.3302277.

[89] D. Ceperley, G. Chester, and M. Kalos, "Monte carlo simulation of a many-fermion study," *Phys. Rev. B*, vol. 16, p. 3081, 1977. DOI: 10.1103/PhysRevB.16.3081.

[90] P. J. Reynolds, D. M. Ceperley, B. J. Alder, and J. Lester William A., "Fixed-node quantum monte carlo for molecules," *The Journal of Chemical Physics*, vol. 77, no. 11, pp. 5593–5603, Dec. 1982, ISSN: 0021-9606. DOI: 10.1063/1.443766. [Online]. Available: https://doi.org/10.1063/1.443766.

[91] W. Foulkes, L. Mitas, R. Needs, and G. Rajagopal, "Quantum monte carlo simulations of solids," *Rev. Mod. Phys.*, vol. 73, p. 33, 2001. DOI: 10.1103/RevModPhys.73.33.

[92] M. H. Kalos, D. Levesque, and L. Verlet, "Helium at zero temperature with hard-sphere and other forces," *Phys. Rev. A*, vol. 9, pp. 2178–2195, 5 May 1974. DOI: 10.1103/PhysRevA.9.2178. [Online]. Available: https://link.aps.org/doi/10.1103/PhysRevA.9.2178.

[93] B. L. Hammond, W. A. Lester, and P. J. Reynolds, *Monte Carlo Methods in Ab Initio Quantum Chemistry*. WORLD SCIENTIFIC, 1994. DOI: 10.1142/1170. [Online]. Available: https://www.worldscientific.com/doi/abs/10.1142/1170.

[94] D. Thouless, "Stability conditions and nuclear rotations in the hartree-fock theory," *Nucl. Phys.*, vol. 21, pp. 225–232, 1960, ISSN: 0029-5582. DOI: https://doi.org/10.1016/0029-5582(60)90048-1. [Online]. Available: https://www.sciencedirect.com/science/article/pii/0029558260900481.

[95] D. J. Thouless, "Vibrational states of nuclei in the random phase approximation," *Nucl. Phys.*, vol. 22, no. 1, pp. 78–95, 1961, ISSN: 0029-5582. DOI: https://doi.org/10.1016/0029-5582(61)90364-9. [Online]. Available: http://www.sciencedirect.com/science/article/pii/0029558261903649.

[96] J. Hubbard, "Calculation of partition functions," *Phys. Rev. Lett.*, vol. 3, p. 77, 1959. DOI: 10.1103/PhysRevLett.3.77.

[97] R. Stratonovich, "On a method of calculating quantum distribution functions," in *Sov. Phys. Dokl.*, vol. 2, 1957, p. 416.

[98] R. Balian and E. Brezin, "Nonunitary bogoliubov transformations and extension of wick's theorem," *Nuovo Cimento B*, vol. 64, pp. 37–55, 1969. DOI: 10.1007/BF02710281. [Online]. Available: https://doi.org/10.1007/BF02710281.

[99] S. Zhang, "Auxiliary-field quantum monte carlo for correlated electron systems," *Emergent Phenomena in Correlated Matter: Autumn School Organized by the Forschungszentrum Jülich and the German Research School for Simulation Sciences at Forschungszentrum Jülich 23-27 September 2013; Lecture Notes of the Autumn School Correlated Electrons 2013*, vol. 3, 2013.

[100] J. L. Weber, H. Vuong, R. A. Friesner, and D. R. Reichman, "Expanding the design space of constraints in auxiliary-field quantum monte carlo," *J. Chem. Theory Comput.*, vol. 19, no. 21, pp. 7567–7576, 2023, PMID: 37889331. DOI: 10.1021/acs.jctc.3c00654. [Online]. Available: https://doi.org/10.1021/acs.jctc.3c00654.

[101] T. E. Booth and J. E. Gubernatis, "Monte carlo determination of multiple extremal eigenpairs," *Phys. Rev. E*, vol. 80, 4 Oct. 2009, ISSN: 15393755. DOI: 10.1103/PhysRevE.80.046704.

[102] G. H. Golub and C. F. Van Loan, *Matrix Computations*, Third. The Johns Hopkins University Press, 1996.

[103] W. Kohn and L. J. Sham, "Self-consistent equations including exchange and correlation effects," *Phys. Rev.*, vol. 140, A1133, 4A Nov. 1965. DOI: 10.1103/PhysRev.140.A1133. [Online]. Available: https://link.aps.org/doi/10.1103/PhysRev.140.A1133.

[104] G. Kresse and J. Furthmüller, "Efficient iterative schemes for *ab initio* total-energy calculations using a plane-wave basis set," *Phys. Rev. B*, vol. 54, p. 11 169, 16 Oct. 1996. DOI: 10.1103/PhysRevB.54.11169.

[105] G. Kresse and D. Joubert, "From ultrasoft pseudopotentials to the projector augmented-wave method," *Phys. Rev. B*, vol. 59, pp. 1758–1775, 3 Jan. 1999. DOI: 10.1103/PhysRevB.59.1758. [Online]. Available: https://link.aps.org/doi/10.1103/PhysRevB.59.1758.

[106] M.-C. Kim, H. Park, S. Son, E. Sim, and K. Burke, "Improved dft potential energy surfaces via improved densities," *J. Phys. Chem. Lett.*, vol. 6, no. 19, pp. 3802–3807, 2015, PMID: 26722874. DOI: 10.1021/acs.jpclett.5b01724. [Online]. Available: https://doi.org/10.1021/acs.jpclett.5b01724.

[107] A. J. Cohen, P. Mori-Sánchez, and W. Yang, "Insights into current limitations of density functional theory," *Science*, vol. 321, no. 5890, pp. 792–794, 2008. DOI: 10.1126/science.1158722.

[108] J. P. Perdew and K. Schmidt, "Jacob's ladder of density functional approximations for the exchange-correlation energy," *AIP Conf. Proc.*, vol. 577, no. 1, pp. 1–20, 2001. DOI: 10.1063/1.1390175. eprint: https://aip.scitation.org/doi/pdf/10.1063/1.1390175. [Online]. Available: https://aip.scitation.org/doi/abs/10.1063/1.1390175.

[109] R. Nagai, R. Akashi, and O. Sugino, "Completing density functional theory by machine learning hidden messages from molecules," *NPJ Comput. Mater.*, vol. 6, no. 1, 2020. DOI: 10.1038/s41524-020-0310-0.

[110] R. Pederson, B. Kalita, and K. Burke, "Machine learning and density functional theory," *Nat. Rev. Phys.*, vol. 4, no. 6, pp. 357–358, 2022. DOI: 10.1038/s42254-022-00470-2. [Online]. Available: https://doi.org/10.1038/s42254-022-00470-2.

[111] J. Behler and M. Parrinello, "Generalized neural-network representation of high-dimensional potential-energy surfaces," *Phys. Rev. Lett.*, vol. 98, p. 146 401, 14 Apr. 2007. DOI: 10.1103/PhysRevLett.98.146401. [Online]. Available: https://link.aps.org/doi/10.1103/PhysRevLett.98.146401.

[112] M. S. Chen, J. Lee, H.-Z. Ye, T. C. Berkelbach, D. R. Reichman, and T. E. Markland, "Data-efficient machine learning potentials from transfer learning of periodic correlated electronic structure methods: Liquid water at afqmc, ccsd, and ccsd(t) accuracy," *J. Chem. Theory Comput.*, vol. 0, no. 0, null, 0, PMID: 36730728. DOI: 10.1021/acs.jctc.2c01203. [Online]. Available: https://doi.org/10.1021/acs.jctc.2c01203.

[113] A. A. Holmes, N. M. Tubman, and C. J. Umrigar, "Heat-bath configuration interaction: An efficient selected configuration interaction algorithm inspired by heat-bath sampling," *J. Chem. Theory Comput.*, vol. 12, no. 8, pp. 3674–3680, 2016, PMID: 27428771. DOI: 10.1021/acs.jctc.6b00407. [Online]. Available: https://doi.org/10.1021/acs.jctc.6b00407.

[114] S. Sharma, A. A. Holmes, G. Jeanmairet, A. Alavi, and C. J. Umrigar, "Semistochastic heat-bath configuration interaction method: Selected configuration interaction with semistochastic perturbation theory," *J. Chem. Theory Comput.*, vol. 13, no. 4, pp. 1595–1604, 2017, PMID: 28263594. DOI: 10.1021/acs.jctc.6b01028. [Online]. Available: https://doi.org/10.1021/acs.jctc.6b01028.

[115] M. Dash, S. Moroni, A. Scemama, and C. Filippi, "Perturbatively selected configuration-interaction wave functions for efficient geometry optimization in quantum monte carlo," *J. Chem. Theory Comput.*, vol. 14, no. 8, pp. 4176–4182, 2018, PMID: 29953810. DOI: 10.1021/acs.jctc.8b00393. [Online]. Available: https://doi.org/10.1021/acs.jctc.8b00393.

[116] K. Ghanem, K. Guther, and A. Alavi, "The adaptive shift method in full configuration interaction quantum monte carlo: Development and applications," *J. Chem. Phys.*, vol. 153, no. 22, p. 224 115, 2020. DOI: 10.1063/5.0032617.

[117] Y. Yao, E. Giner, J. Li, J. Toulouse, and C. J. Umrigar, "Almost exact energies for the gaussian-2 set with the semistochastic heat-bath configuration interaction method," *J. Chem. Phys.*, vol. 153, no. 12, p. 124 117, 2020. DOI: 10.1063/5.0018577. eprint: https://doi.org/10.1063/5.0018577. [Online]. Available: https://doi.org/10.1063/5.0018577.

[118] G. D. Purvis and R. J. Bartlett, "A full coupled-cluster singles and doubles model: The inclusion of disconnected triples," *J. Chem. Phys.*, vol. 76, no. 4, pp. 1910–1918, 1982. DOI: 10.1063/1.443164. [Online]. Available: https://doi.org/10.1063/1.443164.

[119] R. J. Bartlett and M. Musiał, "Coupled-cluster theory in quantum chemistry," *Rev. Mod. Phys.*, vol. 79, p. 291, 2007. DOI: 10.1103/RevModPhys.79.291.

[120] Y. J. Bomble, J. F. Stanton, M. Kállay, and J. Gauss, "Coupled-cluster methods including noniterative corrections for quadruple excitations," *J. Chem. Phys.*, vol. 123, no. 5, p. 054 101, 2005. DOI: 10.1063/1.1950567. [Online]. Available: https://doi.org/10.1063/1.1950567.

[121] M. E. Harding, J. Vázquez, B. Ruscic, A. K. Wilson, J. Gauss, and J. F. Stanton, "High-accuracy extrapolated ab initio thermochemistry. iii. additional improvements and overview," *J. Chem. Phys.*, vol. 128, no. 11, p. 114 111, 2008. DOI: 10.1063/1.2835612. [Online]. Available: https://doi.org/10.1063/1.2835612.

[122] S. R. White and R. L. Martin, "Ab initio quantum chemistry using the density matrix renormalization group," *J. Chem. Phys.*, vol. 110, no. 9, pp. 4127–4130, 1999. DOI: 10.1063/1.478295. [Online]. Available: https://doi.org/10.1063/1.478295.

[123] U. Schollwöck, "The density-matrix renormalization group," *Rev. Mod. Phys.*, vol. 77, pp. 259–315, 1 Apr. 2005. DOI: 10.1103/RevModPhys.77.259. [Online]. Available: https://link.aps.org/doi/10.1103/RevModPhys.77.259.

[124] G. K.-L. Chan and S. Sharma, "The density matrix renormalization group in quantum chemistry," *Annu. Rev. Phys. Chem.*, vol. 62, no. 1, pp. 465–481, 2011, PMID: 21219144. DOI: 10.1146/annurev-physchem-032210-103338. [Online]. Available: https://doi.org/10.1146/annurev-physchem-032210-103338.

[125] W. L. McMillan, "Ground state of liquid he 4," *Phys. Rev.*, vol. 138, A442, 1965. DOI: 10.1103/PhysRev.138.A442.

[126] N. Nemec, M. D. Towler, and R. J. Needs, "Benchmark all-electron ab initio quantum monte carlo calculations for small molecules," *J. Chem. Phys.*, vol. 132, no. 3, p. 034 111, 2010. DOI: 10.1063/1.3288054. [Online]. Available: https://doi.org/10.1063/1.3288054.

[127] L. A. Curtiss, K. Raghavachari, G. W. Trucks, and J. A. Pople, "Gaussian-2 theory for molecular energies of first- and second-row compounds," *J. Chem. Phys.*, vol. 94, no. 11, pp. 7221–7230, 1991. DOI: 10.1063/1.460205. [Online]. Available: https://doi.org/10.1063/1.460205.

[128] F. R. Petruzielo, J. Toulouse, and C. J. Umrigar, "Approaching chemical accuracy with quantum monte carlo," *J. Chem. Phys.*, vol. 136, no. 12, p. 124 116, 2012. DOI: 10.1063/1.3697846. eprint: https://doi.org/10.1063/1.3697846. [Online]. Available: https://doi.org/10.1063/1.3697846.

[129] D. Pfau, J. S. Spencer, A. G. D. G. Matthews, and W. M. C. Foulkes, "Ab initio solution of the many-electron schrödinger equation with deep neural networks," *Phys. Rev. Res.*, vol. 2, p. 033 429, 3 Sep. 2020. DOI: 10.1103/PhysRevResearch.2.033429. [Online]. Available: https://link.aps.org/doi/10.1103/PhysRevResearch.2.033429.

[130] L. Gerard, M. Scherbela, P. Marquetand, and P. Grohs, *Gold-standard solutions to the Schrödinger equation using deep learning: How much physics do we need?* 2022, arXiv:2205.09438. arXiv.org e-Print archive. https://arxiv.org/abs/2205.09438 (accessed June 24, 2023).

[131] J. Lee, F. D. Malone, and M. A. Morales, "Utilizing essential symmetry breaking in auxiliary-field quantum monte carlo: Application to the spin gaps of the c36 fullerene and an iron porphyrin model complex," *J. Chem. Theory Comput.*, vol. 16, no. 5, pp. 3019–3027, 2020, PMID: 32283932. DOI: 10.1021/acs.jctc.0c00055. [Online]. Available: https://doi.org/10.1021/acs.jctc.0c00055.

[132] J. E. Hirsch, "Two-dimensional hubbard model: Numerical simulation study," *Phys. Rev. B*, vol. 31, pp. 4403–4419, 7 Apr. 1985. DOI: 10.1103/PhysRevB.31.4403. [Online]. Available: https://link.aps.org/doi/10.1103/PhysRevB.31.4403.

[133] M. Motta and S. Zhang, "Ab initio computations of molecular systems by the auxiliary-field quantum monte carlo method," *WIRES Comput. Mol. Sci.*, vol. 8, no. 5, e1364, 2018. DOI: https://doi.org/10.1002/wcms.1364. eprint: https://wires.onlinelibrary.wiley.com/doi/pdf/10.1002/wcms.1364. [Online]. Available: https://wires.onlinelibrary.wiley.com/doi/abs/10.1002/wcms.1364.

[134] H. Shi and S. Zhang, "Symmetry in auxiliary-field quantum monte carlo calculations," *Phys. Rev. B*, vol. 88, p. 125 132, 12 Sep. 2013. DOI: 10.1103/PhysRevB.88.125132. [Online]. Available: https://link.aps.org/doi/10.1103/PhysRevB.88.125132.

[135] C.-C. Chang, B. M. Rubenstein, and M. A. Morales, "Auxiliary-field-based trial wave functions in quantum monte carlo calculations," *Phys. Rev. B*, vol. 94, p. 235 144, 23 Dec. 2016. DOI: 10.1103/PhysRevB.94.235144. [Online]. Available: https://link.aps.org/doi/10.1103/PhysRevB.94.235144.

[136] W. J. Huggins, B. A. O'Gorman, N. C. Rubin, D. R. Reichman, R. Babbush, and J. Lee, "Unbiasing fermionic quantum monte carlo with a quantum computer," *Nature*, vol. 603, pp. 416–420, 2022. DOI: 10.1038/s41586-021-04351-z. [Online]. Available: https://doi.org/10.1038/s41586-021-04351-z.

[137] Q. Sun *et al.*, "Pyscf: The python-based simulations of chemistry framework," *WIRES Comput. Mol. Sci.*, vol. 8, no. 1, e1340, 2018. DOI: https://doi.org/10.1002/wcms.1340. [Online]. Available: https://wires.onlinelibrary.wiley.com/doi/abs/10.1002/wcms.1340.

[138] H. Trotter, "On the product of semi-groups of operators," *Proc. Am. Math. Soc.*, vol. 10, pp. 545–551, 1959.

[139] M. Suziki, "Relationship between d-dimensional quantal spin systems and (d+1)-dimensional ising systemsequivalence, critical exponents and systematic approximants of the partition function and spin correlations," *Prog. Theor. Phys.*, vol. 56, pp. 1454–1469, 1976.

[140] M. Calandra Buonaura and S. Sorella, "Numerical study of the two-dimensional heisenberg model using a green function monte carlo technique with a fixed number of walkers," *Phys. Rev. B*, vol. 57, pp. 11 446–11 456, 18 May 1998. DOI: 10.1103/PhysRevB.57.11446. [Online]. Available: https://link.aps.org/doi/10.1103/PhysRevB.57.11446.

[141] P. E. Blöchl, "Projector augmented-wave method," *Phys. Rev. B*, vol. 50, p. 17 953, 1994. DOI: 10.1103/PhysRevB.50.17953.

[142] J. J. Eriksen *et al.*, "The ground state electronic energy of benzene," *J. Phys. Chem. Lett.*, vol. 11, no. 20, pp. 8922–8929, 2020, PMID: 33022176. DOI: 10.1021/acs.jpclett.0c02621.

[143] P. R. C. Kent *et al.*, "QMCPACK: Advances in the development, efficiency, and application of auxiliary field and real-space variational and diffusion quantum Monte Carlo," *J. Chem. Phys.*, vol. 152, no. 17, p. 174 105, May 2020, ISSN: 0021-9606. DOI: 10.1063/5.0004860. [Online]. Available: https://doi.org/10.1063/5.0004860.

[144] J. Kim *et al.*, "Qmcpack: An open source ab initio quantum monte carlo package for the electronic structure of atoms, molecules and solids," *J. Phys. Cond. Matter*, vol. 30, no. 19, p. 195 901, Apr. 2018. DOI: 10.1088/1361-648X/aab9c3. [Online]. Available: https://dx.doi.org/10.1088/1361-648X/aab9c3.

[145] B. Temelso, K. A. Archer, and G. C. Shields, "Benchmark structures and binding energies of small water clusters with anharmonicity corrections," *J. Phys. Chem. A*, vol. 115, no. 43, pp. 12 034–12 046, 2011, PMID: 21910428. DOI: 10.1021/jp2069489. eprint: https://doi.org/10.1021/jp2069489. [Online]. Available: https://doi.org/10.1021/jp2069489.

[146] J. Čížek, "On the correlation problem in atomic and molecular systems. calculation of wavefunction components in ursell-type expansion using quantum-field theoretical methods," *J. Chem. Phys.*, vol. 45, pp. 4256–4266, 11 Dec. 1966. DOI: 10.1063/1.1727484. [Online]. Available: http://dx.doi.org/10.1063/1.1727484.

[147] J. Čížek and J. Paldus, "Correlation problems in atomic and molecular systems iii. rederivation of the coupled-pair many-electron theory using the traditional quantum chemical methodst," *Int. J. Quant. Chem.*, vol. 5, pp. 359–379, 4 Jul. 1971. DOI: 10.1002/qua.560050402. [Online]. Available: http://dx.doi.org/10.1002/qua.560050402.

[148] G. H. Booth, A. Grüneis, G. Kresse, and A. Alavi, "Towards an exact description of electronic wavefunctions in real solids," *Nature*, vol. 493, p. 365, 2013. DOI: 10.1038/nature11770.

[149] D. Cleland, G. H. Booth, C. Overy, and A. Alavi, "Taming the first-row diatomics: A full configuration interaction quantum monte carlo study," *J. Chem. Theory Comput.*, vol. 8, no. 11, pp. 4138–4152, 2012. DOI: 10.1021/ct300504f.

[150] F. R. Petruzielo, A. A. Holmes, H. J. Changlani, M. P. Nightingale, and C. J. Umrigar, "Semistochastic projector monte carlo method," *Phys. Rev. Lett.*, vol. 109, 23 Dec. 2012. DOI: 10.1103/physrevlett.109.230201. [Online]. Available: http://dx.doi.org/10.1103/physrevlett.109.230201.

[151] A. A. Holmes, H. J. Changlani, and C. J. Umrigar, "Efficient heat-bath sampling in fock space," *J. Chem. Theory Comput.*, vol. 12, pp. 1561–1571, 4 Apr. 2016. DOI: 10.1021/acs.jctc.5b01170. [Online]. Available: http://dx.doi.org/10.1021/acs.jctc.5b01170.

[152] N. M. Tubman, J. Lee, T. Y. Takeshita, M. Head-Gordon, and K. B. Whaley, "A deterministic alternative to the full configuration interaction quantum monte carlo method," *J. Chem. Phys.*, vol. 145, 4 Jul. 2016. DOI: 10.1063/1.4955109. [Online]. Available: http://dx.doi.org/10.1063/1.4955109.

[153] N. M. Tubman, C. D. Freeman, D. S. Levine, D. Hait, M. Head-Gordon, and K. B. Whaley, "Modern approaches to exact diagonalization and selected configuration interaction with the adaptive sampling ci method," *J. Chem. Theory Comput.*, vol. 16, pp. 2139–2159, 4 Apr. 2020. DOI: 10.1021/acs.jctc.8b00536. [Online]. Available: http://dx.doi.org/10.1021/acs.jctc.8b00536.

[154] D. S. Levine, D. Hait, N. M. Tubman, S. Lehtola, K. B. Whaley, and M. Head-Gordon, "Casscf with extremely large active spaces using the adaptive sampling configuration interaction method," *J. Chem. Theory Comput.*, vol. 16, pp. 2340–2354, 4 Apr. 2020. DOI: 10.1021/acs.jctc.9b01255. [Online]. Available: http://dx.doi.org/10.1021/acs.jctc.9b01255.

[155] W. Liu and M. R. Hoffmann, "Ici: Iterative ci toward full ci," *J. Chem. Theory Comput.*, vol. 12, pp. 1169–1178, 3 Mar. 2016. DOI: 10.1021/acs.jctc.5b01099. [Online]. Available: http://dx.doi.org/10.1021/acs.jctc.5b01099.

[156] N. Zhang, W. Liu, and M. R. Hoffmann, "Iterative configuration interaction with selection," *J. Chem. Theory Comput.*, vol. 16, pp. 2296–2316, 4 Apr. 2020. DOI: 10.1021/acs.jctc.9b01200. [Online]. Available: http://dx.doi.org/10.1021/acs.jctc.9b01200.

[157] J. J. Eriksen, F. Lipparini, and J. Gauss, "Virtual orbital many-body expansions: A possible route towards the full configuration interaction limit," *J. Phys. Chem. Lett.*, vol. 8, pp. 4633–4639, 18 Sep. 2017. DOI: 10.1021/acs.jpclett.7b02075. [Online]. Available: http://dx.doi.org/10.1021/acs.jpclett.7b02075.

[158] J. J. Eriksen and J. Gauss, "Many-body expanded full configuration interaction. i. weakly correlated regime," *J. Chem. Theory Comput.*, vol. 14, pp. 5180–5191, 10 Oct. 2018. DOI: 10.1021/acs.jctc.8b00680. [Online]. Available: http://dx.doi.org/10.1021/acs.jctc.8b00680.

[159] J. J. Eriksen and J. Gauss, "Many-body expanded full configuration interaction. ii. strongly correlated regime," *J. Chem. Theory Comput.*, vol. 15, pp. 4873–4884, 9 Sep. 2019. DOI: 10.1021/acs.jctc.9b00456. [Online]. Available: http://dx.doi.org/10.1021/acs.jctc.9b00456.

[160] J. J. Eriksen and J. Gauss, "Generalized many-body expanded full configuration interaction theory," *J. Phys. Chem. Lett.*, vol. 10, pp. 7910–7915, 24 Dec. 2019. DOI: 10.1021/acs.jpclett.9b02968. [Online]. Available: http://dx.doi.org/10.1021/acs.jpclett.9b02968.

[161] D. Feller and D. A. Dixon, "Extended benchmark studies of coupled cluster theory through triple excitations," *J. Chem. Phys.*, vol. 115, no. 8, pp. 3484–3496, 2001. DOI: 10.1063/1.1388045. [Online]. Available: https://doi.org/10.1063/1.1388045.

[162] T. Gruber, K. Liao, T. Tsatsoulis, F. Hummel, and A. Grüneis, "Applying the coupled-cluster ansatz to solids and surfaces in the thermodynamic limit," *Phys. Rev. X*, vol. 8, 2 May 2018. DOI: 10.1103/physrevx.8.021043. [Online]. Available: http://dx.doi.org/10.1103/physrevx.8.021043.

[163] A. Grüneis, S. Hirata, Y.-y. Ohnishi, and S. Ten-no, "Perspective: Explicitly correlated electronic structure theory for complex systems," *J. Chem. Phys.*, vol. 146, p. 080 901, 2017. DOI: 10.1063/1.4976974.

[164] I. Y. Zhang and A. Grüneis, "Coupled cluster theory in materials science," *Front. Mater.*, vol. 6, 2019, ISSN: 2296-8016. DOI: 10.3389/fmats.2019.00123. [Online]. Available: https://www.frontiersin.org/articles/10.3389/fmats.2019.00123.

[165] A. Irmler, A. Gallo, and A. Grüneis, "Focal-point approach with pair-specific cusp correction for coupled-cluster theory," *J. Chem. Phys.*, vol. 154, 23 Jun. 2021. DOI: 10.1063/5.0050054. [Online]. Available: http://dx.doi.org/10.1063/5.0050054.

[166] J. McClain, Q. Sun, G. K.-L. Chan, and T. C. Berkelbach, "Gaussian-based coupled-cluster theory for the ground-state and band structure of solids," *J. Chem. Theory Comput.*, vol. 13, no. 3, pp. 1209–1218, 2017, PMID: 28218843. DOI: 10.1021/acs.jctc.7b00049. [Online]. Available: https://doi.org/10.1021/acs.jctc.7b00049.

[167] A. J. W. Thom, "Stochastic coupled cluster theory," *Phys. Rev. Lett.*, vol. 105, 26 Dec. 2010. DOI: 10.1103/physrevlett.105.263004. [Online]. Available: http://dx.doi.org/10.1103/physrevlett.105.263004.

[168] M.-A. Filip, C. J. C. Scott, and A. J. W. Thom, "Multireference stochastic coupled cluster," *J. Chem. Theory Comput.*, vol. 15, pp. 6625–6635, 12 Dec. 2019. DOI: 10.1021/acs.jctc.9b00741. [Online]. Available: http://dx.doi.org/10.1021/acs.jctc.9b00741.

[169] M.-A. Filip and A. J. W. Thom, "A stochastic approach to unitary coupled cluster," *J. Chem. Phys.*, vol. 153, 21 Dec. 2020. DOI: 10.1063/5.0026141. [Online]. Available: http://dx.doi.org/10.1063/5.0026141.

[170] P. P. Jun Shen, "Biorthogonal moment expansions in coupled-cluster theory: Review of key concepts and merging the renormalized and active-space coupled-cluster methods," *Chem. Phys.*, vol. 401, pp. 180–202, 2012, ISSN: 0301-0104. DOI: https://doi.org/10.1016/j.chemphys.2011.11.033. [Online]. Available: https://www.sciencedirect.com/science/article/pii/S0301010411005283.

[171] J. E. Deustua, J. Shen, and P. Piecuch, "Converging high-level coupled-cluster energetics by monte carlo sampling and moment expansions," *Phys. Rev. Lett.*, vol. 119, 22 Nov. 2017. DOI: 10.1103/physrevlett.119.223003. [Online]. Available: http://dx.doi.org/10.1103/physrevlett.119.223003.

[172] A. Chakraborty, S. H. Yuwono, J. E. Deustua, J. Shen, and P. Piecuch, "Benchmarking the semi-stochastic cc(p;q) approach for singlet–triplet gaps in biradicals," *J. Chem. Phys.*, vol. 157, p. 134 101, 13 Oct. 2022. DOI: 10.1063/5.0100165. [Online]. Available: http://dx.doi.org/10.1063/5.0100165.

[173] R. Jastrow, "Many-body problem with strong forces," *Phys. Rev.*, vol. 98, pp. 1479–1484, 5 Jun. 1955. DOI: 10.1103/physrev.98.1479. [Online]. Available: http://dx.doi.org/10.1103/physrev.98.1479.

[174] K. E. Schmidt and J. W. Moskowitz, "Correlated monte carlo wave functions for the atoms he through ne," *J. Chem. Phys.*, vol. 93, pp. 4172–4178, 6 Sep. 1990. DOI: 10.1063/1.458750. [Online]. Available: http://dx.doi.org/10.1063/1.458750.

[175] N. D. Drummond, M. D. Towler, and R. J. Needs, "Jastrow correlation factor for atoms, molecules, and solids," *Phys. Rev. B*, vol. 70, 23 Dec. 2004. DOI: 10.1103/physrevb.70.235119. [Online]. Available: http://dx.doi.org/10.1103/physrevb.70.235119.

[176] J. C. Grossman, "Benchmark quantum monte carlo calculations," *J. Chem. Phys.*, vol. 117, pp. 1434–1440, 4 Jul. 2002. DOI: 10.1063/1.1487829. [Online]. Available: http://dx.doi.org/10.1063/1.1487829.

[177] S. Manten and A. Lüchow, "On the accuracy of the fixed-node diffusion quantum monte carlo method," *J. Chem. Phys.*, vol. 115, pp. 5362–5366, 12 Sep. 2001. DOI: 10.1063/1.1394757. [Online]. Available: http://dx.doi.org/10.1063/1.1394757.

[178] P. López Ríos, A. Ma, N. D. Drummond, M. D. Towler, and R. J. Needs, "Inhomogeneous backflow transformations in quantum monte carlo calculations," *Phys. Rev. E*, vol. 74, 6 Dec. 2006. DOI: 10.1103/physreve.74.066701. [Online]. Available: http://dx.doi.org/10.1103/physreve.74.066701.

[179] M. Casula and S. Sorella, "Geminal wave functions with jastrow correlation: A first application to atoms," *J. Chem. Phys.*, vol. 119, pp. 6500–6511, 13 Oct. 2003. DOI: 10.1063/1.1604379. [Online]. Available: http://dx.doi.org/10.1063/1.1604379.

[180] M. Bajdich, L. Mitas, G. Drobný, L. K. Wagner, and K. E. Schmidt, "Pfaffian pairing wave functions in electronic-structure quantum monte carlo simulations," *Phys. Rev. Lett.*, vol. 96, 13 Apr. 2006. DOI: 10.1103/physrevlett.96.130201. [Online]. Available: http://dx.doi.org/10.1103/physrevlett.96.130201.

[181] W. Purwanto, W. A. Al-Saidi, H. Krakauer, and S. Zhang, "Eliminating spin contamination in auxiliary-field quantum monte carlo: Realistic potential energy curve of f2," *J. Chem. Phys.*, vol. 128, p. 114 309, 11 Mar. 2008. DOI: 10.1063/1.2838983. [Online]. Available: http://dx.doi.org/10.1063/1.2838983.

[182] W. A. Al-Saidi, H. Krakauer, and S. Zhang, "Auxiliary-field quantum Monte Carlo study of first- and second-row post-d elements," *J. Chem. Phys.*, vol. 125, no. 15, p. 154 110, Oct. 2006, ISSN: 0021-9606. DOI: 10.1063/1.2357917. [Online]. Available: https://doi.org/10.1063/1.2357917.

[183] W. A. Al-Saidi, H. Krakauer, and S. Zhang, "A study of h+h2 and several h-bonded molecules by phaseless auxiliary-field quantum monte carlo with plane wave and gaussian basis sets," *J. Chem. Phys.*, vol. 126, p. 194 105, 19 May 2007. DOI: 10.1063/1.2735296. [Online]. Available: http://dx.doi.org/10.1063/1.2735296.

[184] W. Purwanto, H. Krakauer, and S. Zhang, "Pressure-induced diamond to β-tin transition in bulk silicon: A quantum monte carlo study," *Phys. Rev. B*, vol. 80, 21 Dec. 2009. DOI: 10.1103/physrevb.80.214116. [Online]. Available: http://dx.doi.org/10.1103/physrevb.80.214116.

[185] S. Zhang, "Finite-temperature monte carlo calculations for systems with fermions," *Phys. Rev. Lett.*, vol. 83, pp. 2777–2780, 14 Oct. 1999. DOI: 10.1103/physrevlett.83.2777. [Online]. Available: http://dx.doi.org/10.1103/physrevlett.83.2777.

[186] S. Zhang, "Finite-temperature calculations of correlated electron systems," *Comput. Phys. Commun.*, vol. 127, pp. 150–155, 1 May 2000. DOI: 10.1016/s0010-4655(00)00029-1. [Online]. Available: http://dx.doi.org/10.1016/s0010-4655(00)00029-1.

[187] Y. Liu, M. Cho, and B. Rubenstein, "Ab initio finite temperature auxiliary field quantum monte carlo," *J. Chem. Theory Comput.*, vol. 14, no. 9, pp. 4722–4732, 2018. DOI: 10.1021/acs.jctc.8b00569.

[188] C. Gilbreth, S. Jensen, and Y. Alhassid, "Reducing the complexity of finite-temperature auxiliary-field quantum monte carlo," *Comput. Phys. Commun.*, vol. 264, p. 107 952, Jul. 2021. DOI: 10.1016/j.cpc.2021.107952. [Online]. Available: http://dx.doi.org/10.1016/j.cpc.2021.107952.

[189] J. Lee, M. A. Morales, and F. D. Malone, "A phaseless auxiliary-field quantum monte carlo perspective on the uniform electron gas at finite temperatures: Issues, observations, and benchmark study," *J. Chem. Phys.*, vol. 154, 6 Feb. 2021. DOI: 10.1063/5.0041378. [Online]. Available: http://dx.doi.org/10.1063/5.0041378.

[190] Z.-Y. Xiao, H. Shi, and S. Zhang, "Interfacing branching random walks with metropolis sampling: Constraint release in auxiliary-field quantum monte carlo," *J. Chem. Theory Comput.*, vol. 19, no. 19, pp. 6782–6795, 2023, PMID: 37661928. DOI: 10.1021/acs.jctc.3c00521. [Online]. Available: https://doi.org/10.1021/acs.jctc.3c00521.

[191] C. J. Umrigar, M. P. Nightingale, and K. J. Runge, "A diffusion monte carlo algorithm with very small time-step errors," *J. Chem. Phys.*, vol. 99, no. 4, pp. 2865–2890, 1993. DOI: 10.1063/1.465195. [Online]. Available: https://doi.org/10.1063/1.465195.

[192] A. Zen, S. Sorella, M. J. Gillan, A. Michaelides, and D. Alfè, "Boosting the accuracy and speed of quantum monte carlo: Size consistency and time step," *Phys. Rev. B*, vol. 93, p. 241 118, 2016. DOI: 10.1103/PhysRevB.93.241118.

[193] T. A. Anderson, M. C. Per, and C. J. Umrigar, *Reducing the time-step errors in diffusion monte carlo*, arXiv:physics.chem-ph/2312.01526. arXiv.org ePrint archive. https://arxiv.org/abs/2312.01526 (accessed Feb 15, 2024), 2023.

[194] Y. Saad, *Iterative Methods for Sparse Linear Systems* (Other Titles in Applied Mathematics), Second. SIAM, 2003, ISBN: 978-0-89871-534-7. DOI: 10.1137/1.9780898718003. [Online]. Available: http://www-users.cs.umn.edu/%5C~%7B%7Dsaad/IterMethBook%5C_2ndEd.pdf.

[195] H. Tal-Ezer and R. Kosloff, "An accurate and efficient scheme for propagating the time dependent schrödinger equation," *J. Chem. Phys.*, vol. 81, pp. 3967–3971, 9 Nov. 1984. DOI: 10.1063/1.448136. [Online]. Available: http://dx.doi.org/10.1063/1.448136.

[196] Z. Sukurma. "Data for: Large time step auxiliary-field qauntum monte carlo." doi:10.5281/zenodo.10405030. https://doi.org/10.5281/zenodo.10405030. (2023).

[197] G. Herzberg and K. P. Huber, *Molecular Spectra and Molecular Structure*, Second. Malabar, Fla. : R.E. Krieger Pub. Co., 1979, ISBN: 0894642693. DOI: 10.1007/978-1-4757-0961-2.

[198] T. Schäfer, A. Irmler, A. Gallo, and A. Grüneis, *Understanding discrepancies of wavefunction theories for large molecules*, arXiv:physics.chem-ph/2407.01442. arXiv.org ePrint archive. url=https://arxiv.org/abs/2407.01442 (accessed Oct 06, 2024), 2024.

[199] N. Masios, A. Irmler, T. Schäfer, and A. Grüneis, "Averting the infrared catastrophe in the gold standard of quantum chemistry," *Phys. Rev. Lett.*, vol. 131, p. 186 401, 18 2023. DOI: 10.1103/PhysRevLett.131.186401.

[200] M. Motta, J. Shee, S. Zhang, and G. K.-L. Chan, "Efficient ab initio auxiliary-field quantum monte carlo calculations in gaussian bases via low-rank tensor decomposition," *J. Chem. Theory Comput.*, vol. 15, no. 6, pp. 3510–3521, 2019. DOI: 10.1021/acs.jctc.8b00996.

[201] I. Shavitt and R. J. Bartlett, *Many-Body Methods in Chemistry and Physics: MBPT and Coupled-Cluster Theory* (Cambridge Molecular Science). Cambridge University Press, 2009.

[202] K. Schmid, Zheng Ren-Rong, F. Grümmer, and A. Faessler, "Beyond symmetry-projected quasi-particle mean fields: A new variational procedure for nuclear structure calculations," *Nucl. Phys. A*, vol. 499, no. 1, pp. 63–92, 1989, ISSN: 0375-9474. DOI: https://doi.org/10.1016/0375-9474(89)90269-8. [Online]. Available: https://www.sciencedirect.com/science/article/pii/0375947489902698.

[203] K. Schmid, "On the use of general symmetry-projected hartree–fock–bogoliubov configurations in variational approaches to the nuclear many-body problem," *Prog. Part. Nucl. Phys.*, vol. 52, no. 2, pp. 565–633, 2004, ISSN: 0146-6410. DOI: https://doi.org/10.1016/j.ppnp.2004.02.001. [Online]. Available: https://www.sciencedirect.com/science/article/pii/S0146641004000134.

[204] C. A. Jiménez-Hoyos, R. Rodríguez-Guzmán, and G. E. Scuseria, "Multi-component symmetry-projected approach for molecular ground state correlations," *J. Chem. Phys.*, vol. 139, no. 20, p. 204 102, 2013, ISSN: 0021-9606. DOI: 10.1063/1.4832476. [Online]. Available: https://doi.org/10.1063/1.4832476.

[205] A. Ikawa, S. Yamamoto, and H. Fukutome, "Orbital optimization in the resonating hartree-fock approximation and its application to the one dimensional hubbard model," *J. Phys. Soc. Jpn*, vol. 62, no. 5, pp. 1653–1668, 1993. DOI: 10.1143/JPSJ.62.1653. [Online]. Available: https://doi.org/10.1143/JPSJ.62.1653.

[206] T. Jiang, B. O'Gorman, A. Mahajan, and J. Lee, "Unbiasing fermionic auxiliary-field quantum monte carlo with matrix product state trial wavefunctions," *Phys. Rev. Res.*, vol. 7, p. 013 038, 1 Jan. 2025. DOI: 10.1103/PhysRevResearch.7.013038. [Online]. Available: https://link.aps.org/doi/10.1103/PhysRevResearch.7.013038.

[207] M. Amsler *et al.*, "Classical and quantum trial wave functions in auxiliary-field quantum Monte Carlo applied to oxygen allotropes and a CuBr2 model system," *J. Chem. Phys.*, vol. 159, no. 4, p. 044 119, 2023. DOI: 10.1063/5.0146934. [Online]. Available: https://doi.org/10.1063/5.0146934.

[208] M. Kiser *et al.*, "Classical and quantum cost of measurement strategies for quantum-enhanced auxiliary field quantum monte carlo," *New J. Phys.*, vol. 26, no. 3, p. 033 022, 2024. DOI: 10.1088/1367-2630/ad2f67. [Online]. Available: https://dx.doi.org/10.1088/1367-2630/ad2f67.

[209] M. Kiser, M. Beuerle, and F. I. Šimkovic, "Contextual subspace auxiliary-field quantum monte carlo: Improved bias with reduced quantum resources," *J. Chem. Theory Comput.*, vol. 21, no. 5, pp. 2256–2271, 2025, PMID: 39976529. DOI: 10.1021/acs.jctc.4c01280. [Online]. Available: https://doi.org/10.1021/acs.jctc.4c01280.

[210] M. Qin, H. Shi, and S. Zhang, "Coupling quantum monte carlo and independent-particle calculations: Self-consistent constraint for the sign problem based on the density or the density matrix," *Phys. Rev. B*, vol. 94, p. 235 119, 23 Dec. 2016. DOI: 10.1103/PhysRevB.94.235119. [Online]. Available: https://link.aps.org/doi/10.1103/PhysRevB.94.235119.

[211] R. Dutta, G. P. Chen, T. M. Henderson, and G. E. Scuseria, "Construction of linearly independent non-orthogonal AGP states," *J. Chem. Phys.*, vol. 154, no. 11, p. 114 112, 2021. DOI: 10.1063/5.0045006. [Online]. Available: https://doi.org/10.1063/5.0045006.

[212] C. Sun, F. Gao, and G. E. Scuseria, "Selected nonorthogonal configuration interaction with compressed single and double excitations," *J. Chem. Theory Comput.*, vol. 20, no. 9, pp. 3741–3748, 2024. DOI: 10.1021/acs.jctc.4c00240. [Online]. Available: https://doi.org/10.1021/acs.jctc.4c00240.

[213] Y. Chen, L. Zhang, W. E, and R. Car, "Hybrid auxiliary field quantum monte carlo for molecular systems," *J. Chem. Theory Comput.*, vol. 19, no. 14, pp. 4484–4493, 2023. DOI: 10.1021/acs.jctc.3c00038. [Online]. Available: https://doi.org/10.1021/acs.jctc.3c00038.

[214] W. Purwanto, W. A. Al-Saidi, H. Krakauer, and S. Zhang, "Eliminating spin contamination in auxiliary-field quantum monte carlo: Realistic potential energy curve of f2," *J. Chem. Phys.*, vol. 128, no. 11, p. 114 309, Mar. 2008, ISSN: 0021-9606. DOI: 10.1063/1.2838983. [Online]. Available: https://doi.org/10.1063/1.2838983.

[215] G. K.-L. Chan, M. Kállay, and J. Gauss, "State-of-the-art density matrix renormalization group and coupled cluster theory studies of the nitrogen binding curve," *J. Chem. Phys.*, vol. 121, no. 13, pp. 6110–6116, Oct. 2004, ISSN: 0021-9606. DOI: 10.1063/1.1783212. [Online]. Available: https://doi.org/10.1063/1.1783212.

[216] W. Feller, *An Introduction to Probability Theory and Its Applications*. Wiley, 1968, vol. 1, ISBN: 0471257087.

[217] C. P. Robert and G. Casella, *Monte Carlo Statistical Methods*. Springer-Verlag, 2005, ISBN: 0387212396.

[218] H. Flyvbjerg and H. G. Petersen, "Error estimates on averages of correlated data," *J. Chem. Phys.*, vol. 91, no. 1, pp. 461–466, Jul. 1989, ISSN: 0021-9606. DOI: 10.1063/1.457480. [Online]. Available: https://doi.org/10.1063/1.457480.

Publication List

Publication List

- Sukurma, Z., Schlipf, M., Kresse, G., Self-Refinement of Auxiliary-Field Quantum Monte Carlo via Non-Orthogonal Configuration Interaction. *arXiv preprint* arXiv:2501.12765 (2025).
- Sukurma, Z., Schlipf, M., Humer, M., Taheridehkordi, A., Kresse, G., Toward Large-Scale AFQMC Calculations: Large Time Step Auxiliary-Field Quantum Monte Carlo. *J. Chem. Theory Comput.* **20**, 10, 4205–4217 (2024).
- Taheridehkordi, A., Schlipf, M., Sukurma, Z., Humer, M., Kresse, G., Phaseless auxiliary field quantum Monte Carlo with projector-augmented wave method for solids. *J. Chem. Phys.* **159**, 044109 (2023).
- Sukurma, Z., Schlipf, M., Humer, M., Taheridehkordi, A., Kresse, G., Benchmark Phaseless Auxiliary-Field Quantum Monte Carlo Method for Small Molecules. *J. Chem. Theory Comput.* **19**, 15, 4921–4934 (2023).
- Humer, M., Harding, M. E., Schlipf, M., Taheridehkordi, A., Sukurma, Z., Klopper, W., Kresse, G., Approaching the basis-set limit of the dRPA correlation energy with explicitly correlated and projector augmented-wave methods. *J. Chem. Phys.* **157**, 194113 (2022).
- Ramberger, B., Sukruma, Z., Schäffer, T., Kresse, G., RPA natural orbitals and their application to post-Hartree-Fock electronic structure methods. *J. Chem. Phys.* **151**, 214106 (2019).
- Dorner, F., Sukurma, Z., Dellago, C., Kresse, G., Melting Si: Beyond density functional theory. *Phys. Rev. Lett.* **121**, 195701 (2018).

Contributed Talks

- Sukurma, Z., Schlipf, M., Humer, M., Taheridehkordi, A., Kresse, G., Benchmark Auxiliary-Field Quantum Monte Carlo: Focus on Large Time-Step AFQMC. *DPG Spring Meeting of the Condensed Matter Section*, 2024 (Berlin, Germany).
- Sukurma, Z., Schlipf, M., Humer, M., Taheridehkordi, A., Kresse, G., Benchmark Auxiliary-Field Quantum Monte Carlo: Focus on Large Time-Step AFQMC. *TREX Symposium: Bridging Quantum Monte Carlo and High-Performance Simulations - Registration*, 2024 (Luxembourg, Luxembourg).

Posters

- Sukurma, Z., Schlipf, M., Humer, M., Taheridehkordi, A., Kresse, G., Accelerating Auxiliary-Field Quantum Monte Carlo. *17th Internationa Congress of Quantum Chemistry*, 2023 (Bratislava, Slovakia).
- Sukurma, Z., Schlipf, M., Humer, M., Taheridehkordi, A., Kresse, G., Accelerating Auxiliary-Field Quantum Monte Carlo. *Precision Many-Body Physics conference*, 2023 (Paris, France).
- Sukurma, Z., Schlipf, M., Humer, M., Taheridehkordi, A., Kresse, G., Auxiliary-Field Quantum Monte Carlo in the Projector Augmented Wave Method. *Psi-k conference*, 2022 (Lausanne, Switzerland).
- Sukurma, Z., Schlipf, M., Humer, M., Taheridehkordi, A., Kresse, G., Auxiliary-Field Quantum Monte Carlo in the Projector Augmented Wave Method. *CAMD Summer School on Electronic Structure Theory and Materials Design*, 2022 (Helsinngør, Denmark).